Characterization of chiral supramolecular assemblies using Mueller polarimetry

Shahana Nizar Nizar Shyla

Université de Strasbourg

UNIVERSITÉ DE STRASBOURG

École doctorale
Sciences chimiques | ED 222
Université de Strasbourg

ÉCOLE DOCTORALE DES SCIENCES CHIMIQUES

UMR 7006

THÈSE présentée par :

Shahana Nizar NIZAR SHYLA

soutenue le : **20 Septembre 2023**

pour obtenir le grade de : **Docteur de l'université de Strasbourg**

Discipline/ Spécialité : Sciences Chimiques

Characterization of chiral supramolecular assemblies using Mueller polarimetry

Caractérisation d'assemblages supramoléculaires chiraux par polarimétrie Mueller

THÈSE dirigée par :

M. GENET Cyriaque	Institut de Science et d'Ingénierie Supramoléculaires (ISIS), Université de Strasbourg, CNRS

RAPPORTEURS :

Mme CRASSOUS Jeanne	Institut des Sciences Chimiques de Rennes (ISCR), Université de Rennes, CNRS
Mme ZEHNACKER-RENTIEN Anne	Institut des Sciences Moléculaires d'Orsay (ISMO), Université Paris-Saclay, CNRS

AUTRES MEMBRES DU JURY :

M. EBBESEN Thomas	Institut de Science et d'Ingénierie Supramoléculaires (ISIS), Université de Strasbourg, CNRS

Acknowledgements

At the beginning of October 2020, I was a student with a master's degree in Chemistry with a bit of knowledge in molecular and supramolecular chirality, and highly ignorant about Mueller polarimetry. This journey as a Ph.D. student, helped me gather knowledge in optics, polarimetry, and chiroptical characterization, with the immense help and support of many individuals, whom I would like to acknowledge in this section.

First and foremost, I would like to thank Dr. Cyriaque Genet for accepting me as a Ph.D. student and giving me the opportunity to work in the field of Mueller polarimetry. I am thankful for his guidance and support throughout my journey, which has nourished my growth not only professionally but also personally in the academic world. As a supervisor, he has been extremely helpful and understanding, providing a friendly atmosphere in the lab and bringing a cozy working environment. Also, I am always amazed by his simple and elegant explanation of complicated scientific concepts which has been a great inspiration for me.

My sincere thanks to Prof. Thomas Ebbesen for hosting me in the institute through the ERC grant, and also for the amazing discussions not only regarding the work but also on growing in the academic world. The tips and stories that he shared will surely be helpful for my scientific growth.

I would like to express my sincere gratitude to Prof. Jeanne Crassous and Prof. Anne Zehnacker-Rentien for accepting to be on my thesis jury and for reviewing my thesis. I thank them for their critical analysis of the thesis and also for providing suggestions on various improvements. I have well enjoyed discussing my work with them during the defence which helped me look into different aspects of chiroptical studies.

I am immensely grateful to Prof. K. George Thomas for guiding me to the field of chirality through my Master's thesis in IISER-TVM, India. His immense support on theoretical studies on chirality during my Master's along with his suggestion on working in Mueller polarimetry has been the stepping stone to the success of this thesis.

I would also like to extend my gratitude to Prof. Anna Painelli, Dr. Cristina Sissa and Francesco Bertocchi for performing theoretical studies on the experimental results performed in this thesis.

Many thanks to Dr. Eloise Devaux for her support and suggestions for the experiments carried out in the lab. I am thankful for her patience in sitting through 4 rehearsals of my defence, which helped me improve my presentation skills. Sharing the technicalities of Mueller measurements has been made cheerful with her subtle sense of humour.

My sincere thanks to Marie-Claude Jouaiti for all the administrative support provided for my stay and research in Strasbourg. Her quick and efficient responses to my emails have made the tiring French administrative procedures much simpler.

Many thanks to Minghao Li, Sudipta Saha, and Jerome Gautier for helping me understand the basics of Mueller formalism, and the protocols and technicalities of the experiments. I am happy that I had an overlap of 1 year with Minghao Li, to carry out the experiments together. His profound knowledge and experience have helped me to progress faster with my experiments. I am incredibly thankful to Sudipta Saha for his patience in answering my never-ending questions on Mueller formalism, and also for his support even after he left the lab a year ago. Special thanks to Jerome Gautier, who taught me the baby steps to Mueller measurements in my 1st year, spending a lot of time teaching me on alignment of optical elements. Thanks also to Sujith Meleppatt for the wonderful discussions on chirality which has always fuelled me to explore more in this field of research. Many thanks to Anoop Thomas for the initial discussions on C8O3 aggregates that helped me move forward with my experiments in the lab.

Special thanks to Kripa M. Joseph, Anjali Jayachandran, and Shana Shirin Valapra for many academic and non-academic discussions, weekend fun, and Strasbourg explorations. The time we have spent cooking along with movie nights has made Strasbourg life more memorable. Looking forward to more ‘breaking legs together’ moments (not literally anymore) with Kripa.

I am extremely grateful to many other members of the lab – Luis Pires for being an amazing friend with whom I enjoyed having philosophical chit-chats, Bianca Patrahau for her incredible talents in finding the best restaurants, Antoine Tartar for being a nice office mate sharing fun facts on many things that made my stressful moments much lighter, Weijian Tao for inspiring discussions and Chinese delicacies, Kalaivannan Nagarajan for his help in the lab and also for the weekend get-together with delicious south-Indian food, Remi Goerlich for being a great office mate with occasional chats on work and life in Strasbourg.

I also thank Yoichi Sasaki, Soh Kushida, Kuidong Wang, and Sandeep Kulangara, for sharing their incredible knowledge on various scientific and non-scientific domains. In addition, the lab environment would not have been amazing without the presence of a few other members – Lucas Maisonnette and Arthur Luna. Further, I expect a lot more amazing interactions the lab could offer with the new members of the lab – Benjamin Boglio and Swathi Swaminathan, with their enthusiasm and vast knowledge on different aspects of science.

I am deeply indebted to my parents and sisters for their support and struggles to help me reach this achievement. This thesis would not have happened without their immense support for every decision I make and their deep interest to see me in great heights.

Special thanks to my friend – Mammu, for his constant motivation and support, encouraging me with his kind words to move forward whenever I felt tired and overwhelmed with failing experiments. Thanks to my best friends – Jibin, Anupama, and Arya for being amazing friends supporting through the difficulties of living away from home. I also thank my friend – Deepu, for his kind words and for sharing numerous funny life stories that made the writing time more cheerful.

Thanks to my 'worldwide buddies' – Sowmya, Awanti, Kirthana, and Maitreyee, though connected through the internet, have always been there to support me, available when needed to share the perks of Ph.D. and living abroad.

I am grateful for the presence of all these people in my life which has made my PhD life an enjoyable learning endeavour.

Merci à tous,

Shahana Nizar

Table of Contents

Bibliography

List of Publications

- Li, M.; Nizar, S.; Saha, S.; Thomas, A.; Azzini, S.; Ebbesen, T. W.; Genet, C. Strong Coupling of Chiral Frenkel Exciton for Intense, Bisignate Circularly Polarized Luminescence. *Angewandte Chemie International Edition* **2023**, *62* (6), e202212724.

- N.S. Shahana Nizar, Minghao Li, Sudipta Saha, Anoop Thomas, Thomas Ebbesen, Cyriaque Genet, 2D Excitation- emission Mueller polarimetry, (Manuscript under preparation)

Conference Presentations

- Journée des doctorants, Strasbourg, November 30, 2021 (Oral).
  Shahana Nizar.

- Polysolvat-14 Conference (international conference on polymer-solvent complexes and intercalates), Strasbourg, September 19-22, 2022 (Poster).
  Shahana Nizar, Minghao Li, Sudipta Saha, Anoop Thomas, Stephano Azzini, Thomas Ebbesen, Cyriaque Genet.

- JACC (Journées André Collet de la Chiralité) Conference, Biarritz, October 4-7, 2022 (Oral).
  Shahana Nizar, Minghao Li, Sudipta Saha, Anoop Thomas, Stephano Azzini, Thomas Ebbesen, Cyriaque Genet.

- ISIS young scientist seminar, Strasbourg, April 13, 2023 (Oral).
  Shahana Nizar

Chapter 1

Fundamentals of chirality: origin and diversity

In this Chapter, we present the basic concepts and sources of the current research interests related to molecular and supramolecular chirality. The ubiquitous properties of asymmetry have attracted the attention of researchers from a wide range of fields combining synthetic knowledge, theoretical expertise, and analytical spectroscopy methods for understanding the fundamental origin of chirality and exploiting it for functional applications. In this Chapter, we briefly discuss the evolution of the field of chirality that paved the way for classifying chiral signatures based on their specific symmetries and structural forms, such as point chirality, axial chirality, and supramolecular chirality. We also discuss the theoretical understanding of the emergence of monosignate and bisignate circular dichroism, and circularly polarized luminescence in molecules and supramolecular assemblies. Furthermore, we present different analytical techniques that have recently been developed for characterizing chiral structures aimed at improving the sensitivity of artifact-free chiroptical signal detection.

1.1 Introduction on chirality

Chirality, with a Greek etymology meaning hand for *cheir*, defines structures with non-superimposable mirror images.[1] It is a fundamental and unique property of matter observed primarily in nature as spiral galaxies, seashells, and biomolecules, intriguing researchers trying to answer the ever-puzzling questions of homochirality (Figure 1.1).[2–4] Looking deeper into lower scales, beginning with the spin of subatomic particles to naturally occurring homochiral biomolecules of nucleic acids, amino acids, and sugars, and nano- and microscale supramolecular structures, the property has been fascinating for many in the field of physics, chemistry, and biology.[5–9] Ranging from exploring the fundamental insights on how nature evolved into uniqueness, to benefitting from the property for technological advancements in the field of organic light emitting diodes (OLEDs), anti-counterfeiting, 3D display, chiral photonics, and chiral separation for pharmaceutical applications, the field of chirality is to-date a research topic of extreme interest.[10–20]

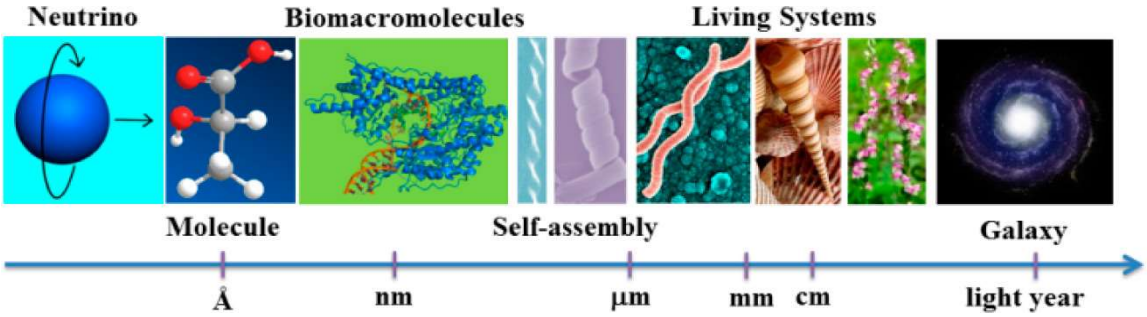

Figure 1.1: *Chirality at different scales from subatomic particles such as neutrinos, to molecules, biomolecules, self-assembled structures, living systems and spiral galaxies. Adapted with permission from ref* [21].

The two non-superimposable mirror symmetric structures identified as chiral systems are called enantiomorphs, while those of molecular species are called enantiomers. These enantiomers of chiral molecules possess similar physical and chemical properties such as melting point, boiling point, density, etc. However, the two species differ only in the way they interact with the environment around them, depending on their intrinsic chiral signature. Many branches of science have evolved with a focus on investigating different aspects of chiral interactions. These include studying chiral forces, chiral chemical reactions, and chiral light-matter interaction.[22–24]

1.2 Light-matter interactions: polarization and chirality

Light-matter interaction is a complex yet intriguing field of study focusing on the exchange of energy between matter and light, that has a quantum-mechanical description along with satisfying the classical laws of conservation of energy and momentum.[25] Light has served as a vital tool for studying the physical and chemical properties of matter, developing into the field of optics and polarimetry. Absorption and emission are two important phenomena probed by exciting a molecular system with light, that gives the ground and excited state properties of a system, respectively, such as the energy level distribution and the energy-transfer processes.[26] However, light described in classical physics not only provides the energetic distribution of matter but also the geometrical and structural aspects once engaging its polarization responses. Chiral properties, which are a geometrical feature can thus be probed with the aid of polarized light. This method of characterizing materials with the merging of concepts taken from polarimetry and chirality began in the early 19th century.[27]

Beginning with E. L. Malus, who brought out the concept of light polarization, followed by L. Arago introducing the rotatory power, the field of polarimetry inspired many to expand the understanding of light-matter interaction.[28,29] Later, the works of Fresnel and Biot pushed the concepts forward dwelling on optical activity, defined as the ability of a substance to rotate the plane of polarization of light passing through it.[30,31] The research followed by Haidinger in 1846 and Cotton in 1895 introduced the concept of circular dichroism (CD), which is defined as the differential absorption of left and right circularly polarized light. This concept has still been used as an important method to characterize chiral nature of molecules and materials (Figure 1.2.a).[32]

As CD emerged as an efficient method to study ground state chirality, researchers were more intrigued to explore the excited state chirality, with studies beginning in the early 20th century. The excited state chirality can be revealed by exciting a sample with unpolarized or linearly polarized light and measuring the difference of left- and right- circularly polarized luminescence (CPL) (Figure 1.2.b). The first experiments of CPL were performed on chiral crystals of sodium uranyl acetate.[33] Research on CD and CPL was not only focused on exploring molecular properties but also a significant surge of research was aimed at developing better instrumentations as well as the theoretical framework for characterizing and analysing associated chiral signatures.[34] This is to date a growing research field as we will discuss later in this Chapter.

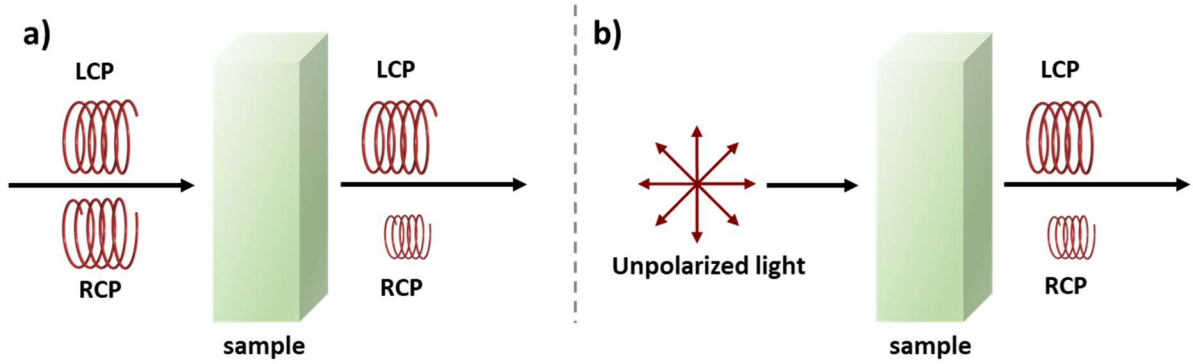

Figure 1.2: *Schematics showing measurements of circular dichroism (CD) (a) and circularly polarized luminescence (CPL) (b) in conventional CD and CPL spectrometers. In the CD spectrometer, we measure the difference in the absorbance of left circularly polarized light (LCP) and right circularly polarized light (RCP) by a sample. In CPL spectrometer, we measure the difference in the emission intensity of LCP and RCP, when the sample is excited with unpolarized light.*

1.3 Chirality at different scales

Chirality can be observed at different scales from small organic molecules to nano and microstructures. Within organic molecules, we observe point chirality, planar chirality and axial chirality (Figure 1.3).[35–38] Helicenes are another class of molecules that show helical chirality, where the isomers are termed P-helicenes (right-handed) and M-helicenes (left-handed).[39–41] Apart from organic molecules, inorganic structures such as lanthanide complexes are another category of molecules widely studied, that shows the largest CPL signals ever reported.[42–45] Moving on larger scales, chiral inorganic and metal nanoparticles were prepared through chiral induction with the use of chiral ligands or chiral solvents.[46–48]

The research interest in the field of chirality currently explores molecular systems that display signatures of exciton coupling where the chiral signals are enhanced to ranges that simple organic molecules cannot reach.[49] This feature of chiral amplification is predominantly observed in supramolecular assemblies, where monomers stack in a helical fashion depending on various structural and environmental conditions of the system. Similar structures have a great tendency to force the transition dipole moment (exciton) of monomers into the strong coupling regime giving rise to strong CD and CPL signals.[49] These supramolecular assemblies are of particular interest in this thesis. Therefore, we will discuss further about these structures in this Chapter.

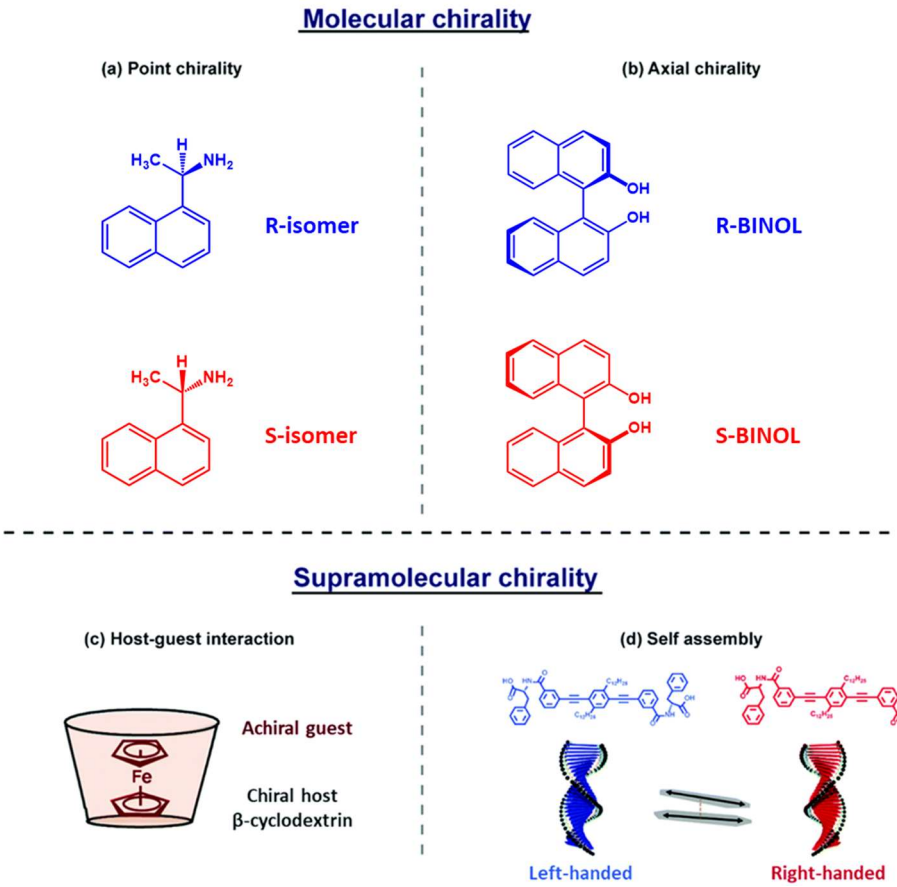

***Figure 1.3**: Elucidation of chirality in different dimensions where point chirality is shown in R- and S- isomers of 1-(1-naphthyl)-ethylamine (a). Axial chirality is demonstrated by R- and S- isomers of 1-1'-Bi-2-naphthol (BINOL) (b), and supramolecular chirality is observed from host-guest complexes of cyclodextrin (c), and helical assemblies of phenyleneethynylene-based molecular systems (d). Adapted with permission from ref* [49].

1.4 Supramolecular assemblies and symmetry breaking

The field of supramolecular assemblies has grown from a simple science of host-guest complexation (Figure 1.3.c) to a field currently explored in every part of the world, with a high interest in understanding living systems that constitute complex forms of sophisticated supramolecular species such as proteins, DNA, cellular structures, all functioning in harmony.[50–53] Not only to understand the working mechanisms of complex supramolecular architectures in a living form by mimicking them using bioinspired materials, but the field has also emerged into developing functional materials to challenge the world problems of pollution, to propose new technological applications and to develop medical diagnostics.[54–57]

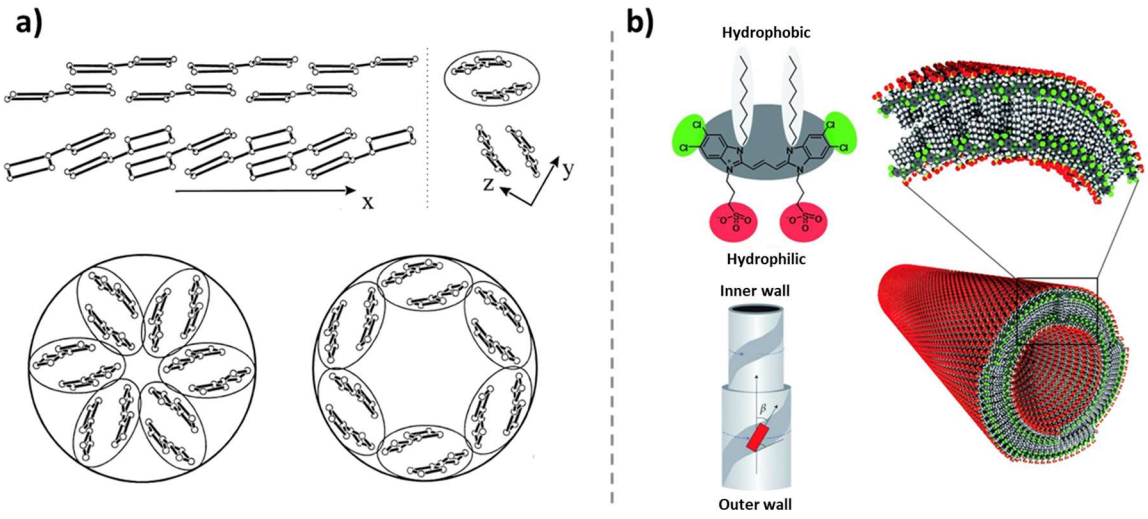

Figure 1.4: *Schematics of supramolecular self-assembly of pseudoisocyanine (PIC) (a), and C8S3 aggregates (b), with the representation of their molecular packing. The hydrophobic and hydrophilic groups of C8S3 that drives the formation of double walled (inner and outer wall) tubular aggregates is also indicated. The angular orientation of molecules (β) with respect to the longitudinal direction of the tube is also marked. Adapted with permission from ref* [58].

Supramolecular assemblies, supramolecular polymers, and self-assemblies are interconnected terminologies in the field of supramolecular chemistry. However, self-assembly is intriguing with its specificity of assemblies formed by the stacking of molecules triggered through little human intervention such as subtle changes in their environment (Figure 1.3.d).[59] The aggregation of pseudoisocyanine (PIC) discovered independently by Scheibe and Jelley, belongs to some of the initial examples of systems undergoing self-assembly, which prompted much attention towards similar cyanine-based aggregates (Figure 1.4).[60–63] These assembly formations and their spectroscopic output are extremely sensitive to the environment. The subtle changes in polarity, temperature, presence of impurities, and water content in organic solvents can significantly influence the energetics in the nucleus of aggregation, amplifying the process to various aggregated species.[64–67] These drastic variations occur mainly by triggering the possibilities of diverse organizations, initiated through weak intermolecular non-covalent interactions.

As a consequence, reproducing these delicate aggregation stages can be extremely difficult, demanding careful experimental strategies. While these delicate structures are difficult to handle with precise environmental monitoring, it is worth exploring their energetic variation looking for kinetic and thermodynamic species, which sometimes coexist. Many experimental

works were carried out to bias the structures by populating one aggregation stage over the other for scientific advantages (Figure 1.5).[68–70] These experimental strategies usually involve two or more solvent compositions, where one dissolves well the monomers (good solvent) while the other destabilizes their monomeric existence (bad solvent). Therefore, with a specific ratio of different solvents, we can drive the monomers to reach an energetic minimum, arriving at a stable supramolecular assembly. These aggregation pathways can then be modified through precise temperature-dependent monitoring protocols. Exploring such pathway complexities began with the seminal work of Meijer and co-workers which has turned now into an advanced field of supramolecular chemistry.[68]

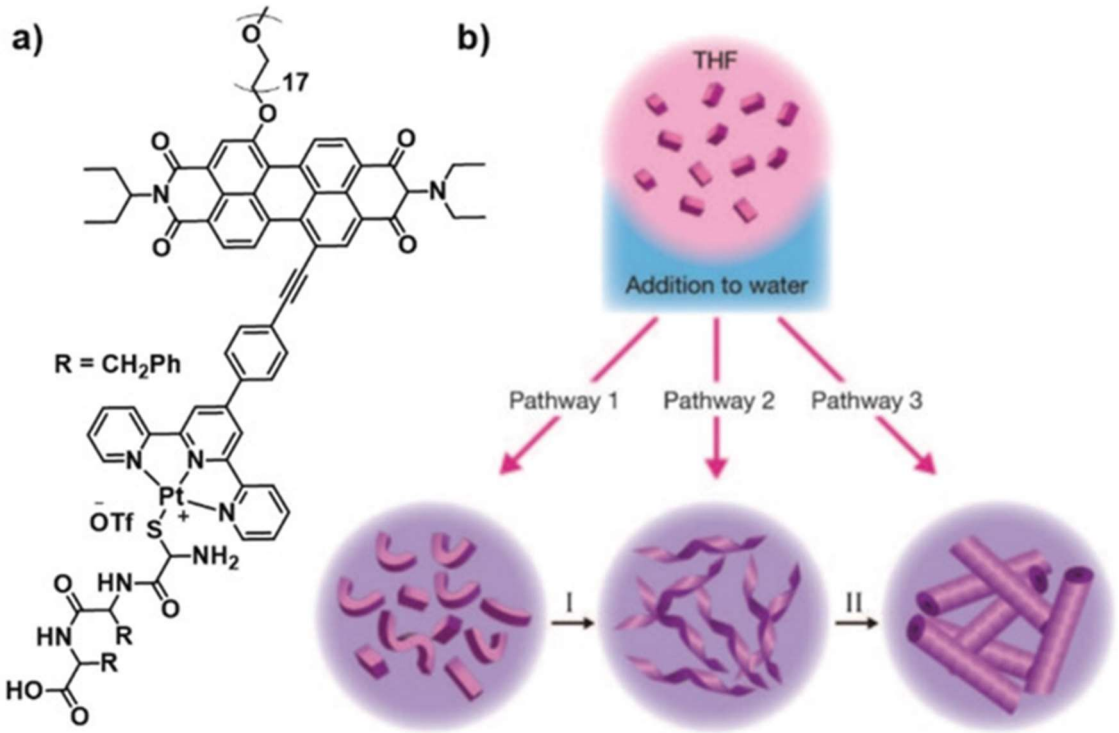

Figure 1.5: *(a) Chemical structure of amphiphilic perylene diimide (PEG-PDI)/terpyridine (terpy) platinum complex. (b) Schematics of pathway depended self-assembly of these molecules. Here, pathway 1 is obtained at 95:5 (v/v) water/THF; pathway 2 at 80:20 (v/v) water/THF, keeping for 45 min at room temperature, followed by dilution with water to attain a 95:5 (v/v) water/THF ratio; pathway 3 at 80:20 water:THF, keeping for 40 h at room temperature, followed by dilution with water to attain a 95:5 (v/v) water/THF ratio. Pathway I obtained with the addition of THF to a water/THF=95:5 (v/v) mixture yielding a water:THF=80:20 (v/v) ratio, and evolution at room temperature for 70 h; pathway II is*

obtained through further evolution for 4 days, or addition of THF to attain a 70:30 (v/v) water/THF ratio followed by evolution for 70 h. Adapted with permission from ref [71].

The extreme sensitivity of structural organization in a self-assembled system with respect to its environment, comes as an advantage when one focuses on chirality. Traditionally, chiral aggregates are prepared by either attaching a chiral handle to an achiral chromophore or by immersing achiral molecules in a chiral environment, thereby forcing aggregation [72–74] However, there exist yet other molecular species, that are achiral in their monomeric form but undergo spontaneous symmetry breaking to form chiral aggregates.[75–77] These structures have been investigated by many over recent years. They provide good archetypal systems for understanding the origin of chirality and possibly shine light on the puzzling questions on homochirality.

C8O3 (3,3′-bis(3-carboxy-n-propyl)-3,3′-di-n-octyl-5,5′,6,6′-tetrachlorobenzimidacarbocyanine) is one such fascinating molecule from the cyanine family that forms chiral tubular aggregates. Aggregation of this cyanine dye resides at the core interest of the studies gathered in this thesis. C8O3 aggregates into both left and right chiral tubes, however, showing occasional predominance of one chirality.[76,78] Developing specific methodologies to characterize such complex chiral systems can bring out new features which may not be easily observed in the bulk state. This fascinating and crucial aspect will be explored in this thesis.

1.5 Theoretical framework on molecular and supramolecular chirality

Along with experimental advancements in developing new supramolecular assemblies and characterizing them, appropriate theoretical frameworks were developed to understand the intriguing spectral features of molecular and supramolecular systems. We now discuss some theoretical advancements in the field of molecular and supramolecular chirality that will guide through the analysis performed in the following Chapters of this thesis. These theoretical discussions have mostly been drawn from my previously published review titled "Emergent chiroptical properties in supramolecular and plasmonic assemblies", co-authored by Meleppatt Sujith, K. Swathi, Cristina Sissa, Anna Painelli and K. George Thomas, during my Master's degree at IISER Thiruvananthapuram.[45]

1.5.1 Origin of circular dichroism

When electromagnetic radiation interacts with matter, resonant energy exchanges happen when the frequency of the light field is close to the transition frequency of matter, creating oscillations of electrons that corresponds to the generation of a transition dipole. At this resonance condition, the transition energy, ω_{eg}, equivalent to the frequency of excitation, ω, is defined as

$$\omega = \omega_{eg} = (E_e - E_g)/\hbar \tag{1.1}$$

where E_e is the energy of excited state and E_g is the energy of ground state.[79] These transitions measured as an absorption spectrum correspond to the oscillator strength evaluated from the area under the absorption band. The oscillator strength can thus be written as,

$$f_{eg} = \frac{2m}{3\hbar e^2}\omega_{eg}\langle g|\hat{\mu}|e\rangle \cdot \langle e|\hat{\mu}|g\rangle \tag{1. 2}$$

where $\hat{\mu}$ is the electric transition dipole moment operator. This expression shows that the intensity of a transition in the absorption spectrum is proportional to the square of the transition dipole moment.

In addition, the magnetic component of the light can interact with the electrons to generate a magnetic dipole. Accordingly, if the electric and magnetic dipoles generated in the matter are aligned, we obtain a rotation of the electric field generating a CD response. This intrinsic chiroptical property generated through electric and magnetic dipole coupling is understood through the Rosenfeld equation defining rotational strength (R_{eg}) as,

$$R_{eg} = Im(\langle g|\hat{\mu}|e\rangle \cdot \langle e|\hat{m}|g\rangle) \tag{1.3}$$

where $\hat{m}$ is magnetic dipole moment operator.[32,80,81] Therefore, a nonvanishing high rotational strength is a determining factor for a high CD signal, which is particularly observed from non-centrosymmetric molecular systems, also called chiral molecules (Figure 1.3.a,b). These intrinsic chiral signatures from molecules emerge as a monosignate peak near the absorption wavelength-range of the material. Similarly, axial chirality also originates due to the coupling of electric and magnetic dipoles, as extensively studied in a variety of hexahelicenes (Figure 1.6). Though the chiral response of simple asymmetric organic molecules can be understood with the above-discussed theoretical description, the origin of induced CD (ICD) and exciton-coupled CD (ECD) demands extended theoretical understandings.

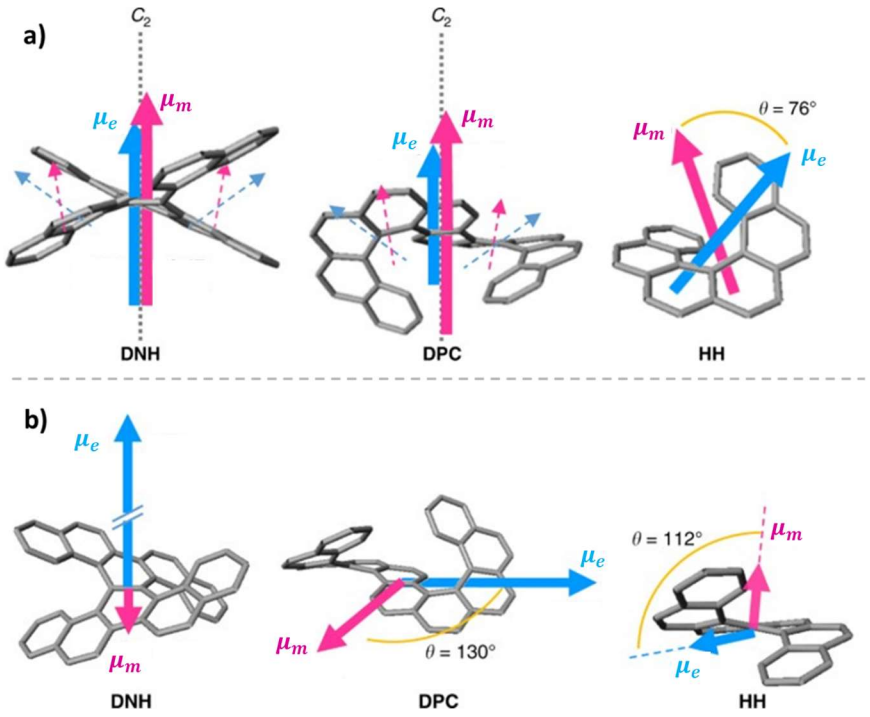

Figure 1.6: *Electric ($\vec{\mu}_e$) and magnetic ($\vec{\mu}_m$) dipole arrangement in the ground (a) and excited (b) states of different helicene based structures such as dinaphtho[2,1-i:1',2'-l]hexahelicene (DNH), diphenanthro[3,4-c:3',4'-l]chrysene (DPC), and hexahelicene (HH). The dashed arrows represent the dipoles in single HHs and the solid arrows represent dipoles in the whole molecule. Adapted with permission from ref* [82].

1.5.2 Induced chirality

In a mixture of chiral and achiral molecules, transfer of chirality can occur from a chiral host to an achiral guest molecule giving rise to a chiral signal in the spectral profile of the otherwise achiral molecule.[83–85] This ICD signal originates from either the reduction of symmetry of achiral molecules in chiral environment called the "structurally induced chirality", or from the non-degenerate coupling of electric transition dipoles of chiral and achiral species without any structural modifications (Figure 1.7).[86–88]

For the former case of ICD through structurally induced chirality, we observe a monosignate CD signal near the absorption wavelength regime determined through nonzero rotational strength (Eqn.(1.3)). In the latter case, in contrast, a bisignate profile (bimodal with opposite chirality) emerges, but with one peak relatively more intense than the other due to the non-degeneracy of the coupled transition dipoles. The absorption and the CD signals, therefore, appear nearer to the guest chromophore. The rotational strength for such a system can be expressed using the Kirkwood coupled oscillator theory as,

$$R \propto \frac{\omega_a \omega_b \mu_a^2 \mu_b^2}{\omega_b^2 - \omega_a^2} \times [\hat{e}_a \cdot \hat{e}_b - 3\frac{(\hat{e}_a \cdot \vec{r}_{ab})(\hat{e}_b \cdot \vec{r}_{ab})}{r_{ab}^2}] \frac{\hat{e}_a \times \hat{e}_b \cdot \vec{r}_{ab}}{r_{ab}^3} \quad (1.4)$$

where ω_a and ω_b are transition frequencies of molecules *a* and *b,* respectively. μ_a and μ_b are respective electric transition dipoles, $\hat{e}_a$ and $\hat{e}_b$ are unit vectors in the direction of transition dipoles, r_{ab} is the distance between the two dipoles. The above expression indicates that the rotational strength can also be induced from the relative arrangement of electric dipoles of host and guest molecules (magnetic dipoles not involved, in contrast with Eqn.(1.3)). This rotational strength is inversely dependent on the transition frequencies of the host and the guest molecules.[86,89] Therefore, a small energy gap between the interacting states of host and guest is important for obtaining a large ICD.

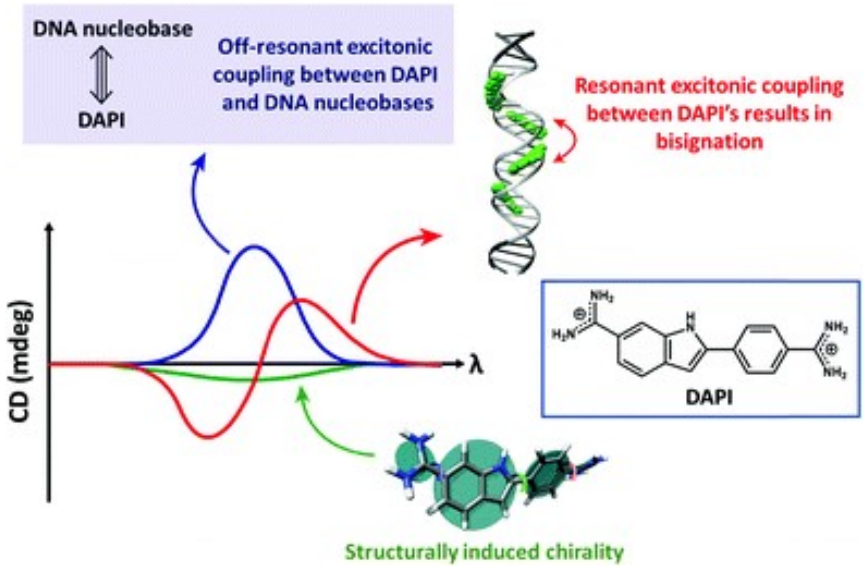

Figure 1.7: *CD spectra of 4',6-diamidino-2-phenylindole (DAPI) observed through structurally induced chirality (green), off-resonant exciton coupling between DAPI and DNA nucleotide (blue), and resonant exciton coupling between DAPI molecules on the surface of DNA nucleotide (red). The helical distribution of DAPI on the surface of DNA nucleotide is also presented. Adapted with permission from ref* [90].

1.5.3 Exciton coupled chirality

At the beginning of the 1900s, Kuhn proposed the coupled oscillator theory, which was later developed by Davydov to explain excitonic effects in molecular crystals.[91–94] Later, Kasha and McRae invoked the concept to explain the spectral variations observed in molecular aggregates that show the feature of bisignation in the CD signal (red signal in Figure 1.7).[95,96] These developments have been significant in the context of chirality. It is only in 1969,

however, that a general rule for assigning the handedness based on the sign of CD signal was put forth by N. Berova, N. Harada and K. Nakanishi initially to study a variety of natural products and synthetic chiral molecules.[97,98] Later, the application of this rule was extended to biological systems and molecular aggregates to understand their optical response.[37]

We will explain in this Section more precisely about these studies on correlating the sign of CD signal to the handedness of chiral structures focusing on molecular aggregates. These aggregate structures mainly involve H-aggregates with side-by-side transition dipole arrangement and J-aggregates with head-to-tail arrangement of monomeric units (Figure 1.8). In these structures, an H-aggregate displays blue-shifted absorption, while a J-aggregate shows a red shift.[99] Along with these features, H-aggregates display a huge suppression of emission while J-aggregates show enhancement of emission, as observed in many cyanine J-aggregates.[100,101] Note that, 'null' aggregates are also observed where molecules are perpendicularly oriented with respect to each other, giving rise to less significant spectral variations during absorption and emission.[102]

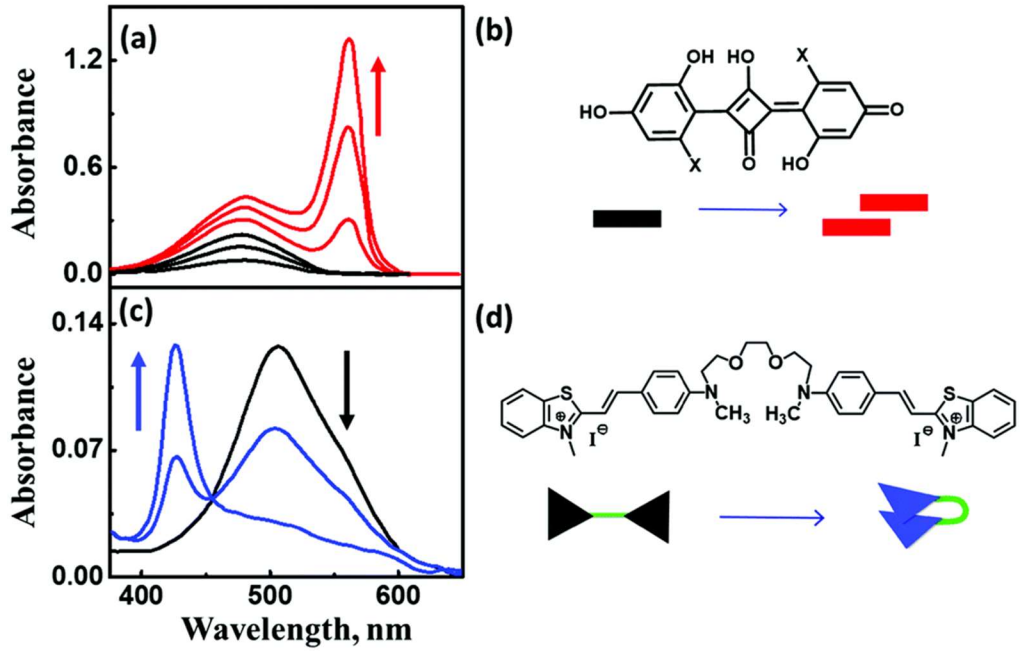

Figure 1.8: *Absorption spectra (a) monitoring the concentration dependent formation of J-aggregates of Squarine dye (b) by varying the concentration between 1.2–13.3 μM. Solvent dependent folding of bichromophoric cyanine dye (d) to form H-aggregate in a mixture of*

toluene and dichloromethane monitored through its corresponding absorption spectra (c). Adapted with permission from ref [49, 100].

With the simple exciton model, these spectral properties can easily be explained. According to the model, when two molecules come in close proximity, their electric transition dipoles undergoes dipole-dipole coupling resulting in two new states leading to delocalization of the electronic transitions, which is the formation of exciton. This model is limited to a single excited state for molecules and the interaction between degenerate electronic states. The newly formed states are linear combinations of single excitonic states with either in-phase or out-of-phase dipolar coupling and are separated with an energy gap twice the interaction energy between the transition dipoles. This resultant splitting is called the Davydov splitting.[92]

To model these dipole interactions, we can consider two equivalent interacting molecules, each with a ground state, $|g\rangle$ and excited state, $|e\rangle$. Hence, the electronic states of the dimer can be expressed as $|g_A g_B\rangle$, $|g_A e_B\rangle$, $|e_A g_B\rangle$ and $|e_A e_B\rangle$ with energies 0, E, E, and 2E, respectively. With the point dipole approximation, we can write the interaction energy (V) between the transition dipoles $\vec{\mu}_A$ and $\vec{\mu}_B$ as,

$$V = \frac{\vec{\mu}_A \cdot \vec{\mu}_B}{4\pi\varepsilon_0 r^3} - \frac{3(\vec{\mu}_A \cdot \vec{r})(\vec{\mu}_B \cdot \vec{r})}{4\pi\varepsilon_0 r^5} \quad (1.5)$$

$$= \frac{\mu_A \mu_B}{4\pi\varepsilon_0 r^3}(cos\,\alpha - 3\,cos\,\theta_A\,cos\,\theta_B) \quad (1.6)$$

where α, θ_A and θ_B are angles, and r is the distance between the two transition dipoles, as defined in the Figure 1.9.

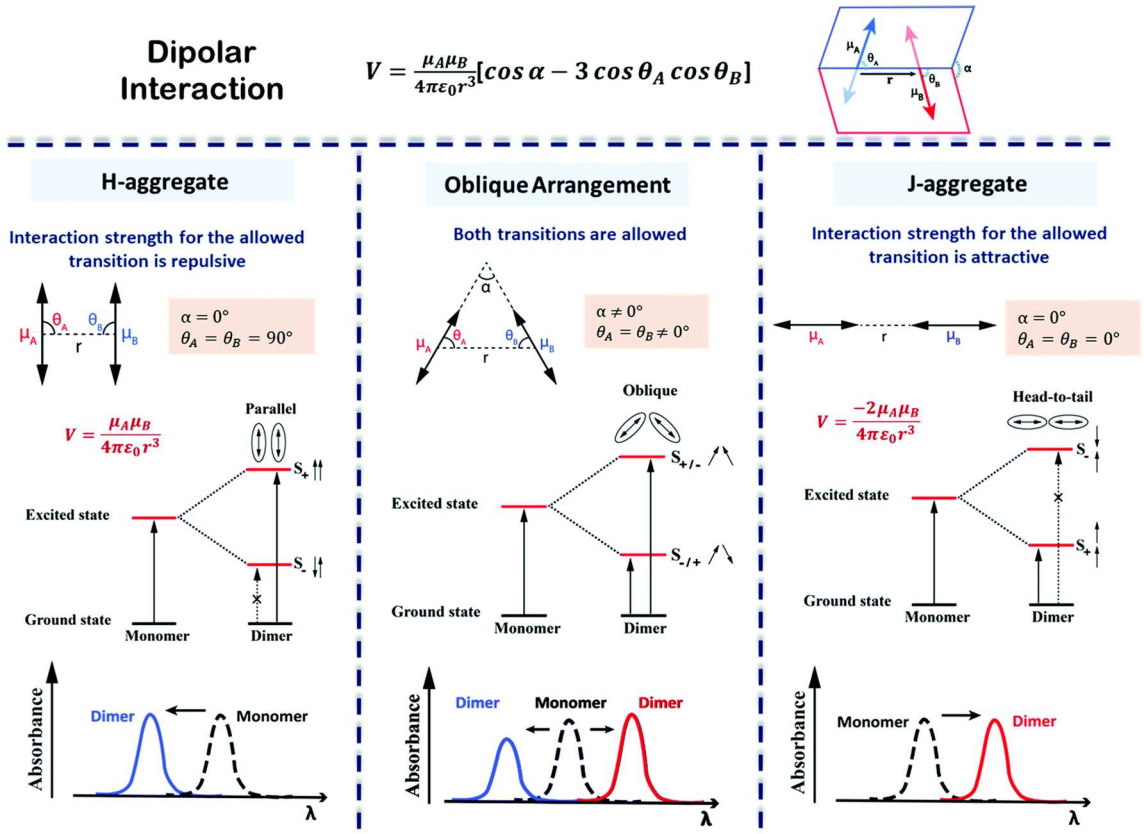

Figure 1.9: *Schematics illustrating various dipole arrangements for the formation of H-aggregate (left panel), J-aggregate (right panel) and oblique dipole coupling (middle panel). Their corresponding allowed and forbidden electronic transitions are also shown in solid and broken arrows, respectively. A transition is allowed only if the vectorial sum of the dipoles is non-zero. The dipolar interaction strengths (V) for H- and J-aggregate are calculated, that gives a positive quantity for the H aggregate (repulsive), while a negative value for the J-aggregate (attractive). This gives a blue-shift in the absorption spectrum for the H-aggregate (left panel), while a red shift for the J-aggregate (right panel). The oblique dipole arrangement can have either a positive or negative interaction strength depending on the geometry, and therefore transitions are allowed to both the electronic excited states (middle panel). The oblique arrangement can show absorbance on both sides of the monomeric absorption band with relative absorption strength depending on the geometry. Adapted with permission from ref* [49].

Within the Heitler-London approximation, we can neglect the interaction between non-degenerate states. This gives the two new states $|S_+\rangle$ and $|S_-\rangle$ expressed as,

$$|S_\pm\rangle = \frac{1}{\sqrt{2}}(|e_A g_B\rangle \pm |g_A e_B\rangle), \qquad (1.7)$$

with energies,

$$E_{\pm} = E \pm V. \tag{1.8}$$

Therefore, the two newly formed states are separated by an energy difference corresponding to twice the interaction strength between the two transition dipoles. These transition dipoles of the newly formed states are also linear combinations of individual dipoles written as,

$$\vec{\mu}_{\pm} = \frac{\vec{\mu}_A \pm \vec{\mu}_B}{\sqrt{2}}. \tag{1. 9}$$

Therefore, for linear aggregates, the transition is allowed only from S_0 to the S_+ state, whereas it is forbidden for the transition from S_0 to the S_- state. Due to this transition selectivity, we observe a blue-shifted absorption spectrum for an H-aggregate with intensity proportional to $2\mu^2$. In contrast, for J-aggregate, we observe a red-shifted absorption spectrum with an intensity proportional to $2\mu^2$. The spectral variations depending on the geometry of the dipole arrangement are presented in Figure 1.9.

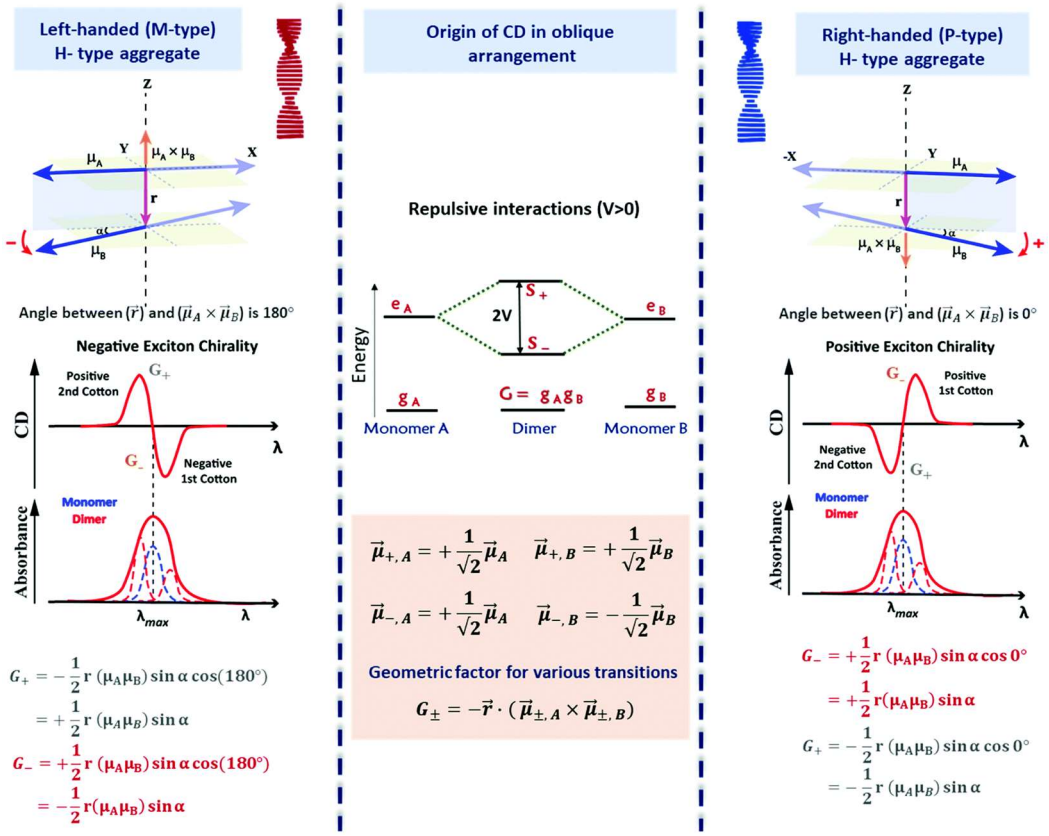

Figure 1.10: *Schematic illustrating right- and left-handed dipole arrangement in a helical aggregate and the origin of their respective bisignate CD signal. In this geometry, V > 0 and*

S_+ is at a higher energy than S_-. The transition happens from the ground to both the electronic excited states, giving rise to absorption in both sides of the monomeric absorption (with different intensities). This two transitions give rise to the bisignate profile for the H-aggregate. The intensity of the CD signals related to the $S_\pm$ states is given by $R_\pm$ in Eqn. (1.10) leading to equal and opposite signals for the two states. The direction of the vector product $\vec{\mu}_{\pm,A} \times \vec{\mu}_{\pm,B}$, is obtained using the right-hand rule, explaining the opposite sign for the right-handed and left-handed helices. Adapted with permission from ref[49].

While these linear aggregates are intriguing by themselves, with such selective transitions, the oblique arrangement of dipoles is even more remarkable in regards to its ability to display chiroptical features, especially with the appearance of bisignation in the CD signal. To understand this origin of bisignate CD signal for oblique dipole arrangement, we have to invoke the Rosenfeld equation (Eqn.(1.3)) and account for the dipole-dipole interaction between the molecules based on the exciton model, along with considering the coupling of electric and magnetic dipoles.[37]

With this exciton model, we arrive at the simplified expression for the rotational strength as,

$$R_\pm = \frac{G_\pm E_\pm}{2} \tag{1.10}$$

where

$$G_\pm = -\vec{r} \cdot (\vec{\mu}_{\pm,A} \times \vec{\mu}_{\pm,B}), \tag{1.11}$$

is called geometric factor. This expression quantifies the relative orientation of dipoles, which is the main parameter describing the CD signal in a supramolecular aggregate. Here, $R_\pm$ and $G_\pm$ corresponding to the rotational strength and geometric factor for the respective $S_\pm$ states. $\vec{\mu}_{\pm,A/B}$ is the contribution of the A/B molecules to the transition dipole moment for excitation to the $S_\pm$ states, and $\vec{r}$ is distance vector connecting the transition dipoles of A and B.

The oblique arrangement of dipoles can give rise to two kinds of aggregates, which are of H-type called the helical aggregate, and of J-type called the creeper-helical aggregate.[49,103] The mathematical representation of the geometric factor for each of the newly formed states and their spectral features characterizing bisignation are presented in Figures 1.10 and 1.11. The dependence of the sign of the CD signal with the dipole arrangement (H-type or J-type) and the handedness of dipole orientation can be understood by comparing these Figures. This

theoretical understanding based on the exciton model shows that the chiroptical signals of helical and creeper-helical geometries differ not only for different handedness but also depend on the type of interaction between the dipoles. The reversal in the CD couplet observed for opposite handedness occurs due to the difference in angle between the separation distance vector, $\vec{r}$, and the resultant dipole moment ($\vec{\mu}_{\pm,A} \times \vec{\mu}_{\pm,B}$). On the other hand, the reversal in CD couplet for the same handedness of helical and creeper-helical geometries occurs due to the reversal in the $S_{\pm}$ states for different geometries (comparison made between Figures 1.10 and 1.11).

This correlation between the sign of CD signal and the handedness is laid down as a general rule for exciton coupled systems, called the exciton chirality rule.[37] To understand the origin of the CPL signal, we have to combine the exciton model with Kasha's rule, which says that a transition associated with appreciable quantum yield occurs from the lowest excited state.[104] Therefore, the exciton model predicts a monosignate CPL signal for both helical and creeper-helical aggregates originating due to the transition from the lowest excited state to the ground state. Hence, the sign of the CPL signal depends on the sign of rotational strength or CD signal for the first Cotton effect at the highest wavelength. The Cotton effect is the characteristic change in the sign of the CD signal in the vicinity of the absorption maximum (see CD spectra in Figures 1.10 and 1.11).

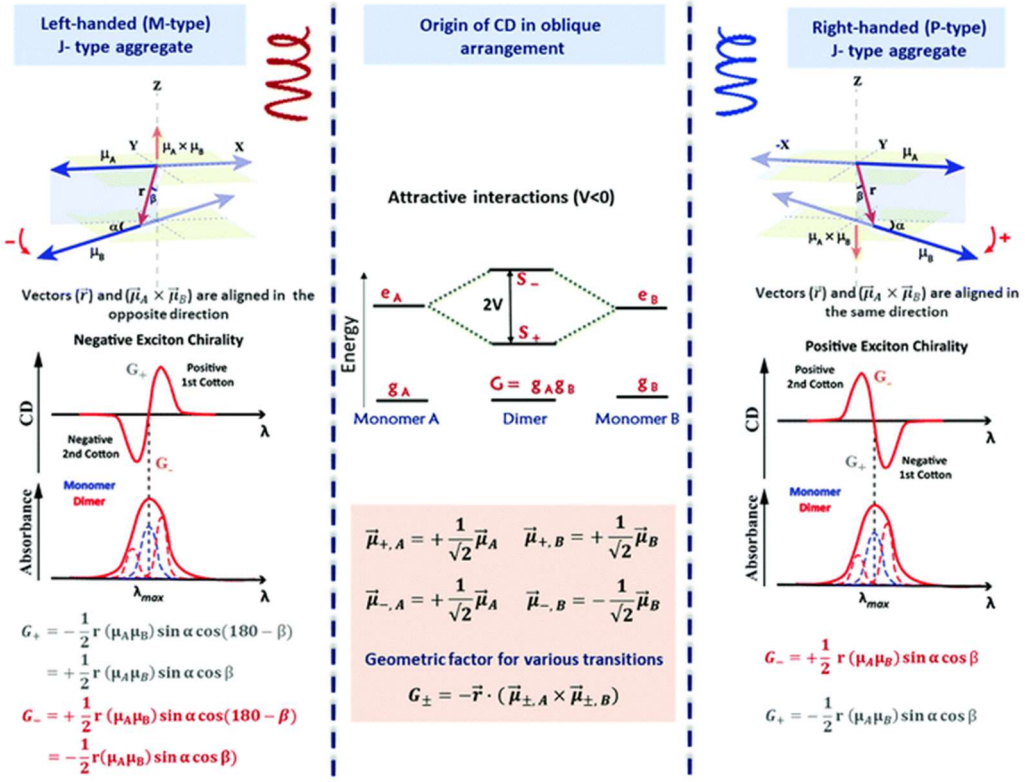

Figure 1.11: *Schematics illustrating right- and left-handed dipole arrangements in helical aggregates and the origin of their respective CD signals. In this geometry, $V < 0$ and S_- is at higher energy than S_+. The transition happens from ground to both the electronic excited states, giving rise to absorption on both sides of the monomeric absorption (with different intensities). This two transitions give rise to the bisignate profile for the J-type aggregate. The intensity of the CD signals related to the $S_\pm$ states is given by $R_\pm$ in Eqn.(1.10) leading to equal and opposite signals for the two states. The direction of the vector product $\vec{\mu}_{\pm,A} \times \vec{\mu}_{\pm,B}$, is obtained using the right-hand rule, explaining the opposite sign for the right-handed and left-handed helices. Here, the sign of bisignate CD signal is opposite for both handedness in comparison to Figure 1.10 describing the case of H-type aggregates. Adapted with permission from ref* [49].

The model detailed above considering the case of a dimer has limitations when dealing with larger aggregates constituting multiple monomers under exciton strong coupling. In such a situation, one must go beyond the simple exciton model to incorporate factors associated with other properties such as exciton delocalization length and energetic disorder in the monomeric packing.[72,105] Spano and co-workers have studied in depth the influence of these parameters in defining the spectral features of molecular aggregates.[106,107] Especially, the energetic disorder that arises due to conformational changes in molecules within the assembly, thermally induced deformation or solvent environment can modify the delocalization process.[108–110] These

influences of energetic disorder and delocalization of exciton can also influence the chiroptical properties of molecular assemblies. Spano and co-workers have further theoretically shown the dependence of exciton delocalization length (exciton coherence length) in determining the CD and CPL of molecular aggregates.[111] Moreover, the spectral shift and the intensity of these signals are also extremely dependent on this delocalization or coherence length.

This influence of the coherence length and the relative dipolar angles in determining the spectral shift and intensity were also explored in detail in the literature.[103,110,112] In a J-type helical aggregate, an increase in exciton coherence length can increase the emission intensity whereas it will be decreased in H-aggregate as the transition from the lowest eigenstate is forbidden. Along similar lines, the chiral output also varies as the coherence length strongly influences the CD and CPL of a supramolecular system.[113–115] Therefore, modulating the exciton coherence length in supramolecular structures can be an excellent way to generate intense circularly polarized luminescence for functional applications.

1.6 Probing chirality: ground and excited states

Traditionally, ground state chirality is measured in a CD spectrometer by exciting the sample with linearly polarized light and measuring the ellipticity of the transmitted light. The chiral polarization efficiency of the system can be determined by estimating the ground state dissymmetry factor, g_{abs}, defined as the difference in the absorbance of the left (A_L) and right (A_R) circularly polarized light divided by the absorbance of non-polarized light (A) at a given wavelength as (Figure 1.12. a),

$$g_{abs} = \frac{A_L - A_R}{A} = \frac{2(A_L - A_R)}{A_L + A_R}. \quad (1.12)$$

Therefore, a system displaying a high positive or negative g_{abs} close to 2 in magnitude is considered as a close-to-ideal chiral absorbing system.

Similarly, we can estimate the strength of excited state chirality through the emission dissymmetry factor (g_{lum}) defined as the difference in the emission intensity of left (I_L) and right (I_R) circularly polarized light divided by the total emission intensity (I) at a given wavelength, expressed as,

$$g_{lum} = \frac{I_L - I_R}{I} = \frac{2(I_L - I_R)}{I_L + I_R}. \quad (1.13)$$

In most cases, after excitation, the system relaxes to the lowest excited state and emits to the ground state. Hence, the dissymmetry factor can be orders of magnitude different from that of the absorption dissymmetry factor. It turns out that the dissymmetry factor correlation between ground and excited states is an interesting quantity to monitor as we will show in Chapter 3. This correlation has been studied for many molecular systems and the results indicate that a highly rigid structure with less vibrational flexibility can provide a high correlation in ground and excited states.[116,117]

The dissymmetry factor determined from experiments can be related to the theoretical modelling of the understanding of rotational strength with,

$$g = \frac{4R}{D}, \tag{1.14}$$

where R is the rotational strength, and D is the total dipole strength (square of transition dipole moment) of the transition.[37] Here, R takes the form either in Eqn.(1.3), Eqn.(1.4), or Eqn.(1.10), depending on the origin of chirality. This expression, for instance, clearly explains the origin of high CPL signal from lanthanide complexes. The reduced electric dipole moment and large magnetic dipole moment make the resultant chiral component to be higher in emission, although the emission quantum yield of the system remains very low.

Apart from these quantities traditionally involved when looking at electronic circular dichroism of chiral structures, other analytical tools have also been developed to provide improved sensitivity. The magnetic CD (MCD) is one among the techniques that is capable of measuring signals with improved sensitivity compared to optical spectroscopy (Figure 12.a).[118] It measures the differential absorption of left and right circularly polarized light induced by a magnetic field through an effect known as the Faraday effect. MCD has been applied to study the coordination and structural geometries of many metal-organic frameworks, metal chromophores, and bioinorganic compounds.[119–121] It has also been developed for vibrational excitations in infrared (MVCD), and X-ray (XMCD) regions of molecular systems.

Fluorescence-detected circular dichroism is another method where CD is measured through fluorescence from chiral chromophores (Figure 12.b).[122] It increases sensitivity thanks to emission signals that are sensitive to the absorbance of different polarization of input light. It is, today, an efficient tool used in biological studies for studying the dynamics of chiral biomolecules of protein or nucleic acid attached to a fluorophore. It has also been applied with chromatography and electrophoresis. [123–125]

Studying chirality at the vibrational level can provide information regarding the absolute configuration of chiral molecules by measuring the differential absorption of left and right infrared circularly polarized light.[126,127] This method termed vibrational CD (VCD) has emerged as an analytical tool in less than 50 years but has shown its efficiency in determining the structural configuration of many peptides and saccharides (Figure 1.12.c).[128,129] It has evolved over the years as a powerful tool in identifying chiral interactions in supramolecular organizations in biomolecules such as DNA fragments and amyloid fibrils.[130–132]

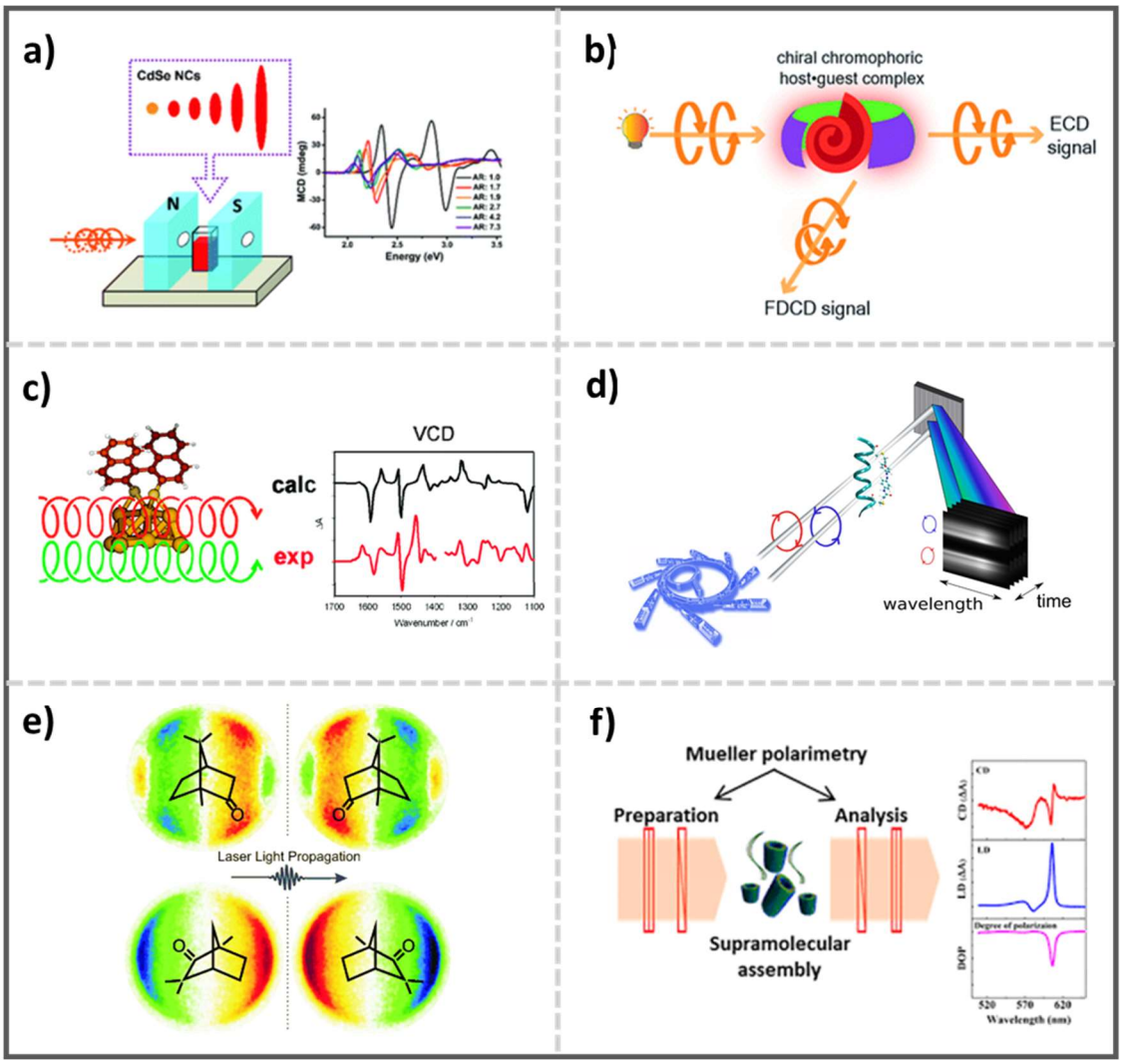

Figure 1.12: *Summary of different emerging spectroscopic methods employed for analysing the chiral signatures of molecular and supramolecular structures, such as a) magnetic circular dichroism (MCD), b) fluorescence-detected circular dichroism (FDCD), c) vibrational circular dichroism (VCD), d) synchrotron radiation circular dichroism (SRCD), e) photoelectron*

circular dichroism (PECD), and e) Mueller polarimetry. Adapted with permission from ref [121,125,130,133,134,143].

Synchrotron radiation circular dichroism (SRCD) is also an emerging new technique where the high light flux from the radiation source increases sensitivity by reducing the signal-to-noise ratio (Figure 1.12.d).[135] This method also has the advantage of measuring signals at lower wavelengths providing more structural information. It is known to improve analysis of the secondary structure of proteins, monitoring protein folding and associated kinetics, and drug-target interactions. This emerging method has great potential in studying complex protein-protein interactions and their complexations.[133,136–138]

Photoelectron circular dichroism (PECD) is yet another promising field where the chirality of molecules with low dissymmetry factor is detected through a photoionization process (Figure 1.12.e).[134,139] This technique is based on the concept that the photoionization of a chiral molecule is different for left and right circularly polarized light, and the dissymmetry is defined as the difference between the photoelectron angular distribution for different helicity of polarized light.[140–142] It uses either a synchrotron radiation source or a pulsed laser source for ionizing the sample.

Among this wide range of chiral characterization techniques employed for studying chiral molecules, the most widely used method is the electronic CD which easily determines the ground and the excited state chiroptical properties of a wide range of molecular and supramolecular species. Although the technique is widely accepted as an efficient characterization method, there are still several limitations sometimes overlooked which can bring various artefacts leading to improper interpretations of the chiroptical signals. Addressing these artefacts is of extreme importance, especially for synthetic chemists, who require the intrinsic characterization details of the molecular systems under study to optimize their structural parameters for the targeted functionalities. This concern for artefact-free polarimetric analysis has attracted much interest at the crossroad of optics and supramolecular chemistry. Mueller polarimetry with its unique signal processing strategy gained attention in recent years due to its excellence in eliminating artefacts by simultaneously monitoring polarization signals and its adaptive flexibility to multiple measurement strategies (Figure 1.12.f).[7,143] In the next Chapter, we will discuss in detail these artefacts and the associated methodologies one can develop for artefact-free signal characterization using Mueller polarimetry.

1.7 Conclusions

In this Chapter, we discussed the origins of the concept of chirality that emerged in different contexts attracting a wide interest from various research fields in general science. Beginning as a characteristic signature of asymmetry, chirality grew as a key concept central to many endeavours, ranging from exploring homochirality to diverse functional applications. These research interests closely involve developing molecular and supramolecular structures that are easily manipulated for specific functionalities. This development of synthetic strategies requires proper experimental characterization methods and theoretical understanding of chiral light-matter interactions. In this Chapter, we briefly discussed the experimental methods, theoretical advancements, and characterization techniques commonly used and implemented to understand the origin of chirality in various molecular and supramolecular systems. Research in these fields gave rise to the concepts of point chirality (Section 1.5.1), axial chirality (Section 1.5.1), induced chirality (Section 1.5.2) and exciton-coupled chirality (Section 1.5.3). These concepts are also briefly discussed in this Chapter. Along with these theoretical advancements, characterization methodologies also evolved where sensitivity and artefact-free measurement techniques were of particular interest. This increased demand for signal sensitivity and artefact-free characterization is an undeniable source of limitation in conventional methods, pushing research interest to explore other alternative techniques, where optics ties the knot with polarimetry, and thereby chirality. We also discussed in this Chapter these advancements in analytical methods, emphasizing the relevance of Mueller polarimetry as the state-of-the-art method providing artefact-free chiroptical signals.

Chapter 2

Mueller polarimetry: from polarization artefacts to artefact-free analysis

In this Chapter, we discuss the experimental artefacts one can be confronted within the polarimetric characterization of molecular and supramolecular structures, and explain how the Mueller formalism is helpful in yielding artefact-free measurements. These artefacts stem either from the intrinsic properties of the sample combining simultaneously occurring polarization responses, or from nonideal optics and instrumentation features. In addition, artefacts in the excited state can arise due to inner-filtering effects associated with the re-absorption of light. These artefacts can easily be accounted for using Mueller polarimetry. We thus present the general protocols carried out to generate the Mueller matrices of the samples, and the necessary correction methods followed for the artefact-free characterization. We also present different polarimetric observables extracted from the samples, within the ground and the excited states, that are not easily accessible using conventional methods, precisely because of artefacts caused by anisotropy and re-absorption effects.

2.1 Introduction

With the ever-growing interests in studying the stereochemical and conformational properties of molecular and supramolecular structures, polarimetric characterization methods have moved forward over the recent years. This progress has, for instance, shown that CD measurements can easily be spoiled by potential artefacts that can affect the chiroptical analysis. To account for this issue, careful measures were put forth in the early 1960s warning the experimentalists.[144] This origin of artefacts limited polarimetric characterization in inhomogeneous and anisotropic samples in solution and solid states. This was initially realized by Disch and Sverdlik in 1969, which later influenced the coining of the terms *true* CD (CD_{true}) and *measured* or *apparent* CD (CD_{app}).[144–146] Here, CD_{true} corresponds to the intrinsic CD spectrum devoid of artefacts, while CD_{app} corresponds to the CD signal measured using a conventional spectrometer.

Artefacts in polarimetric analysis originate from the intrinsic properties of the sample or the imperfections of the optics and electronics involved in the experiments.[147] Artefacts due to inhomogeneity and scattering have been observed in polyalanine films as early as 1970.[148] Additionally, chiroptical artefacts arise mainly when a system shows strong linear dichroism (*LD* (which is *LD* in the horizontal / vertical axes), *LD′* (which is *LD* in the $\pm$45 axes)) combined with linear birefringence (LB (which is *LB* in the horizontal / vertical axes), *LB′* (which is *LB* in the $\pm$45 axes)) which can manifest as circular dichroism as light passes thr ough the solution. In such a case, the CD_{app} can be expressed as,

$$CD_{app} \approx CD_{obs} + \frac{1}{2}(LD' \cdot LB - LD \cdot LB').^{145,149} \quad (2.1)$$

This interplay of LD and LB has been analysed in solutions of J-aggregates of thiocyanine (5,5'-dichloro-3,3'-disulfopropyl thiocyanine) molecules.[150] The apparent CD initially thought as true CD observed from achiral chromophores bound to cellulose in gel film was later proved to originate from LD and LB contribution, as reported by Shindo et. al.[151] Furthermore, the instrument-specific optical responses have to be properly corrected, especially if the instrumentation includes a photoelastic modulator (PEM) and lock-in-amplifier, that adds on similar LD-LB artefacts as suggested by Hipps and Crosby in 1975.[152] Similarly, artefacts in CPL measurements were also pointed out by Dekkers et.al, in 1985.[153,154] Here again these artefacts in CPL arise due to *leaking* of linear polarization in luminescence and also artefacts induced by lock-in-amplifiers. This concern would not be an issue if the

molecular system is composed of spherical emitters or show negligible linear polarization. Nevertheless, all this body of work shows that the experiments have to be properly evaluated before drawing any conclusions regarding their chiroptical features.

Once the artefact issues in chiral characterization were stressed, many in the field began exploring the possibility to formulate methods aimed at extracting intrinsic chiral signals from optically complex materials. Y. Shindo pioneered such studies in determining the problems originating from the presence of LD, LB, and CB in solid samples using conventional spectrometers, incorporating Mueller formalism.[147,155] Measuring LD along with CD was put forth as an important check for artefacts. Measurements performed by rotating the samples, and measuring the front and back sides of sample films, were also suggested as ways to inspect for artefacts.[149] Further, R. Kuroda showed ways to extract artefact-free CD measurements from solid samples with high LD and LB.[156,157] Later, Bart Kahr and Oriol Arteaga expanded these discussions and showed the importance of artefact-free characterization using Mueller polarimetry.[158–161] In addition, the concepts were also expanded to extract polarimetric signatures in the excited state and also to determine the intrinsic fluorescence anisotropy of materials.[162,163]

Today, Mueller polarimetry serves as a vital tool to characterize chiral structures, and to provide intrinsic artefact-free polarimetric observables both in the ground and excited states of molecular and supramolecular structures. This method resides at the heart of the experimental results presented in this thesis. Therefore, in this chapter, we focus on discussing the Mueller formalism, and the protocol followed for the polarimetric measurements reported in this thesis. We also give a brief description of the experimental set-up and the correction protocols followed for extracting different artefact-free polarization responses of the materials studied in this thesis.

2.2 Experimental setup for Mueller polarization measurements

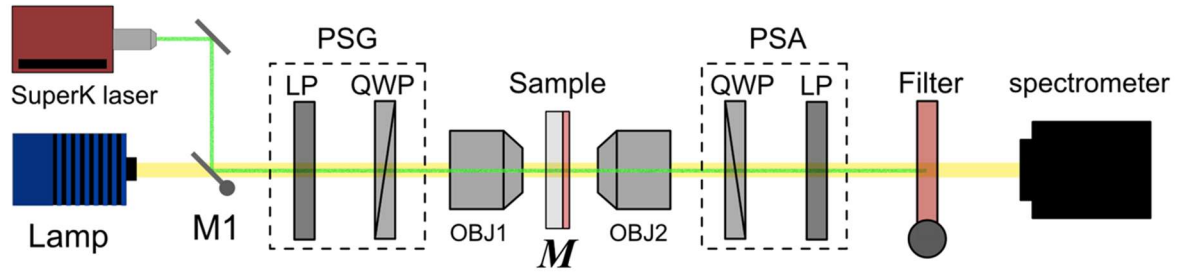

Figure 2.1: *Schematic drawing of the optical setup used in the laboratory for the transmission and emission Mueller matrix measurements performed in this thesis. A flippable mirror M1 allows light sources to be changed from white light to supercontinuum laser depending on the type of measurement performed. A flippable long pass variable filter is used for emission Mueller matrix determination to eliminate any stray signal from the excitation light. LP represents linear polarizers, and QWP represents quarter wave plates. Objective lenses (OBJ1 and OBJ2) are used for focusing the light on a microscopically small region of the sample. Details like mirrors and other lenses are omitted for clarity.*

The optical setup used for the Mueller measurements in this thesis is shown in Figure 2.1. It is grounded on the setup built previously in the laboratory, in particular through the Ph.D. thesis of Minghao Li and Jerome Gautier.[164,165] This experimental setup works in the visible spectral range from 400 nm to 800 nm.

Here, we use a Tungsten-Halogen light source from Ocean Optics, HL2000LL for the transmission studies. The light beam is focused on the sample using a Nikon extra-long working distance (ELWD) 20x (NA = 0.4) objective, and the output light is collected using a Nikon ELWD 40x (NA = 0.6) objective. The main component of the Mueller setup consists of a Polarization State Generator (PSG) and a Polarization State Analyser (PSA). They both constitute a fixed linear polarizer (Glan-Taylor linear polarizer, Thorlabs GT10) and a rotating quarter plate (Thorlabs AQWP05M600) working in the optical range of 400 nm to 800 nm. The PSG generates a specific polarization state sent through the sample and the PSA then analyses the transmitted polarization state of the light. Finally, the output light is sent to a spectrometer (Teledyne Princeton Instrument, SpectraPro HRS-300) coupled to a CCD camera

(Teledyne Princeton Instrument, PIXIS 1024) to record polarization-dependent transmission spectra.

When performing emission Mueller measurements, we use the same experimental setup, but involving a supercontinuum laser source (NKT photonics) to excite the sample. In addition, we use a flippable long-pass filter to prevent the excitation light from reaching the detector. We use the same set of objectives and adjust their positions to collect the maximum intensity of emitted light while minimizing inner-filtering effects that can induce strong artefacts in the measured signals. This aspect of inner-filtering effect will be discussed later in this Chapter. Neutral density filters are used to adjust the intensity of the light source. The exposure time and number of scans are varied depending on the signal strength collected from the sample. The experimental timeframe ranges from 10 min to 1 hr depending on the number and the type of Mueller measurement (transmission or emission), which will be discussed later in the thesis.

2.3 Stokes-Mueller formalism

In this Section, we briefly describe the Stokes-Mueller formalism employed when performing experiments and analysing our data.

2.3.1 General description

The mathematical framework implemented in polarization optics was initially established with the Jones formalism, which applies well to fully polarized light. However, it has limitations within a real experimental situation where light can be partially polarized or non-polarized.[166,167] In this regard, the Stokes formalism was put forth by G. G. Stokes to describe the intensity and polarization properties of light in a vectorial form, called the Stokes vector, which is a more convenient approach for experimental situations.[168,169] The Mueller formalism, developed by Hans Mueller in the 1940s postulates a general linear relation between input and output Stokes vector in an optical medium (Figure 2.a).[170] This relation takes the mathematical form of a Mueller matrix that can be constructed to handle all polarization states of light, before and after it has interacted with matter (Figure 2.b).

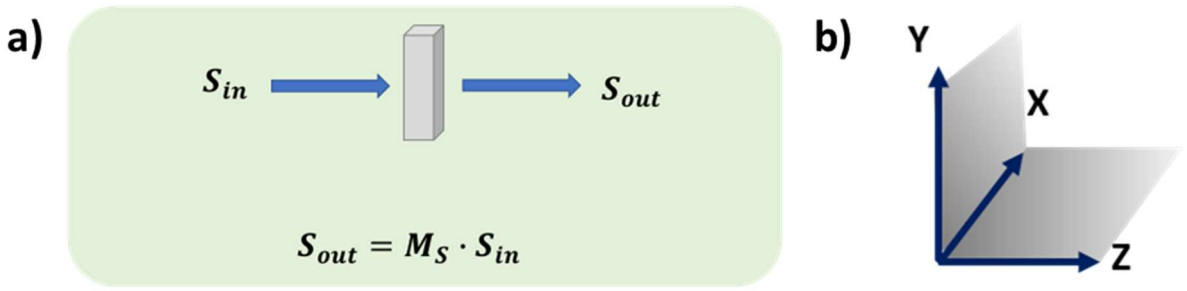

Figure 2.2: *a) Representation of Stokes vector of input ($\vec{S}_{in}$) and output ($\vec{S}_{out}$) beam of light. b) Coordinate axes in the experimental frame.*

We begin by setting up a reference frame (laboratory frame) with which we can identify the polarization states of the light. Within this coordinate frame, we define the Stokes vector as,

$$\vec{S} = \begin{pmatrix} S_0 \\ S_1 \\ S_2 \\ S_3 \end{pmatrix} = \begin{pmatrix} I_0 \\ I_V - I_H \\ I_{45} - I_{-4} \\ I_l - I_r \end{pmatrix} \tag{2.2}$$

where I_0 is the total intensity of light, $I_V - I_H$ is the difference of intensity between the vertical (Y-axis) and the horizontal linearly polarized light (X-axis), $I_{45} - I_{-4}$ is the intensity difference between the +45 and -45 linearly polarized light in the X-Y plane, $I_l - I_r$ is the intensity difference between the left and right circularly polarized light.

For a light beam interacting with a medium, we can define the output Stokes vector in terms of the input Stokes vector in the following manner.

$$\vec{S}_{out} = M \cdot \vec{S}_{in}, \tag{2.3}$$

where M is called the Mueller matrix which contains all the polarimetric information of the medium that was responsible for modifying the input polarization state of the light (Stokes vector).

This definition of Stokes vector imposes the Mueller matrix to be a 4×4 matrix as,

$$M = \begin{pmatrix} m_{00} & m_{01} & m_{02} & m_{03} \\ m_{10} & m_{11} & m_{12} & m_{13} \\ m_{20} & m_{21} & m_{22} & m_{23} \\ m_{30} & m_{31} & m_{32} & m_{33} \end{pmatrix} \tag{2. 4}$$

In general, these 16 matrix elements are independent and carry unique polarimetric information about the system. The symmetries of the medium can force specific constraints extremely important for extracting the essential observables, as we will discuss further down in this Chapter.

2.3.2 Multiplicative nature of Mueller matrices

An interesting aspect of the Stokes-Mueller formalism is its multiplicative nature. For a medium constituting N successive systems, it is possible to consider each with its own Mueller matrix M_k, $k \in < 1, N >$, so that the total Mueller matrix of the medium can be expressed as,

$$M = \prod_{k=1}^{N} M_k \tag{2.5}$$

This multiplicative nature of Mueller matrix can be extremely useful when dealing with systems that are layered (or formed by multiple components) where light sequentially interacts with each of them. We will exploit this multiplicative nature when studying the polarimetric properties of materials, as discussed further in this Chapter.

2.4 Measurement analysis

In this Section, we describe the mathematical framework based on the Stokes-Mueller formalism that helps in extracting artefact-free polarimetric properties of a sample. Considering the experimental setup explained in Section 2.2, the full Mueller matrix that modifies the input Stokes vector can be considered as the product of Mueller matrices associated with PSG, $M_{PSG}(\theta_1)$, the unknown Mueller matrix of the sample (considering no objectives), M_x, and the Mueller matrix of PSA, $M_{PSA}(\theta_2)$. Hence, the output Stokes vector can be expressed as,

$$\vec{S}_{out} = M_{PSA}(\theta_2) \cdot M_x \cdot M_{PSG}(\theta_1) \cdot \vec{S}_{in} \tag{2.6}$$

The intensity of the output Stokes vector can then be expressed in terms of the polarization states generated at PSG (g_{j0}) and PSA (a_{0i}) at various angle combinations. Hence, S_{out} will take the form,

$$S_{out} = \begin{pmatrix} a_{00} & a_{01} & a_{02} & a_{03} \end{pmatrix} \cdot \begin{pmatrix} m_{00} & \cdots & m_{03} \\ \vdots & \ddots & \vdots \\ m_{30} & \cdots & m_{33} \end{pmatrix} \cdot \begin{pmatrix} g_{00} \\ g_{10} \\ g_{20} \\ g_{30} \end{pmatrix}. \tag{2.7}$$

Therefore, the transmitted signal intensity measured can be expressed as,

$$S_{out}^{k} = \sum_{j=0}^{3} \sum_{i=0}^{3} a_{0i}^{k} g_{j0}^{k} \, m_{i,j} \tag{2.8}$$

where k ranges from 1 to 16 measurements. The Mueller matrix elements can then be arranged in a 16-dimensional column vector, X_m. The parameters a_{0i} and g_{j0} are collected in a matrix A_m, and the intensity for different angle combinations is combined in the column vector, I_m. In this manner, we can express the above equation as,

$$I_m = A_m \cdot X_m \tag{2.9}$$

In our experiments, we perform 64 measurements and over-determine these elements to reduce the experimental error. Therefore, the final expression we employ to generate the Mueller matrix elements is,

$$X_m = (A_m^T \cdot A_m)^{-1} A_m^T \cdot I_m \, . \tag{2.10}$$

To measure the 64 angle combinations, we begin from the cross-polarized state where the fast axis of PSG and PSA are aligned with the polarizer in PSG. From this position, we sequentially rotate each of the QWPs 7 times with a step size of angle 22.5°.

This measurement will give the combined polarimetric response of the PSG, sample, and PSA. It is then important to remove the Mueller matrix of PSG and PSA to extract the Mueller matrix of the sample. The ideal way to correct for these additional elements is to determine the polarimetric responses of the experimental setup without the sample. But, before performing such corrections and Mueller measurements, it is important to calibrate the polarizers and quarter-wave plates. We now present the calibration protocols we have been using for the Mueller matrix measurements.

2.5 Measurement protocols

In this Section, we describe the protocol followed for the Mueller polarimetric measurements that include the calibration of linear polarizers and the quarter-wave plates. In addition, we discuss the correction methodologies used to remove the Mueller matrix associated with the experimental set-up (PSG, PSA, reference) and the optical response of potential artefacts when characterizing the properties of a material.

2.5.1 Calibration of the linear polarizers

Calibration of the linear polarizers requires bringing the two linear polarizers in PSG and PSA in orthogonal positions. The polarizer in the PSG being fixed, this calibration thus reduces to bringing the polarizer in PSA orthogonal to the polarizer in PSG. This procedure will correspond to testing the Malus' law for a real polarizer where the intensity of transmitted light is recorded as a function of the angle between the two polarizers.

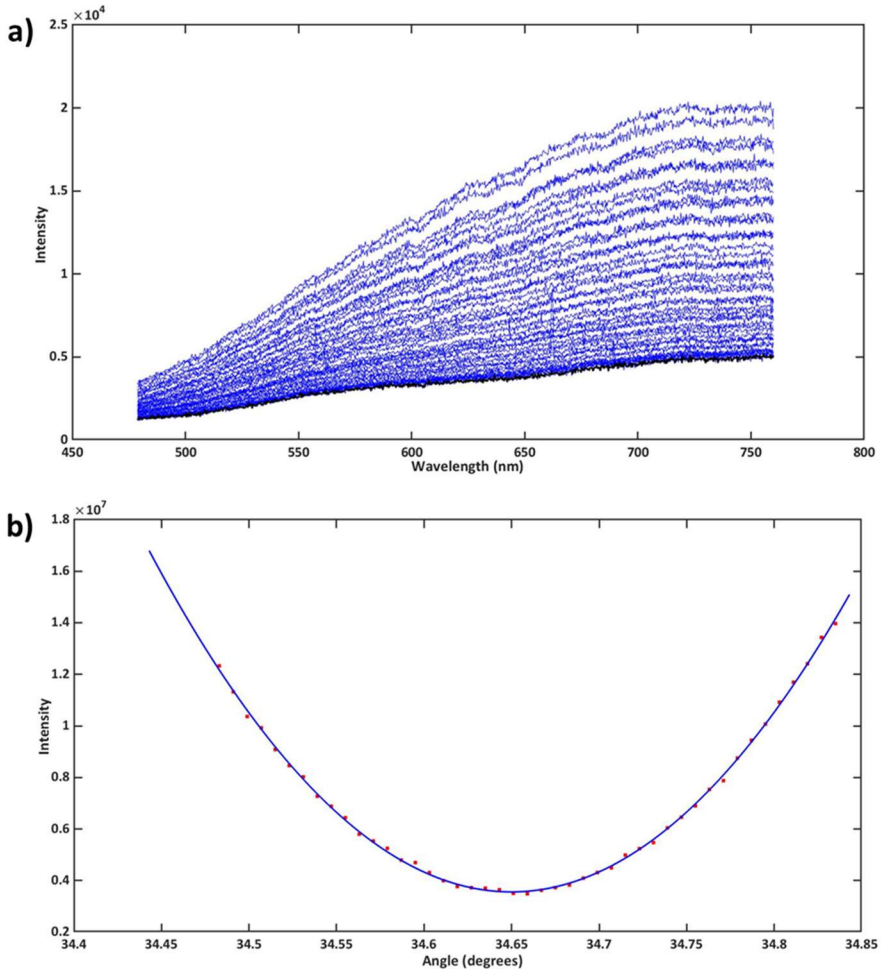

Figure 2.3: *a) Spectra of transmitted light depending on the angle between the two linear polarizers in PSG and PSA. The black trace represents the minimum intensity among the whole ensemble of spectra. b) Scatter plot of intensity (are under the graph of (a)) for various angles (red) and the corresponding parabolic fit of the Malus' law (blue) to obtain the angle between the polarizers corresponding to the minimum intensity.*

Rotating the polarizers and recording the intensity to find the minima is the ideal method to identify the orthogonal orientation of the polarizers. In our experiments, we initially find a possible range of angles within $\pm 0.4°$, where the minima resides. The polarizer in PSA is then rotated within this range with an interval of $0.008°$, and the intensity is recorded for

every angle (Figure 3.a). This intensity is then modelled by a parabolic function of angle (the Malus' law) (Figure 3.b), and the minima of the parabola is identified as the angular position of the polarizer in PSA when it becomes orthogonal to the fixed orientation of the linear polarizer in PSG.

2.5.2 Calibration of the QWPs

Calibration of QWPs requires modelling them as linear retarders and determining their mean fast axis orientation, ellipticity, $\varepsilon(\lambda)$, and retardance, $\delta(\lambda)$. These parameters are wavelength-dependent and, therefore, require compensation for this wavelength dependency throughout the spectral measurement. Here, we use the homogeneous elliptic birefringent model (HEB) to calibrate the QWPs.[171] To determine the mean fast axis orientation, here again, we need to rotate the QWPs within a range of angles. In a similar way as the calibration of the polarizers, here we place one of the QWPs (one in the PSG) between the calibrated polarizers and find the range of angles within which the intensity reaches its minimum by rotating the QWP (in PSG) with a step size of $0.008°$. This intensity for every angle is then plotted as a function of wavelength, and the angle corresponding to the minimum intensity for every wavelength is determined. This angle corresponds to the mean fast axis orientation ($\bar{\theta}_1$) of the QWP in PSG (Figure 2.4.a). To account for the wavelength-dependent variation in transmitted intensity, we choose an averaged angle and determine the parameter $\Delta\theta_1(\lambda) = \theta_1(\lambda) - \bar{\theta}_1$ (Figure 2.4.b). This parameter is introduced in the analysis to compensate for the wavelength dependent changes in defining the QWPs. This procedure is repeated for the other QWP (in PSA) to determine its mean fast axis orientation, $\bar{\theta}_2$, and the parameter accounting for wavelength dependency, $\Delta\theta_2(\lambda) = \theta_2(\lambda) - \bar{\theta}_2$. To determine the ellipticity and retardance parameters for each QWP, we perform a Mueller measurement without any sample between the PSG and PSA. We call this the "empty Mueller matrix ".

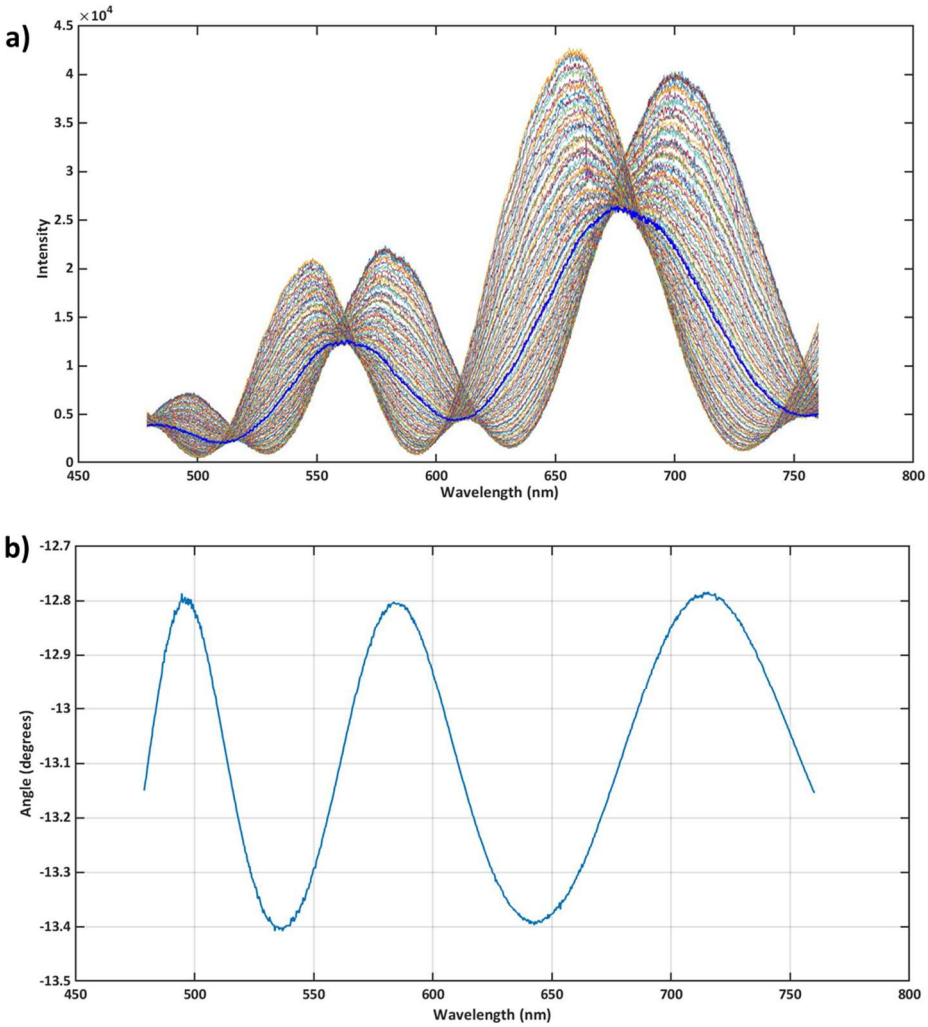

Figure 2.4: *The spectra of transmitted light depending on the angle rotated in the QWP. The blue trace represents the spectra corresponding to the minimum intensity. b) Spectra showing the wavelength-dependent variation of the fast-axis of QWP.*

In such an "empty configuration", we expect the Mueller matrix to be proportional to the identity matrix, I_4, considering that the polarization of light does not vary in air. This leads us to fit the measured Mueller matrix to the identity matrix based on the HEB model for a QWP to extract the ellipticity and retardance for the two QWPs (see ref [21,28] for more details). This empty Mueller matrix will be used to determine the Mueller matrix of the sample and its corresponding reference by eliminating the polarimetric response of the optical setup. An example of an empty Mueller matrix is given in Figure 2.5, which shows values very close to an identity matrix, indicating that the experimental setup does not add any polarimetric modifications to the light beam.

When performing a transmission Mueller measurement using objectives, it is important to verify whether the objectives add any polarimetric effects. Therefore, we perform a Mueller

measurement with the objectives (but without any sample between the objectives). We use this measurement as the empty Mueller matrix. Therefore, we can write (assuming the similarity between objectives),

$$M_{empty}^{1/2} = M_{OBJ1} = M_{OBJ2}. \quad (2.11)$$

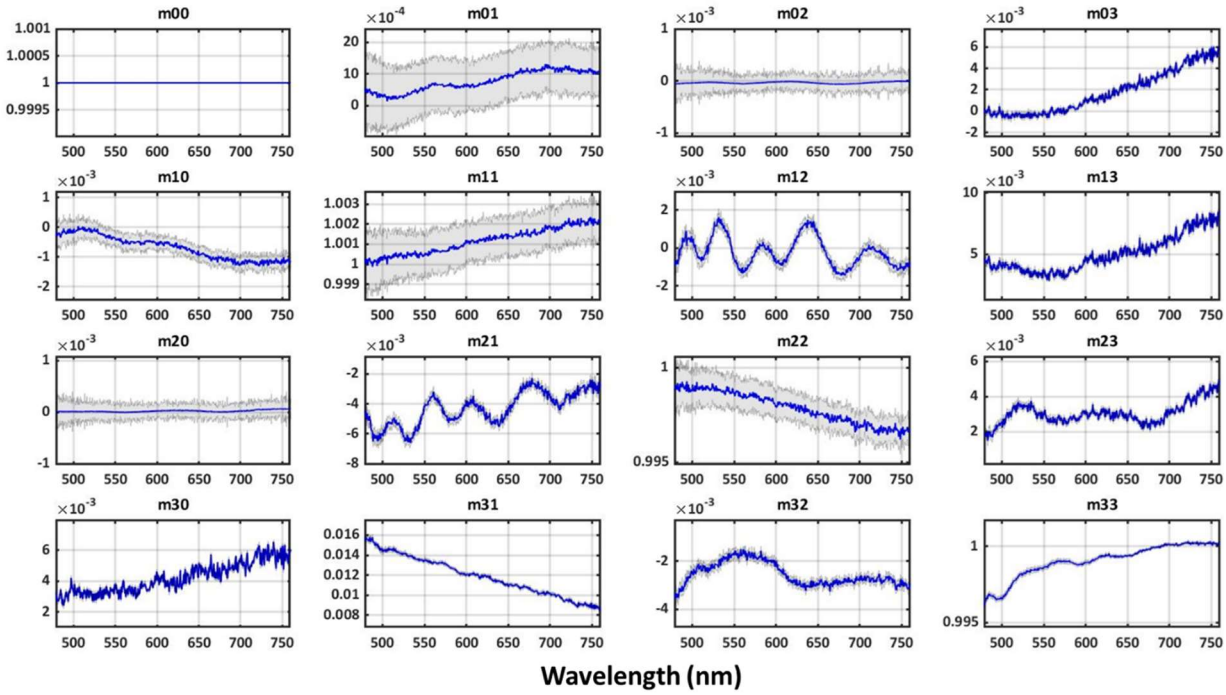

Figure 2.5: *Empty Mueller matrix showing values very close to an Identity matrix. The grey-shaded region represents the error bar for each element estimated through the standard deviation calculated from the empty Mueller matrix.*

2.5.3 Correction for reference

In most cases, depending on the sample, polarimetric characterization requires a correction for reference which is either a cuvette when studying a solution or a bare substrate when measuring a film (Figure 2.6).

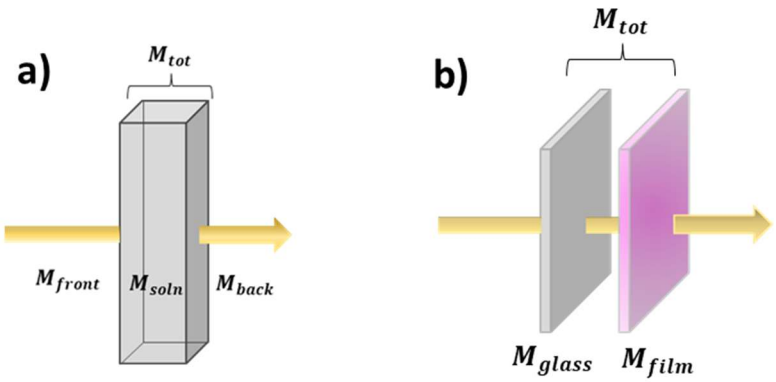

Figure 2.6: *Mueller matrix measurements through a solution (a), and film state (b), where the total Mueller matrix (M_{tot}) is divided into different components involving the Mueller matrix of the material of interest and the Mueller matrix of the reference.*

When characterizing a sample constituting a solution, we must correct for the two sides (*front* and *back*) of the cuvette that interacts with the light beam independently before and after the solution. The Mueller matrix of the sample, in this case, can be expressed as,

$$M_x = M_{front}^{-1} M_{tot} M_{back}^{-1} \tag{2.12}$$

To perform this correction, we measure the Mueller matrix of the cuvette (filled with the solvent if required) without any material of interest and eliminate this contribution from M_{tot}. On the other hand, if the sample is a film, we measure first the unknown Mueller matrix as the product of Mueller matrices of the substrate glass (M_{glass}) and the film (M_{film}), as shown in Figure 2.6. Hence, the unknown Mueller matrix of the sample can be expressed as,

$$M_{tot} = M_{film} \cdot M_{glass} \tag{2.13}$$

By performing a reference measurement with a bare glass substrate, we measure first the matrix, M_{glass}, from which the Mueller matrix of the molecular film, M_{film} can be estimated as,

$$M_{film} = M_{tot} \cdot {M_{glass}}^{-1} \tag{2.14}$$

An example of transmission Mueller matrix of a bare glass substrate is presented in Figure 2.7. The matrix elements are very close to an identity matrix indicating that the glass substrate does not induce any strong modifications in the polarization of the transmitted light.

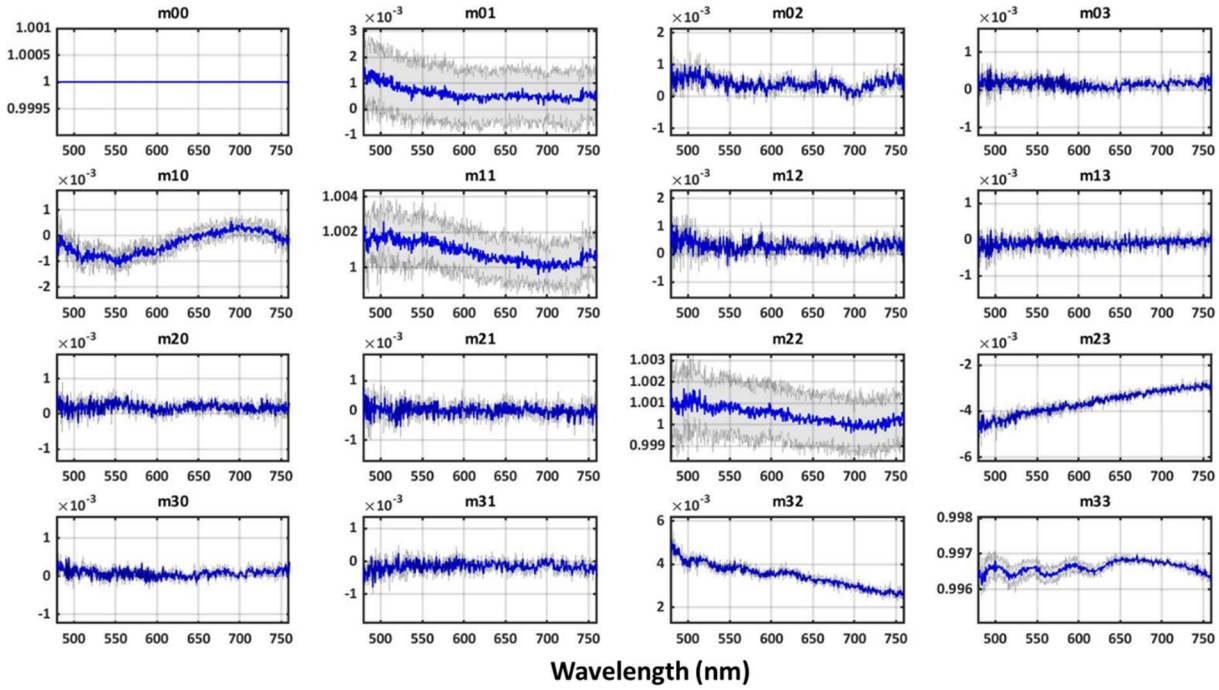

Figure 2.7: *Mueller matrix of glass as a reference for a film measurement. This Mueller matrix has values very close to an identity matrix, indicating that the glass substrate adds no polarimetric modifications to the input light. The grey-shaded region represents the error bar for each element estimated through the standard deviation calculated from the empty Mueller matrix.*

2.5.4 Transmission Mueller matrix

For performing transmission Mueller matrix evaluation, we place the sample in between the PSG and the PSA, as shown in Figure 2.1, and rotate the QWPs through 64 angle combinations to obtain one Mueller matrix. We usually perform a minimum of 3 Mueller matrices and take the average of all the matrices. From this configuration, if the Mueller matrix obtained is depolarized (diagonal elements with values much lower than 1), we follow a differential decomposition method (see ref[164] for more details) to extract the different observables corresponding to the ground state polarimetric properties of the material such as linear dichroism in the horizontal /vertical axes (LD), and ± 45 axes (LD'), linear birefringence (LB, LB'), circular dichroism (CD), circular birefringence (CB), and the degree of polarization (DOP).[172–175] This decomposition method allows us to directly extract the essential polarimetric properties of the material from the matrix, which are presented in Figure 2.8. From this matrix, the DOP is extracted from the matrix elements (m_{ij}) as,

$$DOP = \frac{\sqrt{\sum_{ij} m_{ij}^2 - 1}}{\sqrt{3}}. \quad (2.15)$$

$$M = \begin{pmatrix} A & -LD & -LD' & CD \\ -LD & A & CB & LB' \\ -LD' & -CB & A & -LB \\ CD & -LB' & LB & A \end{pmatrix}$$

LD: Linear Dichroism
LB: Linear Birefringence
CD: Circular Dichroism
CB: Circular Birefringence

Figure 2.8: *Polarimetric observables that can be read from a transmission Mueller matrix after differential decomposition. Here, after differential decomposition of the transmission Mueller matrix, we get A=1.*

2.5.5 Emission Mueller matrix

As described above, an emission Mueller measurement can also be performed in the transmission configuration using a white laser source (with laser power around 1.7 mW) coupled to a filter with a minimum bandwidth of 10 nm for exciting the sample (Figure 2.1). In the exact same manner as the transmission configuration, the PSG is used to generate a specific polarization state of the input laser beam, and the PSA is used to analyse the polarization state of the *emitted* light.

In this configuration, therefore, the emission Mueller matrix, M_E, relates the polarization state of excitation (S_{in}), at a wavelength, λ_p, to the polarization state of photoluminescence (S_{out}) at a wavelength, λ_{pl}, as follows:

$$\vec{S}_{out}(\lambda_{pl}) = M_E(\lambda_{pl}, \lambda_p) \cdot \vec{S}_{in}(\lambda_p) \quad (2.16)$$

However, it is important to stress here that the total Mueller matrix measured in this configuration is composed of three different parts (see Figure 2.9),

$$M_{tot}(\lambda_{pl}, \lambda_p) = M_{T_{pl}}(\lambda_{pl}, \lambda_p) \cdot M_E(\lambda_{pl}, \lambda_p) \cdot M_{T_p}(\lambda_p) \quad (2.17)$$

where M_{Tp} is the transmission Mueller matrix of the medium that depends on the excitation wavelength, λ_p. M_{Tpl} is the transmission Mueller matrix of the emitted light through the same medium that depends on the emission wavelength, λ_{pl}.

This expression reveals the importance of performing a proper correction procedure with transmission Mueller matrix to extract artefact-free emission Mueller matrix. This correction procedure is extremely important to perform on materials that have overlapping

absorption and emission spectra (zero Stokes shift) from which re-absorption of emitted light becomes an issue. In such a case, indeed, the polarimetric signals can be modified depending on the strength of re-absorption. Eventually, this leads to unreliable measurements for excited state polarization studies until a correction for such re-absorption effects is performed on the sample.

2.5.6 Correction for re-absorption

For materials characterized to show large Stokes shifts, the polarization properties of the emitted light are not much affected by re-absorption. In this case, a correction methodology is not necessarily required. However, for materials such as Cyanine aggregates of C803, that do not display any Stokes shift, the polarization signals can sensibly be impacted by re-absorption.[176] This phenomenon termed as the "inner filtering effect", constitutes a serious problem for polarimetric analysis of the excited state. This problem of polarization modifications through re-absorption in C8O3 aggregates in solutions has been studied in detail by Minghao Li in his Ph.D. He showed that the polarimetric signals can be varied depending on the optical pathlength, suggesting to reduce the pathlength of the samples in polarimetric analyses and thereby controlling the impact of the inner filtering effect.[164]

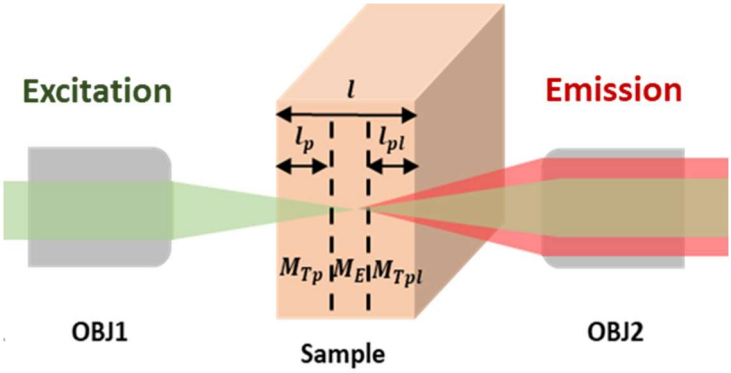

Figure 2.9: *Measurement of an emission Mueller matrix showing the decomposition of the total Mueller matrix into that of a transmission and emission Mueller matrix dependent on the path length of the light through the sample.*

The total Mueller matrix, M_{tot} in emission can be written in terms of optical pathlength as,

$$M_{tot}(\lambda_{pl}, \lambda_p) = exp\,[l_{pl} \cdot N_M(\lambda_{pl})] \cdot M_E(\lambda_{pl}, \lambda_p) \cdot exp\,[l_p \cdot N_M(\lambda_p)] \qquad (2.18)$$

where, N_M is the differential Mueller matrix (matrix extracted from the transmission Mueller matrix as shown in Figure 2.8), M_t and, l_{pl} and l_p are optical path lengths as indicated in Figure 2.9. In our experiments, we use this correction methodology, especially in Chapter 3 of this thesis, where this method will be discussed in more detail.

2.5.7 Correction for photochemical modifications affecting emission intensity

When a molecular system is excited using a light source, the high energy received can induce photochemical modifications in the system that eventually reduce the resulting emission intensity collected in experiments. Usually, one invokes a photobleaching process where the fluorophore loses its ability to emit due to chemical changes.[177–179] However, in our experiments, characterizing C8O3 aggregates, we noticed that in some cases, the collected emission intensity sometimes increases slightly instead of diminishing. Our experiments are usually performed after the laser is stabilized (a minimum of 2 hrs of waiting time). Therefore, the increment that we observe is not likely to have occurred due to the intensity variations in the excitation laser source.

Emission enhancement as a result of photobrightening has been studied in C8S3 aggregates originating from lattice deformations but this property has not been studied in other Cyanine-based aggregates.[180] This phenomenon of increasing intensity observed in C8O3 aggregates is intriguing in this regard and requires more studies to understand the precise mechanism at play. However, irrespective of the source of these varying signals, it becomes a serious issue when performing an emission Mueller polarimetric analysis. This issue arises because Mueller polarimetry relies on the fact that all the intensity variations originate only from the changes in the polarization states modified at the PSG and PSA. Therefore, any intensity variation due to other physical or chemical modifications of the material can bias improperly the analysis. We have noted that the increase or decrease in intensity is more pronounced for films when the laser is focused on a specific point for a long time, while studies in solution state were much less affected thanks to diffusion.

To account for such unwanted intensity modifications, it is important to analyse the evolution of the emission signal within the measurement time frame for the laser power (close to 1.7 mW) chosen in the experiments. To perform this analysis, we measured the emission spectra of the sample at a particular excitation wavelength for 6 hours along with monitoring

the laser stability. These control experiments showed that within the time frame of our measurement (20 min-1 hr for acquiring 4 Mueller matrices), the intensity variations are not too important to impact sensibly the results. However, it remains true that a proper experimental methodology for polarimetric studies requires correcting for such intensity variations. Therefore, we use a fitting method based on the knowledge that photobleaching exponentially evolves.[178,179] Similar exponential fit can be used to account for intensity growth. In addition, we were able to reduce these intensity changes by using optical density filters and by reducing the excitation laser power. The spectral changes before and after correction for such photochemical modifications are shown in Figure 2.10. This comparison demonstrates the efficiency of our corrections.

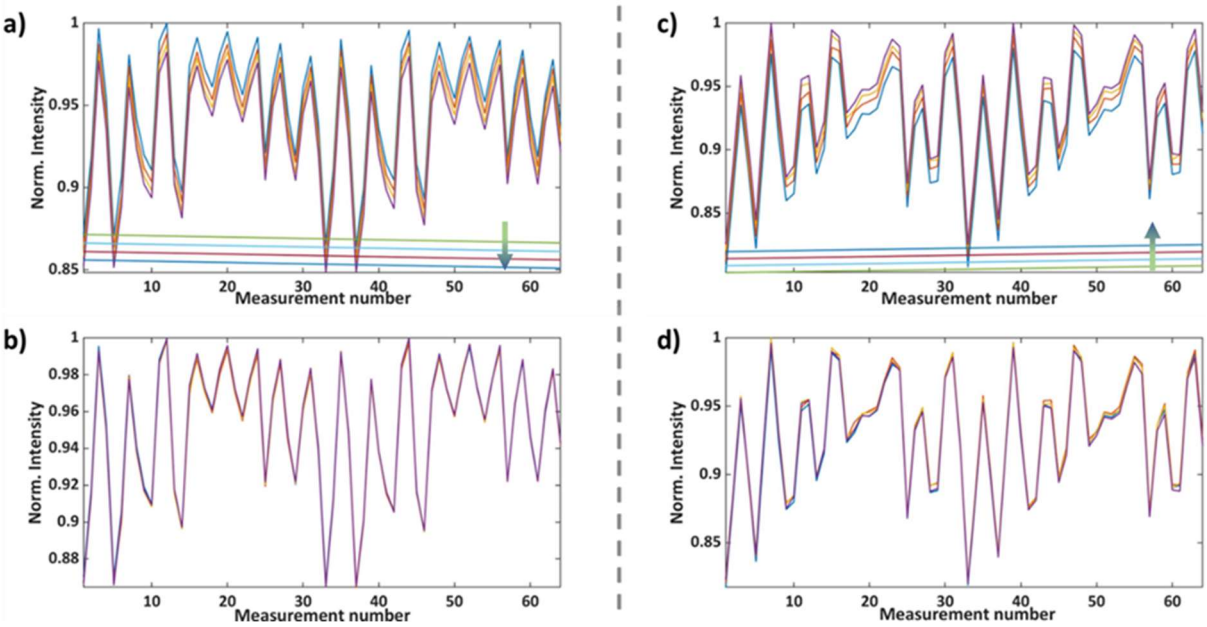

Figure 2.10: *Intensity plots for each measurement for a specific angle combination of the PSG and PSA. The superimposed zig-zag traces represent all 4 Mueller matrices measured over the whole experiment. The straight lines are drawn connecting two intensity minima to distinguish between the bleaching and enhancement of the emission intensity. a) Spectra before correction showing intensity drop (bleaching) during the measurement. b) Spectra after correcting for bleaching. c) Spectra before correcting for enhancement in intensity. d) Spectra after correcting for enhancement. The arrows indicate the direction of intensity variations.*

2.5.8 Observables extracted from emission Mueller matrix

Once the correction methodologies are properly accounted for, we obtain information on both the ground and the excited state properties of the material, separated into different elements of the matrix such as linearly polarized luminescence (LPL, LPL'), circularly polarized luminescence (CPL), fluorescence detected linear dichroism (FDLD, FDLD'), fluorescence detected circular dichroism (FDCD) as summarised in Figure 2.11. These observables will be exploited in Chapter 4 of this thesis. Additionally, we obtain information on fluorescence polarization or anisotropy of the material from the diagonal elements of the matrix that is free from anisotropy due to orientation. [163,181,182] Furthermore, the off-diagonal elements provide information regarding dephasing or retardance effects between orthogonal circular and linear polarizations.

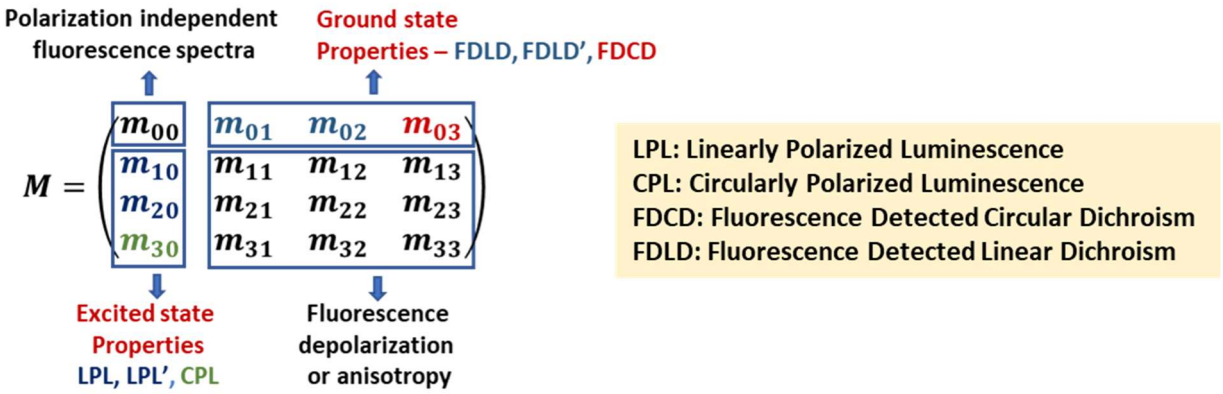

Figure 2.11: *Polarimetric observables extracted from an emission Mueller matrix.*

2.6 Conclusions

In this Chapter, we discussed about Mueller polarimetry, which is the main characterization method employed in this thesis for studying the polarimetric properties of the ground and excited states of a molecular system. We explored various potential sources of artefacts and presented an approach capable of removing artefacts appearing due to polarimetric responses that concomitantly occur in transmission such as LD, LB, CD, and CB. Similarly, for emission polarimetric analysis, LPL can affect the CPL measurements. This influence can also be accounted for using our polarimetric approach. We briefly discussed the theoretical descriptions of the Mueller formalism in defining the artefact-free polarimetric properties of the materials. Further, we explained the protocols used for the measurements, both in transmission and emission configuration. In the latter case, in addition to the artefacts due to

intrinsic polarization features, polarimetric signals can be modified through re-absorption of the emitted light, and photochemical modifications induced in the excited state. We presented their respective correction procedures also in this Chapter.

Chapter 3

Strong coupling of chiral Frenkel excitons and emergence of intense bisignate circularly polarized luminescence

In this chapter, we explore the ground and the excited state chiroptical properties of bundled C8O3 aggregates using Mueller polarimetry to show that the strong coupling of chiral Frenkel excitons yields intense bisignate dissymmetry factors in absorption and emission of the order 0.08. We use careful measures to eliminate the possible artefacts due to re-absorption, high anisotropy, and in-homogeneity of the sample to access the intrinsic properties of the tubular and bundled aggregates. With this artefact-free Mueller polarimetry, we study the correlation between the ground and the excited state chirality. We also analyse the chiroptical structure-to-property relation of these aggregates through an energy level diagram that explains the multiple emissive nature and the bisignate profile of the CD signal that would hardly be discernible with conventional polarimetric studies.

3.1 Introduction

Simple chiral molecules have been employed in various scientific domains to bring in technological advancements, especially by manipulating their emissive properties and thereby enhancing the contrast and efficiency of light-emitting diodes, developing chiral lasers and anti-counterfeit applications.[183–192] These technological developments demand materials with high luminescence dissymmetry factor, g_{lum} (see definition in Section 1.6 of Chapter 1), and high quantum yield. Simple chiral molecules show g_{lum} of the order 10^{-5} to 10^{-3} which , in fact, makes them less desirable.[193–195] However, new chiral molecular systems have recently been brought forward with exceptional chiroptical properties that can be exploited for various applications. These systems include lanthanide complexes, a wide variety of helicenes, chromophores with chiral handles, chiral polymers, etc, as briefly discussed in Section 1.3 in Chapter 1.[196–201] Among these structures, lanthanide complexes show the highest ever known g_{lum} with a value close to 1.38 due to high rotational strength as discussed in Section 1.6 in Chapter 1.[197] Although one feature demanding for an efficient CPL emitter is reached, these structures turn out to be disappointing due to their low quantum yield. Therefore, the quest for efficient CPL emitters is continued with intense research activities around the globe.

In this context of increasing the optical activity of molecular structures, there is a growing interest in molecular aggregates that are now identified as a way to tailor chiroptical properties, in particular, making use of the dynamical control that can be reached through solvent compositions and their role played in self-assembly designs.[202–204] As discussed in Section 1.5.3, in a supramolecular aggregate, neighbouring monomers undergo exciton coupling giving rise to collective excitation that delocalizes over the monomers in the self-assembled system. Researchers have explored these distinct properties of molecular aggregates to enhance the effective chiral signature aiming for the demonstration of amplified chiral emission.[205,206] J-type chiral aggregates appear ideal in this case as they are known to show superradiance with narrow intense emission lines.[207–210]

However, a few issues need to be accounted for in this context when exploring the photophysical properties of J-aggregates. The low Stokes shift measured from such J-aggregates makes it difficult to extract any intrinsic chiral signatures from polarimetric measurements due to the reabsorption of the emitted light. This reabsorption leads to inner filtering artefacts (see Section 2.5.6) that eventually spoil the interpretation of the data.[211] Additionally, the huge anisotropy of aggregated samples adds artefacts to chiroptical

measurements if one forgets to properly account for the associated contributions of linear dichroism (LD) and linear birefringence (LB), as discussed in Section 2.1 in Chapter 2. These intrinsic properties of the material make it difficult to characterize the chiroptical signatures of J-aggregates.

In this chapter, we exploit the unique assets of Mueller polarimetry to extract the intrinsic chiroptical signatures of J-aggregates of C8O3 (3,3′-bis(3-carboxy-n-propyl)-3,3′-di-n-octyl-5,5′,6,6′-tetrachlorobenzimidacarbocyanine) (Figure 3.1.a) that forms highly anisotropic tubular and fiber-like structures. Apart from artefacts due to anisotropy, C8O3 adds more complexity to the characterization methods by forming both left- and right-handed aggregates due to spontaneous symmetry breaking with no control of enantioselectivity. This racemic nature of the self-assembly requires careful measurements when targeting selective characterization. Using home-made Mueller polarimetry, we eliminate various artefacts and show that these structures are efficient CPL emitters. In addition, we demonstrate that these structures display unique property of bisignate CPL signal with a high correlation of ground to excited state chirality.

3.2 C8O3 aggregates

The class of cyanine molecules is well-known to form J-aggregates with ordered molecular packing in linear as well as tubular structures with fascinating optical properties due to long-range excitonic interactions.[212–215] These J-aggregates were studied extensively in the past for their application in artificial light harvesting devices, spectral sensitizers in photographic industry, opto-electronics and nonlinear optics.[216–220] The influence of structural modifications of the cyanine dye 5,5′,6,6′-tetrachlorobenzimidacarbocyanine (TBC) in the morphology of aggregates was initially studied by the group of Dahne.[221,222] These amphiphilic dyes self-assemble through hydrophobic interactions, hydrogen bonding, dispersion forces between highly delocalized π-electron clouds, and electrostatic forces due to delocalized positive charges.[215,223] C8O3 aggregates are double-walled nanotubes with spectral signatures characteristic of J-aggregates similar to the well-studied C8S3 (3,3′-bis(2-sulfopropyl)-5,5′,6,6′-tetrachloro-1,1′-dioctylbenzimidacarbocyanine) aggregates with the herringbone-like molecular packing. However, C8O3 differs from C8S3 by showing strong CD signals. [209,224]

C8O3 aggregates were known to have mainly two mutually perpendicular electronic transitions, one polarized along the axis of the tube termed longitudinal exciton and the other polarized perpendicular to the axis termed the transverse exciton.[224–226] The monomers initially

form a small assembly in solution, which later aggregates into single tubular aggregates (Figure 3.1.b). These tubular aggregates undergo another nucleation stage to form twisted chiral bundles as shown in Figure 3.1.c.

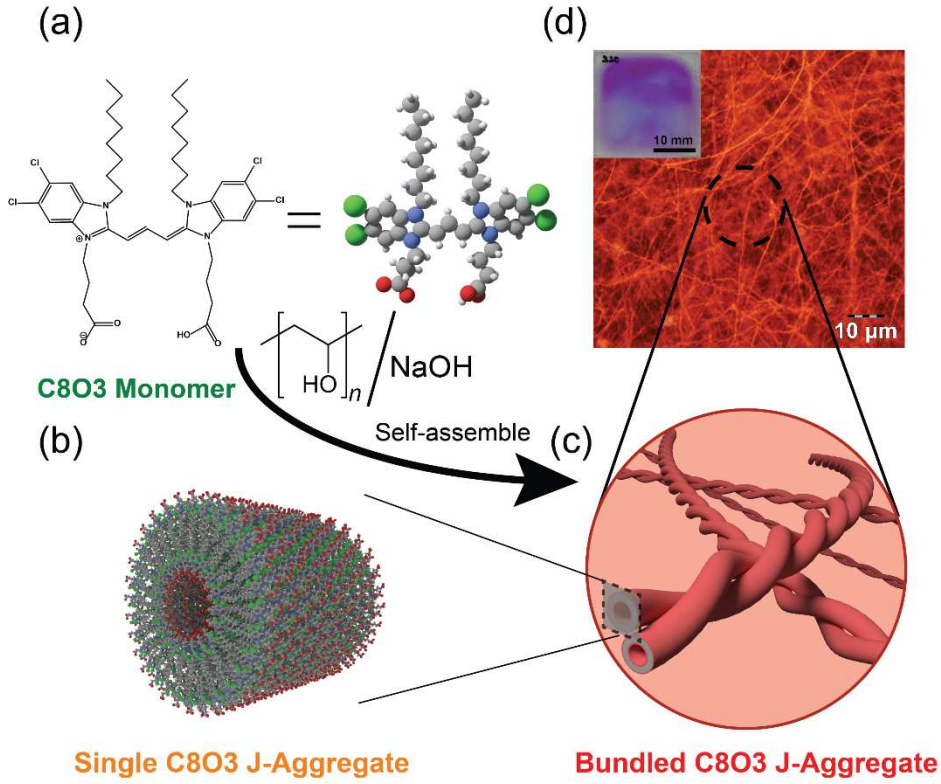

Figure 3.1: *Chemical structure of the amphiphilic C8O3 dye monomers (a) that self-assemble in chiral, double-layer tubular aggregates showed in (b) formed by adding PVA/NaOH into the monomer solution prepared with ethanol.[14] At a later stage of self-assembly, these tubular aggregates get intertwined into twisted bundles (c). These aggregate structures in the film state can directly be imaged using dark-field microscopy (see (d)). The inset in (d) shows a photograph of the thin film sample as it appears after preparation.*

Although, the molecules form aggregates with left- and right-handed geometry due to spontaneous symmetry breaking, a large CD signal can still be measured. This remarkable measurement indicate enantiomeric richness in the self-assembly. X-ray structure analysis of single crystals of C8O3 was reported in the literature that identified the presence of twist in the trimethine backbone with an angle of 18° for some of the molecules.[227] This structural distortion in C8O3 molecules is presented in Figure 3.2. It is, therefore, realized that this feasibility of dihedral torsions in the structure of the molecule might have initiated the formation of helical aggregates when the crystalline material with an enantiomeric form of the

dye is dissolved in the solution phase for aggregation. A similar chirality transfer has been proposed for crystals of sodium chlorate.[228]

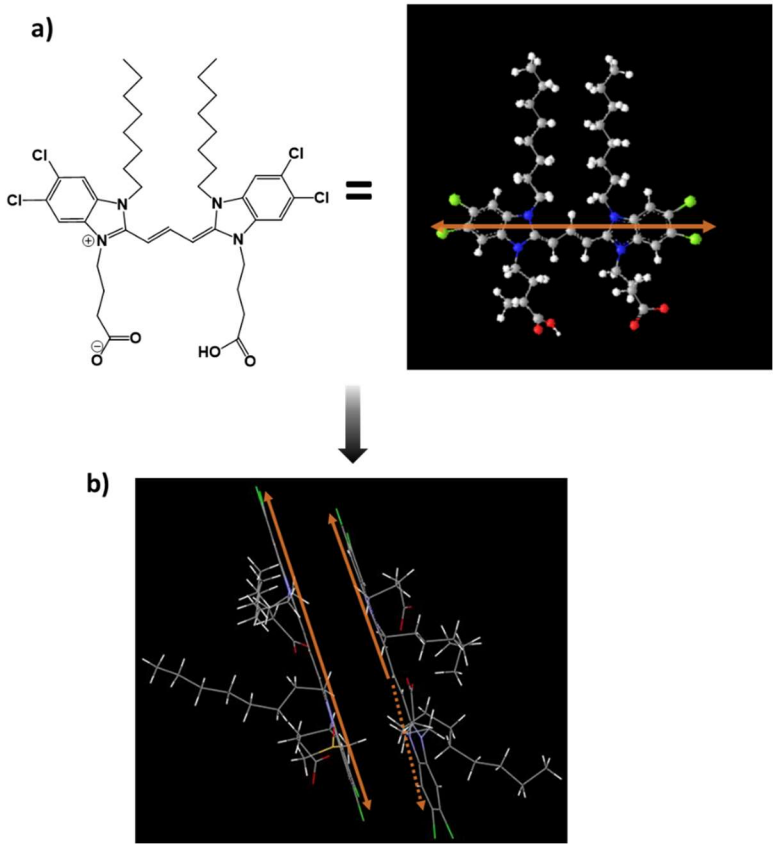

Figure 3.2: *a) Molecular structure of C8O3 with the representation of the transition dipole (orange double arrow) along the trimethine backbone. b) The molecular packing in single crystal showing twist in the trimethine chain. The solid double arrows shows the parallel arrangement units in the molecules, while the dotted line shows the twisted section in the chromophoric unit. Reproduced using crystallographic data (CCDC-14064) reported in ref*[227] *and reproduced using the software, Mercury 3.8.*

A huge linear anisotropic optical response in the ground state has been reported in the literature, but to our knowledge the excited state anisotropic features were not explored.[225] We could indeed expect a high linearly polarized emission from these structures due to their high anisotropy in the ground state. Therefore, artefacts in both ground and excited state chiroptical signals are highly probable in these structures. Hence, artefact-free polarimetric analysis is extremely important in characterizing their intrinsic properties. The ground state chiroptical spectral variations with varying aggregation phases in solution have previously been analysed in the laboratory using Mueller polarimetry.[229] Using a similar solution-phase analysis for the excited state chirality is however much more difficult. This difficulty stems mainly from the

fast diffusion of aggregates. As a consequence, polarimetric studies have to be performed in thin film conditions. In addition, the restricted diffusion of aggregates in thin film helps in focusing the light beam on a small region (limited by the numerical aperture of a microscope) with a specific distribution of aggregates. This "optical microscopy" based experimental strategy gives the possibility to study the microscopic polarimetric properties of these aggregates down to the levels of few structures.

3.3 Sample preparation and dark field microscopy

A 0.25 mM C8O3 (FEW Chemicals) monomer dye solution was prepared by dissolving in ethanol (Solution 1). PVA/NaOH solution was prepared by dissolving 6% PVA (Polyvinyl alcohol 40-88, 205 kDa from Sigma-Aldrich) and 10 mM NaOH (97% from Sigma-Aldrich) in a 1:1 volume ratio (Solution 2). Solution 2 was added to Solution 1 in a 1:1 volume ratio, thoroughly mixed (Solution 3), and then drop-casted on a well-cleaned glass substrate (inset in Figure 3.1.b). The substrates were left overnight (12-15 hours) for drying to get films of C8O3 aggregates.[225] This gave films that are 1-4 μm thick. These films are highly inhomogeneous with fibre-like aggregates as seen from the dark field microscopic image in Figure 3.1.d. This demands a method that can selectively measure properties from an almost homogeneous region in the film, motivating our development of Mueller polarimetry with the addition of microscopes.

3.4 Transmission Mueller polarimetry on C8O3 aggregates

The details of this experimental procedure for transmission Mueller matrix are described in (Sections 2.2 and 2.4 in Chapter 2). These experiments take around 30 min with an average of 3 Mueller measurements. A non-depolarizing matrix (see discussion in Section 2.4) obtained from the C8O3 aggregate film generated from the transmission Mueller matrix through differential decomposition is shown in Figure 3.3. [230,231] This decomposition method allows us to directly estimate the ground state polarimetric properties of the material. Here, the linear dichroism (LD) and linear birefringence (LB) are very high in comparison to the circular dichroism (CD) and circular birefringence (CB). In such a situation, it is highly probable to observe artefacts in CD if this signal is not corrected for the LD-LB components (see Section 2.1).

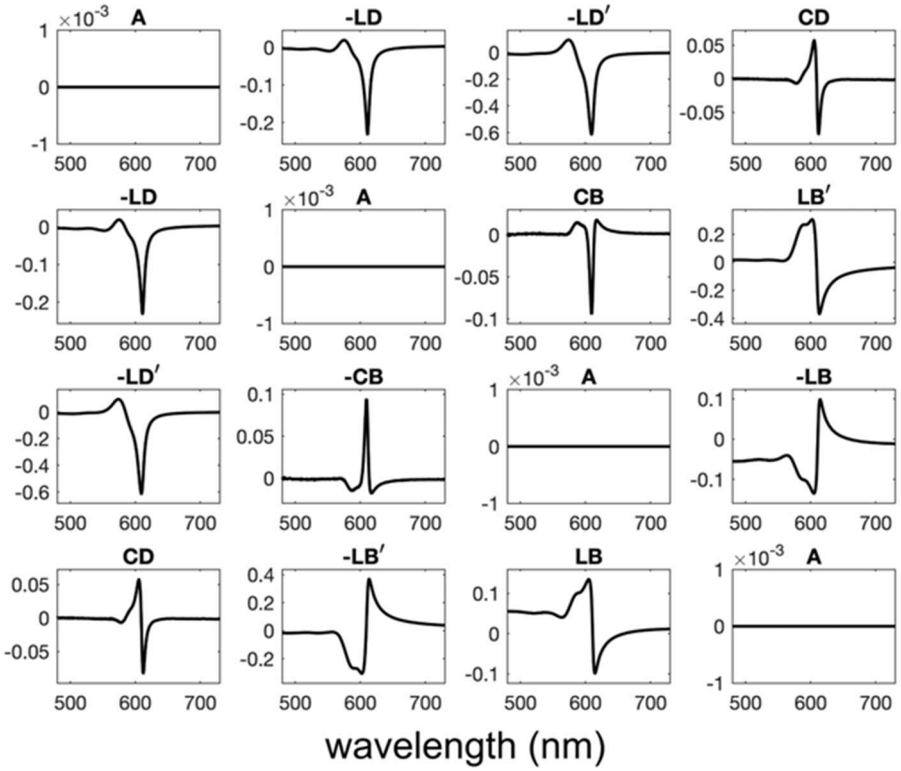

Figure 3.3: *The non-depolarizing matrix generated from the transmission Mueller matrix that presents different polarimetric observables in the ground state of the bundled aggregates.*

The absorption spectra of monomers, tubes, and bundles are shown in Figure 3.4. The monomers have their absorption maxima at 527 nm in ethanol, and the spectra undergo a red shift upon aggregation. This red shift is a signature of J-type molecular packing. The aggregates have mainly two absorption peaks characteristic of a longitudinal exciton at 610 nm and transverse exciton at 576 nm. When measuring the absorption spectra, we took great care to adjust the power of the white light source to prevent inducing spontaneous emission. The absorption spectra of tubular aggregates and bundled aggregates are hardly discernible in a small 2 nm blue shift for the bundles. This 2 nm shift is however instrumental in determining the interaction type between the tubes and bundles. This blue shift indeed indicates that the bundles are formed through an H-type interaction between the tubes (Section 1.5.3 in Chapter 1).[232]

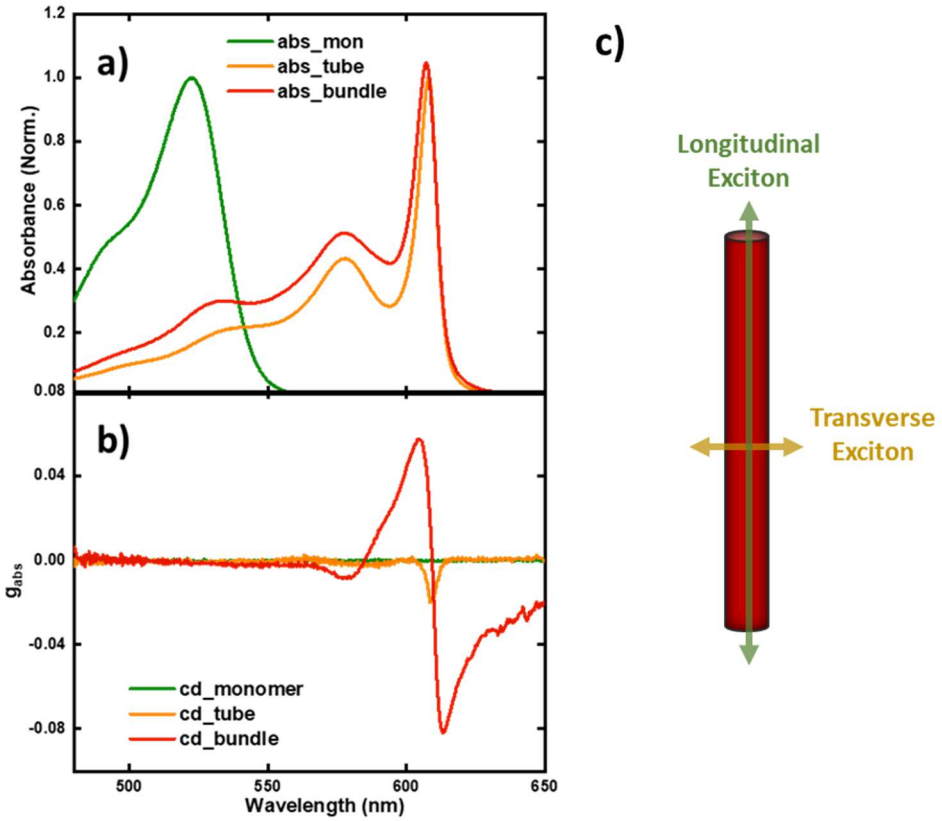

Figure 3.4: *Absorption spectra (a) and CD (absorption dissymmetry factor, g_{abs}) spectra (b) of C8O3 monomers in 0.3 mM solution in ethanol (green), tubular aggregates in film (orange) and bundled aggregates in film (red). The absorption peak at 610 nm corresponds to longitudinal exciton whereas the peak at 576 nm corresponds to the transverse exciton. (c) Schematic representation of the longitudinal and transverse excitons along the aggregated structure. The absorption peak for tubular and bundled aggregates at 527 nm might be originating from the residual monomers in the films. The bisignate CD spectrum of bundles shows cross-over at 610 nm at the absorption maximum of the aggregate, while that of the tubular aggregate is monosignate with a peak maxima at 610 nm.*

Focusing specifically on bundled aggregates, the LD and LD′ profiles (Figure 3.3) have two peaks, one centred at 610 nm corresponding to the longitudinal excitonic transition and another at 576 nm corresponding to the transverse exciton. The oppositely signed nature of the peaks identifies that the two transitions are oriented almost orthogonal to each other (this feature will be verified in Chapter 4). One essential spectral signature of our interest is the CD, that describes the ground state chirality of the material. This chiroptical signatures is presented in Figure 3.4.b in terms of absorption dissymmetry factor, g_{abs} (Section 1.6 of Chapter 1). The C8O3 monomers shows no CD signal in solution state (shown in green). However, the

molecules undergo self-assembly to form tubular structures that display a monosignate peak at the absorption maximum as seen in Figure 3.4.b (shown in orange). Further, the tubes undergo bundling to form twisted fibre-like structures that show a bisignate CD signal with crossover at the absorption maxima (shown in red). This distinct feature of bisignation in CD is a signature of exciton coupling and is originating from the coupling of longitudinal exciton of the tubes upon bundle formation. Here, we assume that the coupling of transverse exciton is much lower compared to longitudinal excitons to generate a large spectral variation. This assumption is taken based on the lower dipole strength for transverse exciton that reduces the coupling strength between the transverse excitons between the tubular aggregates. The bundles form either left-handed or right-handed structures. Here, resorting to microscopic objectives serves as an essential tool that allows to selectively measure local regions over which an enantiomeric excess can be isolated from the extended surface of the sample that macroscopically corresponds to a racemic mixture.

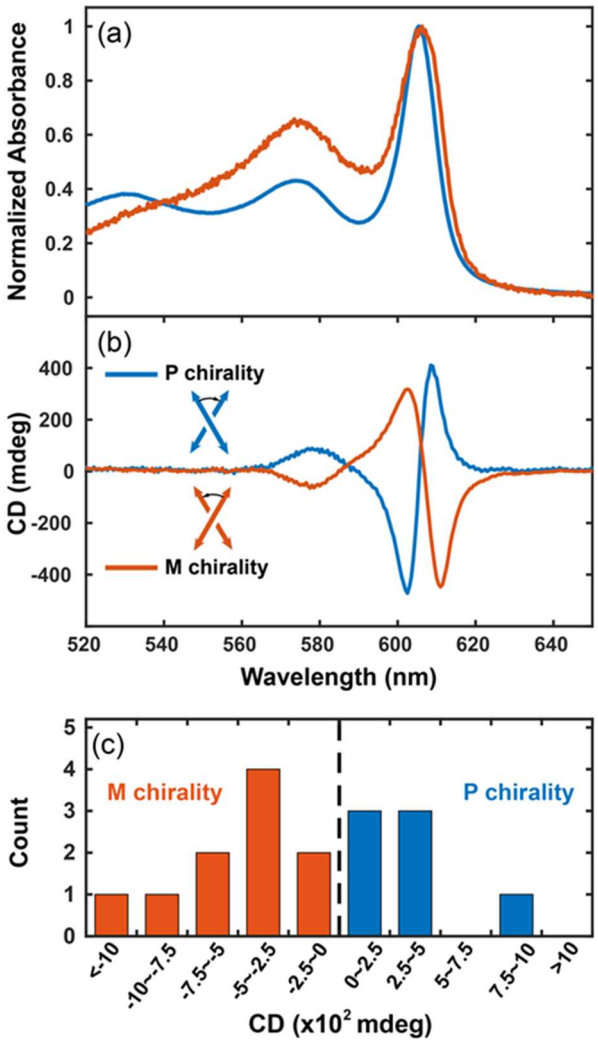

Figure 3.5: *(a) Absorption spectra of P- and M-chiral bundles self-assembled C8O3 aggregates in thin film, and their respective CD spectra (b) measured using Mueller polarimetry. Note that the crossover points of bisignate CD are both positioned at the absorption maxima of each form. (c) Statistical distribution of P- and M-forms through the film, revealing no particular bias, thereby characterizing the racemic nature of the film.*

We have also verified the stochastic distribution of P- vs M- chirality by monitoring the sign of CD signal at various locations on the same sample film and also among different samples (Figure 3.5). The statistical study performed on 17 positions resulted in 10 measurements associated with the M-chirality and 7 measurements associated with the P-chirality of the bundle. This nearly similar statistical distribution suggests a racemic ensemble of bundles within the films, with no preference for one enantiomer over the other.

3.5 Emission Mueller polarimetry on C8O3 aggregates

In this section, we investigate the excited state chiroptical properties of tubular and bundled C8O3 aggregates in film state. We also explain the correction methodologies employed for extracting the intrinsic polarimetric properties and their importance in studying the excited state chiroptical signatures.

3.5.1 Correction for re-absorption of emitted light

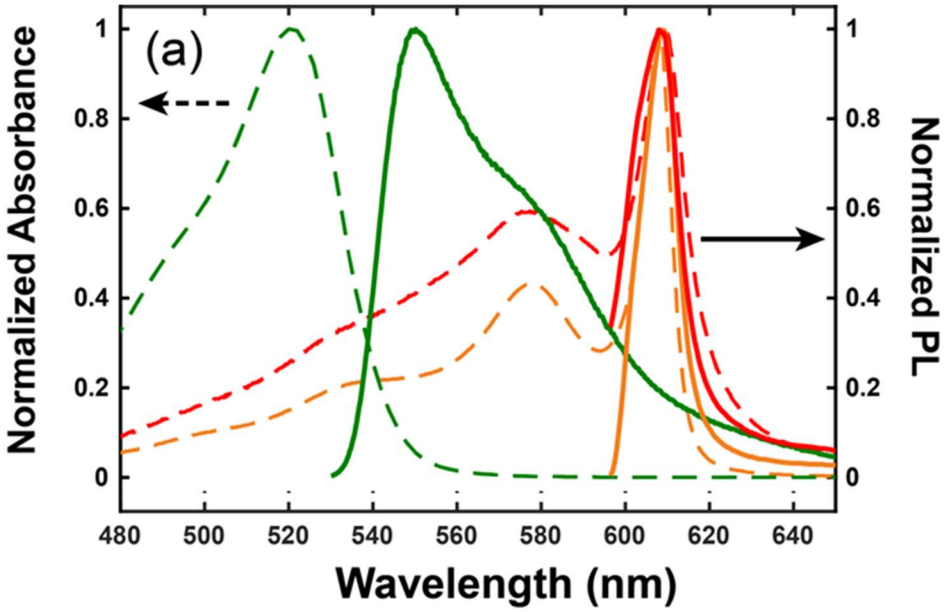

Figure 3.6: *Absorption (dotted lines) and emission (solid lines) spectra of monomers (green), tubular aggregates (orange) and bundled aggregates (red). The absorption and emission spectra of tubular and bundled aggregates are overlapping with each other, indicating the importance of performing the re-absorption correction. The emission spectra are taken by exciting at 576 nm.*

The emission spectrum of the C8O3 monomer in Figure 3.6 has its maximum at 543 nm while that of the aggregate is red-shifted in comparison to monomer, and centred at 610 nm. Here again, distinguishing bundles and single tubular aggregates from the emission spectra are extremely challenging.

From Figure 3.6, we also see that the emission spectra of the tubular and bundled aggregates are overlapping with their corresponding absorption spectra with zero Stokes shift. Here, we stress that for these J-aggregates with overlapping absorption and emission bands, the inner filtering artefact, if not well accounted for, is a strong artifact that can drastically

modify the strength of the CPL signal, which could be perceived as either a very low or an exceptionally high signal. Indeed, the CPL signal can also be modified by a filtering effect when the emitted light passes through the linear dichroic, linear birefringent, and circular dichroic optical medium. In such a case, we apply the correction methodology using transmission Mueller matrix to extract the intrinsic polarimetric properties, as discussed earlier in Sections 2.5.5 and 2.5.6 of Chapter 2. However, applying this method requires less diffusion of molecular species and a small path length (see Section 2.6 of Chapter 2). Therefore, stabilizing the aggregates in film becomes a crucial strategy in this case to well account for the issues of re-absorption.

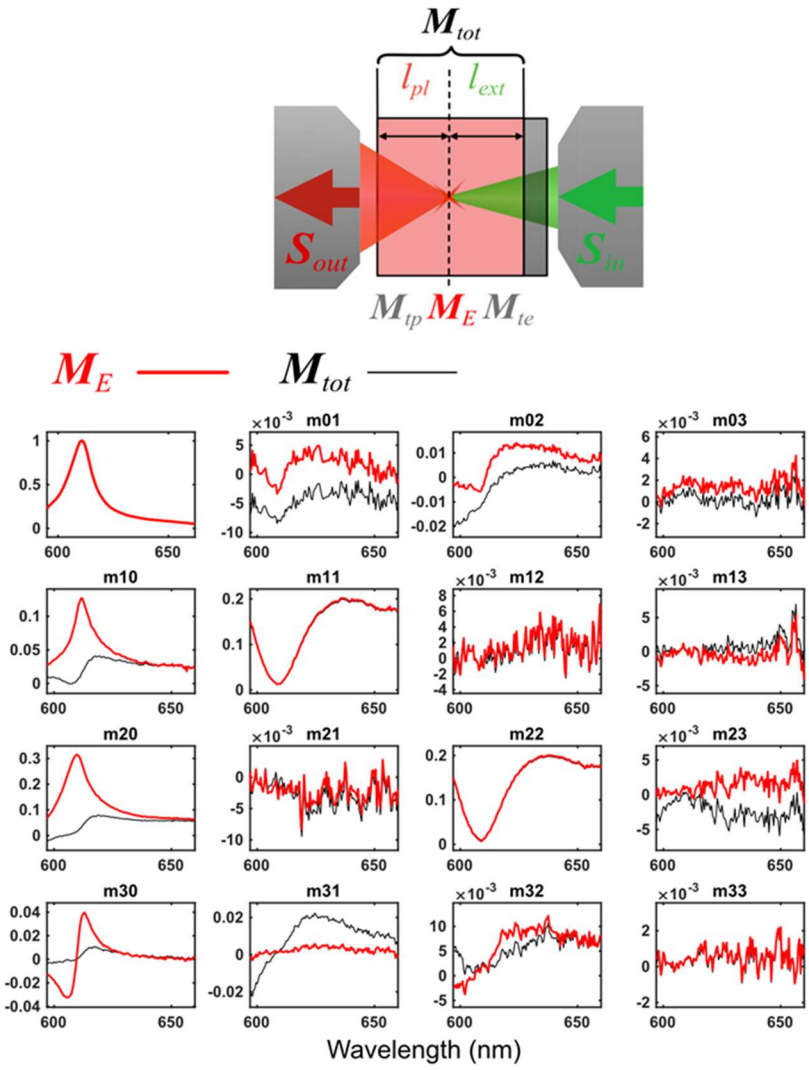

Figure 3.7: *The top panel shows the configuration of an emission Mueller matrix measurement and describes the sequence important to follow in order to correct for the induced inner filter effect. Here, l_{ext} and l_{pl} corresponds to the path lengths for the excitation and emission light, respectively. M_{tp} and M_{te} represents the Mueller matrices of transmitted emission and*

transmitted excitation light, respectively. S_{in} and S_{out} represent the input and output Stokes vector. The bottom panel shows the emission Mueller matrix before (M_{tot}, black trace) and after (M_E, red trace) correction for bundled aggregate excited at 530 nm.

Figure 3.7 shows the emission Mueller matrix of the bundle before and after applying the correction for re-absorption, generated by exciting the sample at 530 nm. The detailed description of this correction methodology is explained in Section 2.5.6 of Chapter 2. In this chapter, we mainly focus on the spectral signatures in the Mueller matrix coefficients of m_{10}, m_{20}, and m_{30}. The significance of other Mueller matrix elements will be discussed in Chapter 4. The elements m_{10} and m_{20} are the linearly polarized luminescence (LPL), while m_{30} is the CPL signal in terms of absorption dissymmetry factor, g_{lum} (Section 1.6 of Chapter 1). Here we can see that the black trace, corresponding to the signal before transmission correction, is bimodal in LPL identifying strong re-absorption of emitted light. In addition, the CPL signal is very low. On the other hand, once the correction methodology is applied, we regain the unimodal shape of the LPL spectra in m_{10} and m_{20} alongside an increased magnitude for the CPL signal. This CPL signal is surprisingly bisignate, similar to the CD spectra with a remarkably high value for g_{lum} close to 0.08. This result clearly shows the importance of performing a transmission correction to obtain intrinsic polarimetric signatures from a system that shows high re-absorption. Without applying this correction methodology, the strong CPL signature with its unique feature of bisignation would have not been discovered.

3.5.2 Spectral analysis of the CPL signal

As seen in Figure 3.8, the monomers show no CPL signal. On the contrary, the tubular and bundled aggregates show interesting chiroptical features in their excited states. In particular, the CPL signal obtained for tubular aggregate is monosignate at the maximum of the emission spectrum, whereas, the bundled aggregate with a bisignate profile has its crossover at the emission maxima of the aggregate. This spectral signature requires more analysis since a bisignate CPL signal is an exception for molecular systems as discussed in Section 1.5.3 of Chapter 1. A similar bisignate nature for CPL was previously observed for chiral polymers.[233] However, the sharp CPL signal measured here within a small spectral width for the emission spectra (full width at half maxima (FWHM) ~11 nm) is clearly a surprising outcome of our experiments. Analysis of these remarkable chiroptical properties of the aggregates will be performed in the following Sections.

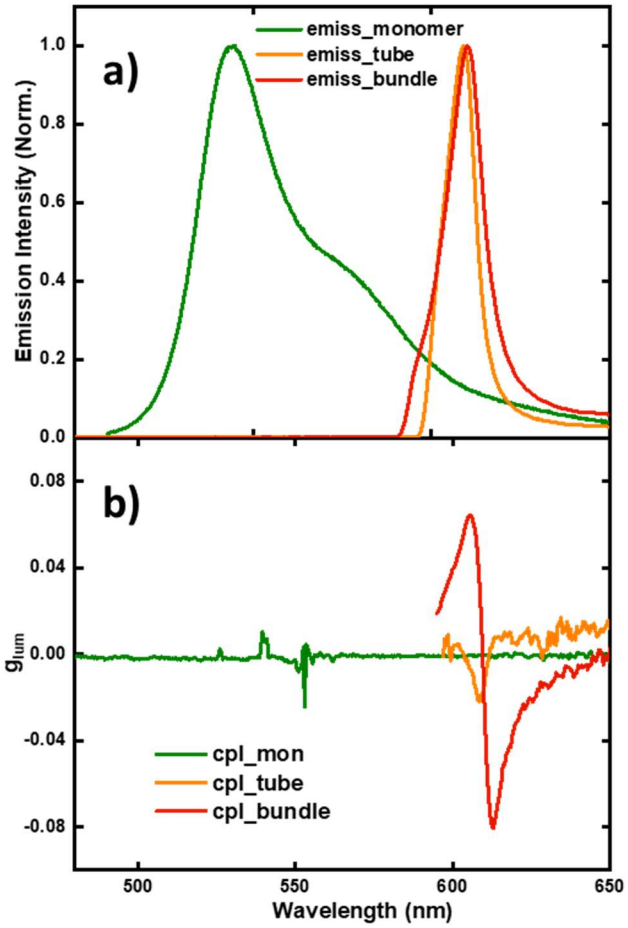

Figure 3.8: *a) Emission and b) CPL (luminescence dissymmetry factor, g_{lum}) spectra of monomer (green), tubular aggregate (orange), and bundled aggregate (red) excited at 532 nm. The emission spectra of monomer has maximum at 543 nm. The tubular and bundled aggregates have their emission maxima around 610 nm overlapping with each other (emission peak of longitudinal exciton). The monomers show no CPL signal. In contrast, the tubular aggregate shows a monosignate CPL signal at the emission maxima, while the bundled aggregate shows a bisignate profile with a crossover at the emission maxima.*

3.6 Chiroptical analysis

The bisignate nature of the CPL spectra is remarkable as it indicates two emission bands spectrally resolved due to their opposite helicity, whereas commonly we observe a single emission band based on Kasha's rule.[234] This rule, validated by numerous molecular systems, states that in any condensed phase, emission occurs in appreciable yield only from the lowest excited state of a given multiplicity, irrespective of the initial photoexcited state.[104] Herein, the two polarized emission bands have a crossover at the emission maximum similar to the CD signal, identifying the origin of this spectral signature as the result of exciton coupling of

longitudinal transition. We have then performed a circularly polarized luminescence excitation (CPLE) spectrum shown in Figure 3.9.b by exciting the sample from 510 nm to 580 nm with a step size of 8 nm in the excitation wavelength. The emission spectra with excitation wavelength from 510 to 580 nm presented in Figure 3.8.a increases in intensity in agreement with the increase in absorbance of the aggregated sample. In contrast, the CPL signal maintains a similar bisignate nature with maxima at 605 nm and minima at 613 nm (Figure 3.9.c). This CPLE spectrum demonstrates that the system radiatively relaxes from two electronic excited states of the bundles that remains unchanged regardless of the excitation wavelength. In this sense, the emission process seems to deviate from the usual Kasha's rule (see discussion on CPL in Section 1.5.3 of Chapter 1), as we further discuss below in Section 3.8. Note that anti-Kasha emission processes have previously been observed at the level of chiral polymers.[233]

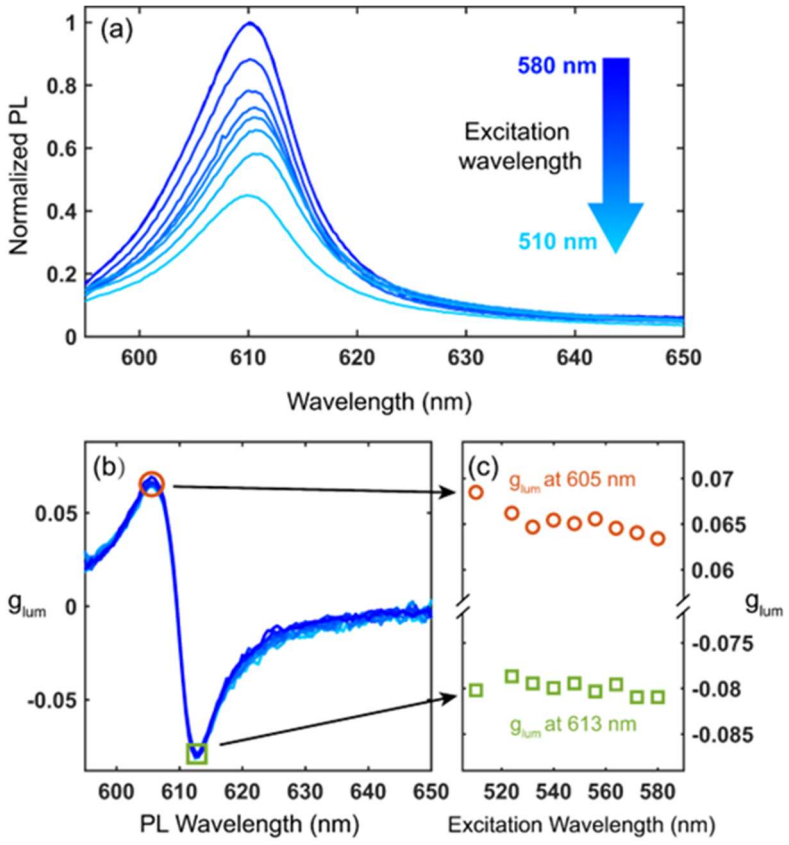

Figure 3.9: *(a) Normalized photoluminescence (PL) and (b) g_{lum} spectra of C8O3 bundles excited with wavelengths ranging from 580 nm to 510 nm. (510 nm, 524 nm, 532 nm, 540 nm, 548 nm, 556 nm, 564 nm, 572 nm, 580 nm). The inset in (a) details where the excitation wavelengths (all within the blue area) sit in the absorption and CD spectra. (c) The CPL excitation (CPLE) spectra is built by monitoring the evolution of the g_{lum} extremum values (at 605 nm and 613 nm) of the bisignate CPL throughout the excitation bandwidth.*

3.7 Correlation of ground and excited state chirality

The exceptional features of bisignate CD and CPL spectra intrigued us in correlating the ground and the excited state chirality of the bundled aggregates. The dissymmetry factors for absorption (g_{abs}) and emission (g_{lum}) evaluate the strength of the chiral signal, and their correlation indicates the extent of chirality preservation from the ground to the excited states.[235] Detailed analysis on the g_{abs}-g_{lum} correlations has been reported on simple chiral molecules from which it was understood that the correlation of absolute dissymmetry in emission and absorption is very low in many systems.[235] The low correlation in the dissymmetry factor originates due to conformational flexibilities and vibrational relaxations, resulting in emission from states different from those involved in the absorption process, eventually displaying different chiroptical signatures in the ground and excited states. As a consequence, this correlation is expected to enhance, if the molecular system is characterized by small Stokes shift where the states involved in the absorption and emission processes are the same.

The C8O3 aggregates studied in this thesis fall directly in this exceptional regime with zero Stokes shift in emission. But, this correlation in C8O3 aggregates can only be effectively studied, if the method employed is artifact-free in order to precisely capture the intrinsic chiral signals emerging from the aggregates. By implementing our methodology of the transmission correction (discussed in Section 3.5.2 above), we were able to extract the intrinsic chiroptical properties that eventually enabled us to perform precise correlation studies of the ground and excited states.

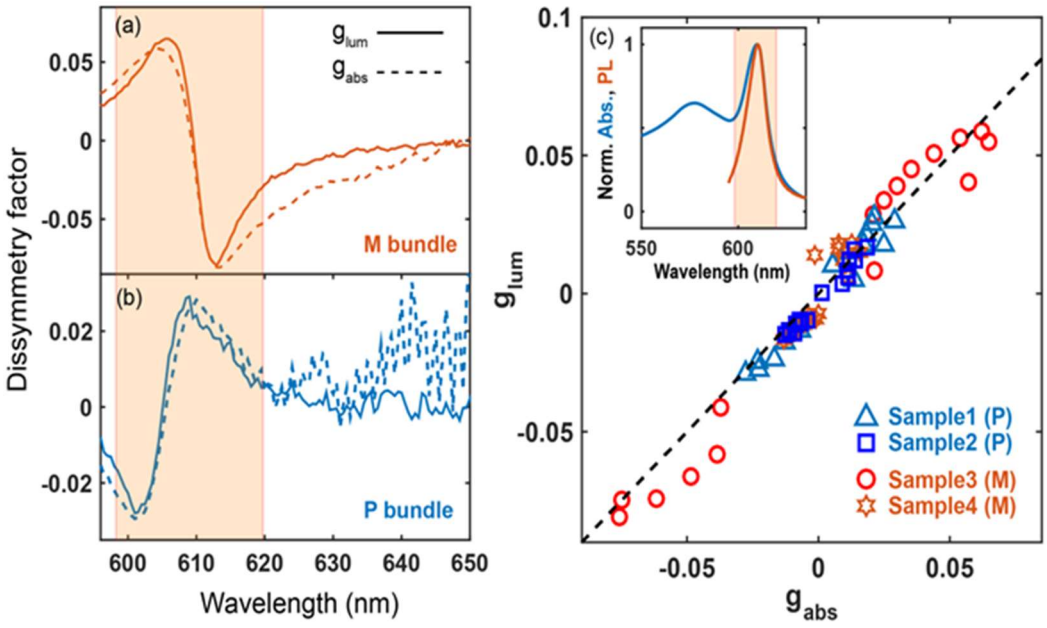

Figure 3.10: *Absorption and emission dissymmetry factors g_{abs} and g_{lum} for bundles of (a) P- and (b) M-forms of chirality. (c) The correlation plot of g_{abs} and g_{lum} for different samples in M- and P-forms, gathering data from 4 different samples and bisignate profiles of different amplitudes. Data points are taken for each sample at different wavelength within the overlapping wavelength range for absorption and emission spectra (orange area). The dash line with a slope 1 shows the quasi-perfect correlation.*

The correlation curve is presented in Figure 3.10.c, by analyzing the g_{abs} and g_{lum} plots in Figures 3.10.a and 3.10.b. This correlation study is performed by picking values within the overlapping wavelength range of the absorption and emission spectra (region marked in orange color in Figure 3.10.c). The values are collected from 4 different samples of both P and M bundles. Once plotted, these values are distributed linearly along a line of slope 1 going through the origin, thus, presenting a nearly perfect correlation of the ground and the excited state chirality (Figure 3.10.c).

In general, for many chiral organic molecules, one measures $g_{lum} < g_{abs}$.[235] In our case, the high correlation must have derived from the near-zero Stokes shift found in bundles, implying that the transitions engaged in the absorption and emission process are the same.[236] This, in turn, forces the g_{abs} and g_{lum} to be equal as the g-factor is expressed as, $g = 4R/D$, where the rotational strength (R) and the total dipolar strength (D) are associated with the ground-to-excited ($|g\rangle \rightarrow |e\rangle$) or excited-to-ground ($|e\rangle \rightarrow |g\rangle$) state transition, respectively (see Section 1.6 of Chapter 1). Therefore, the tightly bound bundles with reduced degrees of freedom resulted in this quasi-perfect correlation.

3.8 Energy level diagram and bisignate CPL signal

The unique chiroptical signals characterized in the previous Sections can easily be synthesized with the exciton model commonly employed for studying the chiroptical properties of monomeric assemblies, but extending the description to bundled C8O3 aggregates. Herein, for explaining the chiroptical signatures of bundles, we consider strong dipolar coupling between the excitons of single tubular aggregates. This extension to the simple exciton model will help us in analyzing the structure-to-property relation in bundles. The CD and CPL spectra display bisignation around 610 nm where the longitudinal exciton absorbs. Hence, in this analysis, we consider only the interaction of longitudinal excitons of the tubes intertwined when forming the bundle. We remind that the simple exciton model is defined assuming that only degenerate transition dipoles are interacting. Accordingly, here we neglect any interaction between the longitudinal and the transverse excitons. This assumption could be validated considering that the two dipoles are oriented almost orthogonal to each other, implying destructive longitudinal-transverse exciton coupling.

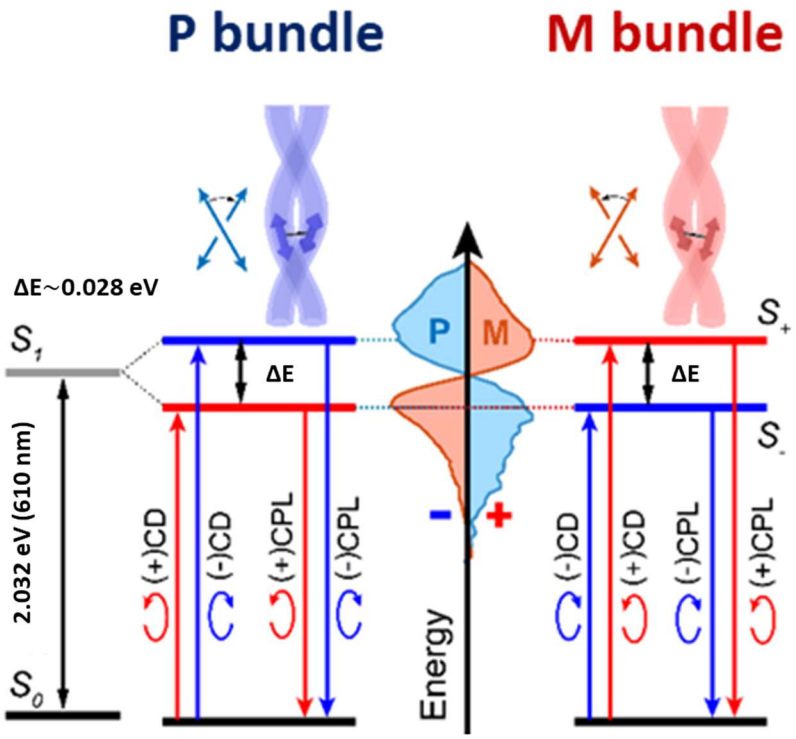

Figure 3.11: *Energy level diagram of P- and M-type bundled aggregate built from the CD, CPL and CPLE measurements. The Frenkel exciton strong coupling yields a Davydov splitting of 28 meV for both forms.*

Focusing on the longitudinal excitons, we thus adopt the simple exciton model considering the strong coupling of chiral Frenkel excitons longitudinally excited along the tubular aggregates, that are obliquely coupled inside the twisted bundles (as sketched in Figure 3.2). Under strong coupling, two new states are formed with the Frenkel excitons coupled in-phase and out-of-phase, where we represent the former as S_+ and the latter as S_- states, respectively.[232,237] As detailed in Section 1.5.3 of Chapter 1, the two newly formed states in an obliquely coupled configuration, display opposite chiral signatures. This difference in chirality for the two excited states results in the bisignate nature of CD and CPL spectra. In addition, the left and the right-handed bundles show mirror imaged CD and CPL spectra as described in detail in Section 1.5.3. This opposite chiral signatures of CD and CPL for left- and right-handed bundled aggregates can be seen from Figures 3.10.a, 3.10.b.

With this description based on the exciton model, we draw the energy level diagram of the bundled aggregate in Figure 3.11. Here, S_0 and S_1 are the ground and the excited electronic states of the single tube, that are separated with an energy difference of 2.036 eV (610 nm). The two newly formed states are separated with a very small energy gap of 28 meV, which is proportional to the inter-exciton coupling strength. With this small Davydov splitting, the two $S_\pm$ states are indiscernible looking at either the absorption or emission spectra. Remarkably, only a chiroptical characterization is capable of resolving the two exciton coupled states. This capacity is rooted in the fact that two states involve opposite helicities. By taking into consideration the small blue shift observed in the absorption spectrum of the bundle in comparison to that of the tubular aggregates, we consider that the dipolar coupling is of H-type. This sets the S_- state lower in energy than the S_+ state. According to the experimental results on CD, upon excitation, the transition occurs from the ground state to the two electronic excited states. When the sample is excited to a higher energy level, we observe emission from both the electronic excited states. Therefore, the P-type bundle has a positive followed by a negative couplet in CD and CPL, while these spectra reverses for the M-type aggregate (similar to description in Figure 1.10 of Chapter 1). Hence, the emission occurring from both the electronic excited states, describes well the bisignate profile of the CD and CPL spectra with high g_{abs}-g_{lum} correlation from the bundled C8O3 aggregates.

One remarkable feature of this energy level diagram is that the emission proceeds from the two electronic excited states, and not preferentially from S_- only. This looks very similar to an anti-Kasha relaxation dynamics, when emission is triggered from an excited state higher in energy compared to the lowest excited state. The CPLE spectra and the g_{abs}-g_{lum} correlation

study performed above clearly show that the chiral absorption and emission occur between the ground and the two electronic excited states. This remarkable spectral feature could be the result of high suppression of vibration relaxation from the S_+ state to the S_- state due to the quenching of the vibrational manifold through the dense π- π stacking of monomeric units in the aggregate. However, considering that the 28 meV Davydov splitting is just of the order of the thermal energy available at room temperature ($k_BT = 25\ meV$), the S_+ state can also be considerably populated directly from S_- state through thermal excitation. Therefore, both these populated excited states (S_+ and S_-) can lead to emission lines with opposite helicities, giving rise to a bisignate CPL signal.

To verify if the emissive feature originates due to structural rigidity or thermal excitation, temperature-dependent emission polarimetric studies have to be performed. We expect that if the bisignation in the CPL signal originates from thermal excitation, reducing the temperature of the system would display a change from a bisignate to a monosignate profile. However, the bisignate nature of the signal would be retained if it takes its origin from the high structural rigidity of the aggregate. Performing emission measurements at different temperatures lower than 25°C (room temperature), and monitoring the evolution of the CPL signal will, therefore, help in distinguishing the precise origin of the bisignation in CPL.

3.9 Conclusions

In this chapter, we have investigated the ground and excited state chiroptical properties of bundles of C8O3 aggregates in thin films using Mueller polarimetry. Although these aggregates form chiral twisted structures, they were not previously identified as potential CPL emitters, and neither their excited state polarimetric properties were characterized. The zero-Stokes shift IN emission makes it hard indeed to characterize the excited state features due to inner filtering artefacts, that can easily pollute the chiroptical signatures. Herein, by employing Mueller polarimetry, we removed various potential artefacts from the measurements to extract the intrinsic chiral properties of the C8O3 aggregates. Once our methodology was set up, we identified C8O3 bundles as an excellent CPL emitter with g_{lum} close to 0.08. We also identified bisignation in both CD and CPL, originating from the strong coupling of chiral longitudinal Frenkel excitons in each tubular aggregate when forming the bundles.

Moreover, the ground and the excited states showed nearly a 100% one-to-one correlation with overlapping g_{abs}-g_{lum} curves near the longitudinal absorption cross-section.

This close-to-perfect correlation points towards high chirality preservation from ground-to-excited states. Furthermore, the bisignate profile of the CPL signal identifies multiple electronic emissive features, which might have emerged due to low energy gap (with a splitting in energy of 28 meV) between the two electronic excited states formed by strong coupling. This energy gap, very close to thermal energy, $k_B T = 25\ meV$, at room temperature that could have favored thermal excitation paths of the higher electronic excited state.

The unique chiroptical signatures of C8O3 twisted bundles turn them into promising materials for chiroptical application especially considering their high luminescence dissymmetry factor. Their capacity to yield opposite chiral emissions with high contrast and narrow bandwidth opens applicative perspectives in the context of chiral photonic architectures. Besides these perspectives, our experimental results involved efficient tools and methods that can remove artefacts due to re-absorption and high anisotropy. These procedures demonstrated in this Chapter led us to extract the intrinsic polarimetric properties of the material that would have been otherwise hardly accessible using conventional optical methodologies.

Chapter 4

2D Excitation-Emission Mueller polarimetry: ground and excited state anisotropy characterization of C8O3 aggregates

In this Chapter, we explore the excitation-wavelength dependent excited state polarization properties of the C8O3 aggregates in film state using 2-dimensional Excitation-Emission Mueller polarimetry. Anisotropy characterisation of these structures are highly challenging due to the high inhomogeneity of the sample and the zero-Stokes shift in emission. Employing the Mueller formalism, we separate the anisotropy due to spatial orientation of structures and the anisotropy between the excitation and emission dipole orientation. This artefact-free analysis helps in determining the excitation and emission dipole orientation and their orientational order in the film state of C8O3 aggregates. Furthermore, with this method we analyse the wavelength-dependent evolution of other ground and excited state polarimetric properties such as fluorescence detected linear dichroism, fluorescence detected circular dichroism, linearly polarized luminescence and circularly polarized luminescence.

4.1 Introduction

Polarimetry, employing the polarization property of light, has served as a vital tool for the characterization of the optical properties of materials as discussed briefly in Chapter 1.[238–242] Fluorescence anisotropy or fluorescence polarization measurement provides essential information on the size, shape and rigidity of the molecular system. In addition, it also gives insights on the transition dipole orientations of excitation and emission.[243,244] These measurements have been used in biological systems for studying the protein interactions, membrane fluidity and immune-assays.[245–250] Fluorescence anisotropy measurement is based on the principle of photoselection, which is the preferential excitation of fluorophores with transition dipoles oriented parallel to the polarization of the excitation light source. In an ideal scenario, this preferential excitation results in preferentially polarized fluorescence. However, the diffusion of fluorophores, and the depolarization and re-absorption of emitted light affects the anisotropy measurement impeding proper analysis.[251] Hence anisotropy measurements are limited to mostly small molecules heavily diluted and dissolved in highly viscous solvents such as glycerol or propylene glycol which effectively reduces rotational diffusion. Employing these protocols developed for such system are difficult for characterizing longer aggregates in solution due to their extreme sensitivity to the solvent environment.

From Chapter 3, we see that the C8O3 aggregates with long fibre-like nature, shows huge anisotropic signatures in absorption and emission with large linear dichroism (LD) and linearly polarized luminescence (LPL) signals. These anisotropies originate from the excitonic characteristics and structural orientations of the molecular system in the film, which vary in magnitude depending on the orientation order (vanish if randomly oriented) of the sample. Herein, for convenience, we call these anisotropy parameters as "extrinsic" as they depend on the distribution of the structures in the sample. Also, we call the fluorescence anisotropy or fluorescence polarization as intrinsic, because the relative orientation of absorption and emission dipoles is an "intrinsic" property of the molecular system.

In Chapter 3, we explained the optical complexity of C8O3 aggregates where simultaneously occurring polarization features (for instance, linear dichroism (LD) and linear birefringence (LB)) obscure the interpretation of other unique polarization signatures.[252] Although, having the aggregate structures in film state reduces the issue of rotational diffusion for measurements in conventional methods, the zero-Stokes shift in emission and the inhomogeneity of the film make it challenging to measure the intrinsic anisotropies.

Additionally, due to the high anisotropic nature these extrinsic signatures couple with the intrinsic features making the fluorescence anisotropy measurement difficult. Here again, Mueller polarimetry serves an essential role in characterizing the artefact-free anisotropy of complex molecular structures.[253–255] Recently, this polarimetric method has been employed to probe the orientation of achiral dye TB-NDI on the surface of supramolecular nanotubes formed by chiral dipeptide motif, showing the necessity to perform Mueller formalism for the understanding of structural complexity.[243] Therefore, in this Chapter, we explore in detail the ground and excited state anisotropic properties of bundled C8O3 aggregates using Mueller polarimetry.

In the previous Chapter, we have characterized the excited state properties of the sample by exciting the system at a single wavelength focusing mainly on the chiroptical signatures. However, the emission property of a material, especially a supramolecular aggregate with intricate energy level characteristics, demands an excitation spectrum. This brings out the necessity to perform excitation spectroscopy coupled with Mueller formalism. Similar method has previously been applied for C8O3 aggregates in solution, however, did not yield spectral profiles easy to decipher due to diffusion of aggregates causing depolarization of the optical signals. Therefore, efficient experimental strategy demands measurements to be performed in rigid (viscous) conditions.[256]

In this Chapter, we perform fluorescence Mueller polarimetric measurements coupled with excitation spectroscopy on chiral bundled C8O3 aggregates in polymeric film to generate a 2-dimensional excitation-emission (2D-Ex-Em) Mueller matrix. This characterization methodology provides information on the excitation wavelength-dependent excited state polarimetric properties of the material such as fluorescence-detected linear dichroism (FDLD), fluorescence-detected circular dichroism (FDCD), linearly polarized luminescence (LPL), circularly polarized luminescence (CPL) and the fluorescence polarization of excitation and emission dipoles. This artifact-free information is hardly accessible with conventional spectroscopic methods, while easily accessible with the Mueller measurements.

4.2 Mueller matrix in emission

In this Section, we describe the different intrinsic and extrinsic anisotropy observables obtained from Mueller matrix based on the literature reports in ref.[244,257] This includes estimating the anisotropy in ground state such as FDLD, FDLD′ and FDCD, and the excited

state anisotropies such as LPL, LPL′ and CPL (see Section 2.11 of Chapter 2). Furthermore, we also describe on how to extract the intrinsic fluorescence anisotropy and other phase information from the Mueller matrix.

4.2.1 Estimating anisotropy

Traditionally, fluorescence anisotropy is measured with the help of two polarizers, one fixed before the sample placed vertically along the z-axis, and the other placed after the sample either vertically (z-axis) or horizontally (x-axis) as shown in Figure 4.1. In this configuration, the fluorescence anisotropy parameter, *r* and the polarization, *p* are defined as,

$$r = \frac{I_{\parallel} - I_{\perp}}{I_{\parallel} + 2I_{\perp}} \; and \; p = \frac{I_{\parallel} - I_{\perp}}{I_{\parallel} + I_{\perp}} \tag{4.1}$$

where, $I_{\parallel}$ and $I_{\perp}$ are the intensities associated with vertical and horizontal detection of the polarization when the incident light is vertically polarized. Fluorescence polarization and anisotropy carry similar information, however the term anisotropy is more commonly used since the quantity is normalized by total intensity in all the angles ($I_z = I_{\parallel}$, $I_x = I_y = I_{\perp}$).[251,258,259]

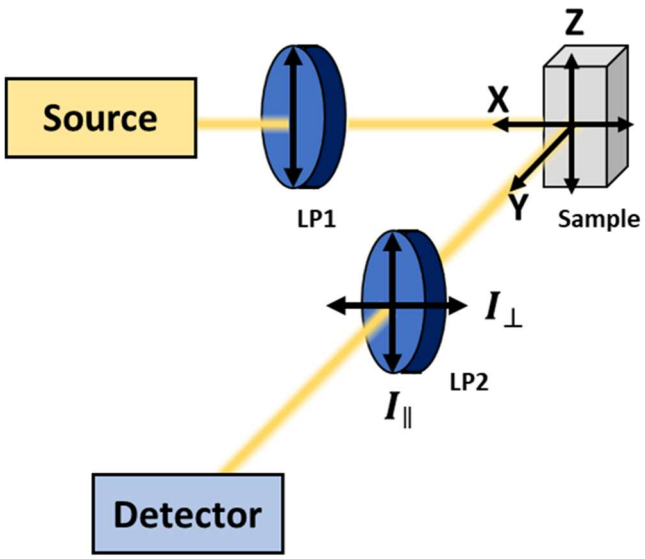

Figure 4.1: *Experimental setup for a traditional anisotropy measurement. The linear polarizer LP1 is fixed and LP2 is rotated to measure the fluorescence anisotropy of a sample.*

As opposed to traditional fluorescence anisotropy measurement, Mueller matrix allows us to extract the intrinsic and extrinsic anisotropy factors. To understand this, the emission Mueller matrix can be expressed as,

$$M = M_1 \times M_d \times M_0 \quad (4.2)$$

where, M_1 and M_0 represent the anisotropies intrinsic to the excited and ground states, respectively. M_0 describes anisotropic absorption of the incident beam by measuring the differential interaction of the ground state with the orthogonal polarization of the incident light (V/H, +45/-45, σ^+/σ^- based on the representation of Stokes vectors). This information reside in the 1st row of the Mueller matrix, that displays FDLD, FDLD′, FDCD. On the other hand, M_1 describes the anisotropic emission with regards to the orthogonal polarization of emission (V/H, +45/-45, σ^+/σ^-). This information resides in the 1st column of the Mueller matrix, that gives the excited state properties, characterizing the linear (LPL, LPL′) and circular polarization anisotropy (CPL) in emission. In addition, the information related to depolarization of optical signals caused by fast rotation of molecular species, energy transfer and random orientation of fluorophores, reside in the matrix, M_d, and can be identified from the diagonal elements of the Mueller matrix (Figure 2.11 of Chapter 2).[244] This Mueller matrix acts as a transfer matrix describing the changes in the relative orientation between the excitation and emission dipoles.

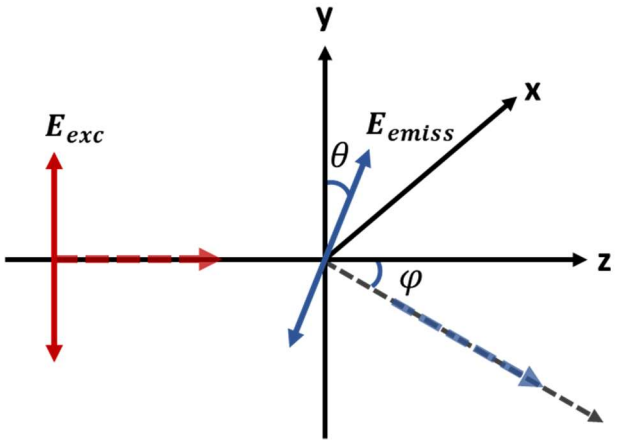

Figure 4.2: *Schematics of fluorescence scattering showing different angular parameters used in defining the matrix, M_d in Section 4.2.1. The solid red and blue arrows represent oscillating electric fields and the respective broken arrows represent its propagation direction.*

Using the dipolar approximation, and looking at the fluorophore molecules as randomly oriented dipoles with depolarization acting as the main polarimetric contribution, the polarization transfer matrix can be expressed as,

$$M_d = \begin{bmatrix} a - b\sin^2\varphi & -b\sin^2\varphi & 0 & 0 \\ -b\sin^2\varphi & b(1+\cos^2\varphi) & 0 & 0 \\ 0 & 0 & 2b\cos\varphi & 0 \\ 0 & 0 & 0 & 2c\cos\varphi \end{bmatrix} \quad (4.3)$$

where φ is the scattering angle (Figure 4.2). The information on photoselection can be obtained from the parameters a and b.[257]

For a linear oscillator in an isotropic medium, we can relate these parameters to the dipolar angles as,

$$a = \frac{1}{2}(1 + \langle\cos^2\theta\rangle), \quad \text{and} \quad (4.4)$$

$$b = \frac{1}{4}(3\langle\cos^2\theta\rangle - 1) \quad (4.5)$$

where θ is the angle between the emission dipole and azimuthal angle of the polarization of the excitation light (Figure 4.2). Therefore, the diagonal elements in the Mueller matrix provide the information on fluorescence anisotropy. However, the directly extractable quantity is in fact the fluorescence polarization, since the normalization with total intensity in this measurements considers only $I_{\parallel}$ and $I_{\perp}$(in the XY plane in Figure 2.2.b) which are in the plane of the sample. Whereas intensity perpendicular to the sample (in the direction of light propagation) is not measured. Therefore, to determine anisotropy from fluorescence polarization, we have to use the relation,

$$r = \frac{2p}{3-p}. \quad (4.6)$$

Theoretically, if the emission and absorption dipoles are collinear, $\langle\cos^2\theta\rangle$ is $\frac{3}{5}$, and if the dipoles are randomly oriented, the average value is $\frac{1}{3}$.[251] Therefore, when the absorption and emission dipoles are collinear ($p = 2b$), we obtain the maximum value for fluorescence polarization as $p = 0.4$ (estimated from Eqn. 4.3 and 4.4).

The parameter *c* is related to the optical activity of the material. For a linear oscillator, c=0, whereas, if we consider an elliptical or circular oscillator, where the electric and magnetic transition dipole moments are either parallel or antiparallel with the same magnitude giving a high rotational strength (discussed in Section 1.5 of Chapter 1), the parameter *c* is nonvanishing. For such a system, the limiting values of *b* and *c* are 1/20 and 5/16, respectively.

In general, the magnetic dipole only has a small component parallel to the electric dipole, describing as an elliptical oscillator that makes *c* much smaller than *a* and *b*.[257]

In such a case where c<<a,b, and for exact forward or back scattering ($\varphi = 0$ or π) we obtain the direct measurement of FDCD and CPL from the normalized Mueller matrix.

Further, we can write the matrices M_0 and M_1 as,

$$M_0 = \begin{bmatrix} 1 & m_0 & n_0 & p_0 \\ m_0 & r_0' & 0 & 0 \\ n_0 & 0 & r_0'' & 0 \\ p_0 & 0 & 0 & r_0''' \end{bmatrix} and\ M_1 = \begin{bmatrix} 1 & m_1 & n_1 & p_1 \\ m_1 & r_1' & 0 & 0 \\ n_1 & 0 & r_1'' & 0 \\ p_1 & 0 & 0 & r_1''' \end{bmatrix} \quad (4.7)$$

where the parameters m_0, n_0, p_0 corresponds to horizontal/vertical linear, ±45 linear and circular differential absorption for the fluorescence (diattenuation), respectively. On the other hand, the parameters m_1, n_1, p_1 correspond to horizontal/vertical linear, ±45 linear and circular differential emission (polarizance) under orthogonal polarization, respectively.

By bringing in the above discussed approximations that 2c<<2b<<a (corresponding to strong depolarization effects in the transfer matrix, M_d), and $\varphi = 0$ or π (i.e. forward or backward fluorescence measurements), we can write the total Mueller matrix elements (M_{ij}) of Eqn.4.2 in terms of the elements of the absorption and emission anisotropy matrices, $M_{i=0,1}$ as

$$\frac{M_{01}}{M_{00}} = m_0, \frac{M_{02}}{M_{00}} = n_0, \frac{M_{03}}{M_{00}} = p_0, \quad (4.8)$$

$$\frac{M_{10}}{M_{00}} = m_1, \frac{M_{20}}{M_{00}} = n_1, \frac{M_{30}}{M_{00}} = p_1 \quad (4.9)$$

Therefore, the linear and circular anisotropy parameters can be directly extracted from the Mueller matrix. We can now define the anisotropy parameters in the following manner,

$$\alpha_T = \frac{\sqrt{M_{01}^2+M_{02}^2+M_{03}^2}}{M_{00}}, \qquad \alpha_L = \frac{\sqrt{M_{01}^2+M_{02}^2}}{M_{00}}, \qquad \alpha_C = \frac{M_{03}}{M_{00}} \quad (4.10)$$

$$\beta_T = \frac{\sqrt{M_{10}^2+M_{20}^2+M_{30}^2}}{M_{00}}, \qquad \beta_L = \frac{\sqrt{M_{10}^2+M_{20}^2}}{M_{00}}, \qquad \beta_C = \frac{M_{30}}{M_{00}} \quad (4.11)$$

where α_T, α_L, α_C are the total, linear (FDLD) and circular (FDCD) fluorescence diattenuation, respectively. And, β_T, β_L, β_C are the total, linear (LPL) and circular (CPL) polarizance, respectively.[254]

The off-diagonal elements such as m_{12}, m_{21}, m_{13}, m_{31}, m_{32}, and m_{23} represent retardance or dephasing between the orthogonal circular and linear polarization phases.

4.2.2 Dipolar orientation

From the Mueller matrix, we can also estimate the orientation of the transition dipoles involved in the absorption (θ_{exc}) and emission (θ_{emiss}) process.

$$\theta_{exc} = \pm\frac{1}{2}tan^{-1}\left(\frac{M_{02}}{M_{01}}\right),\ \ \theta_{emiss} = \pm\frac{1}{2}tan^{-1}\left(\frac{M_{20}}{M_{10}}\right) \tag{4.12}$$

We can also estimate the dipolar orientational order for the excitation and emission by defining an angular distribution function as,

$$f(\theta) \propto e^{-\frac{(\theta-\theta_{ex/em})^2}{2\Delta\theta_{ex/em}{}^2}} \tag{4.13}$$

where $\Delta\theta$ is determined by estimating α_L in the following manner expressed as

$$\alpha_L = \sqrt{\frac{(I_H-I_V)^2}{(I_H+I_V)^2} + \frac{(I_P-I_M)^2}{(I_P+I_M)^2}} \tag{4.14}$$

where I_H, I_V, I_P, I_M are emission intensity when excited with light polarized in horizontal, vertical, +45 and -45 directions.

These fluorescence intensities can be expressed as,

$$I_H \propto \int_0^\pi \left|\mu \cdot E_H\right|^2 f(\theta)d\theta \ \propto \int_0^\pi cos^2(\theta)\, f(\theta)d\theta \tag{4.15}$$

$$I_V \propto \int_0^\pi \left|\mu \cdot E_V\right|^2 f(\theta)d\theta \ \propto \int_0^\pi sin^2(\theta)\, f(\theta)d\theta \tag{4.16}$$

$$I_{P/M} \propto \int_0^\pi \left|\mu \cdot E_{P/M}\right|^2 f(\theta)d\theta \ \propto \int_0^\pi cos^2(\theta \pm \pi/4)\, f(\theta)d\theta \tag{4.17}$$

Similarly, β_L is also evaluated. By estimating α_L and $\beta_L$in Eqn. 4.8 and 4.9, and comparing with the evaluation using the Eqn. 4.12, we can obtain the dipolar orientation

angles and their distribution order.[243] This discussion will be carried out further in Section 4.10 using the Mueller matrix.

4.2.3 Additivity of anisotropy

For a complex heterogeneous system, anisotropy measurement can be challenging when each constituent brings its own contribution to the total anisotropy. [251]

The individual anisotropy, r_i, can be expressed as,

$$r_i = \frac{I_{\parallel}^i - I_{\perp}^i}{I_{\parallel}^i + 2I_{\perp}^i} = \frac{I_{\parallel}^i - I_{\perp}^i}{I_i} \tag{4.18}$$

and each species contributes to the total anisotropy with a fraction, $f_i = \frac{I_i}{I}$ and $\sum f_i = 1$

Therefore, the total anisotropy, $r(\lambda)$ can be expressed as,

$$r(\lambda) = \sum_i f_i(\lambda) r_i(\lambda) \tag{4.19}$$

Here again, from Mueller matrix, we obtain fluorescence polarization for individual species, p_i instead of r_i, and one has use Eqn 4.6 to determine the fluorescence anisotropy.

4.3 Experimental protocols and results: excitation wavelength-dependent emission spectra of C8O3 aggregates

Further in this Chapter, we present the experimental protocols and the results of 2D-Ex-Em Mueller matrix on C8O3 aggregates.

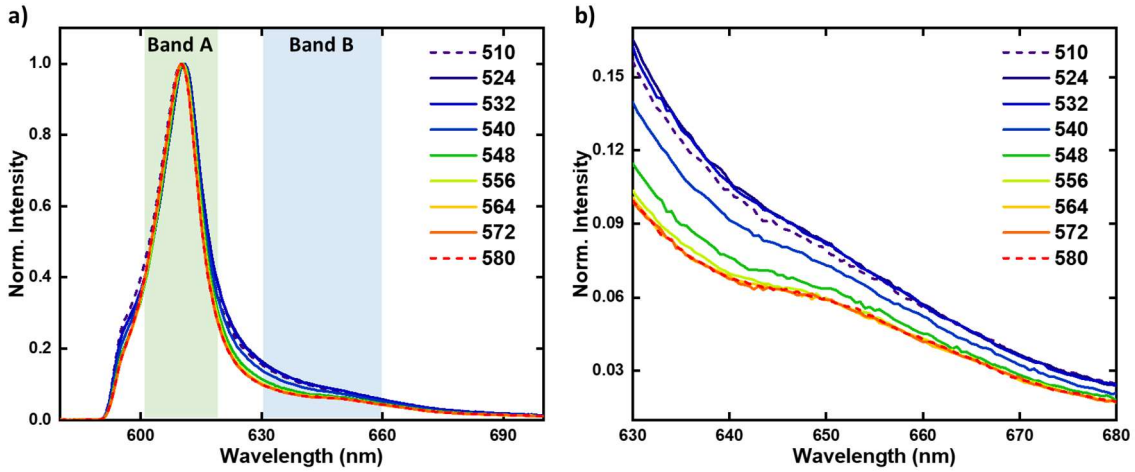

Figure 4.3: *a) The normalized emission spectra of the C8O3 aggregate excited from 510 to 580 nm with two emission bands marked A (emission maxima around 610 nm) and B, and b) the zoomed emission spectra showing intensity variations in band B .*

Before going deeper into the analysis of 2D- Ex-Em Mueller matrix, the unpolarized emission spectra needs special attention. The unpolarized emission spectra of C8O3 aggregates with the excitation from 510 nm to 580 nm normalized to the emission maximum are presented in Figure 4.3. They show two emissive bands, one narrow band (A) centred at 610 nm and a broad band (B) ranging from around 630-660 nm which shows intensity variation with excitation wavelength. At band B, the spectra show higher intensity when excited at lower wavelength from 510 nm to 540 nm. This feature reduces in relative intensity as the excitation wavelength moves closer to the absorption of the transverse exciton of the aggregate, along with the narrowing of band B. With the 2D- Ex-Em Mueller matrix that gives polarimetric anisotropy signatures, these spectral variations at higher emission wavelength can be correlated to obtain more insight on the emissive nature of the aggregates.

4.4 Measuring the 2D-Ex-Em Mueller matrix

We perform the emission Mueller matrix measurement by exciting the sample from 510 to 580 nm. These measurements are then combined to form a 2D colourmap with excitation wavelength on the y-axis and emission wavelength on the x-axis. The normalized 2D- Ex-Em Mueller matrix of C8O3 aggregates characterized in Chapter 2 are presented in Figure 4.4. To generate the Mueller matrix, we use the same experimental setup and procedures detailed in Chapter 2. Emission Mueller matrices are measured by exciting the sample from 510 nm to 580 nm sequentially at the same position of the sample. Before beginning this continuous

Mueller matrix measurements, we first perform an emission and transmission Mueller measurement from the same position to make sure that the probing region is populated with bundled aggregates. In addition, this transmission Mueller matrix is used for the re-absorption correction to the emission Mueller matrix for all the excitation wavelengths as explained in the Section 2.5.6 in Chapter 2.

In the normalized 4x4 2D- Ex-Em colormap of Figure 4.4, the first column providing the information on LPL in m_{10} and m_{20} (LPL′) and, CPL in m_{30} does not vary its intensity with the wavelength of excitation, but shows large values along with CPL signals bisignated at the emission maximum. This is because the anisotropic emissive property of the aggregate with an unpolarized excitation beam is independent of its excitation wavelength and only show its excited state properties. On the other hand, the first row elements with m_{01} and m_{02} as the FDLD and FDLD′, increases in magnitude (with negative sign) in accordance with the increase in the anisotropic absorption of the aggregate (increase in excitation wavelength). The m_{03} coefficient containing the information of FDCD, is very low as the chiral absorption for the excitation from 510-580 nm remains itself very low.

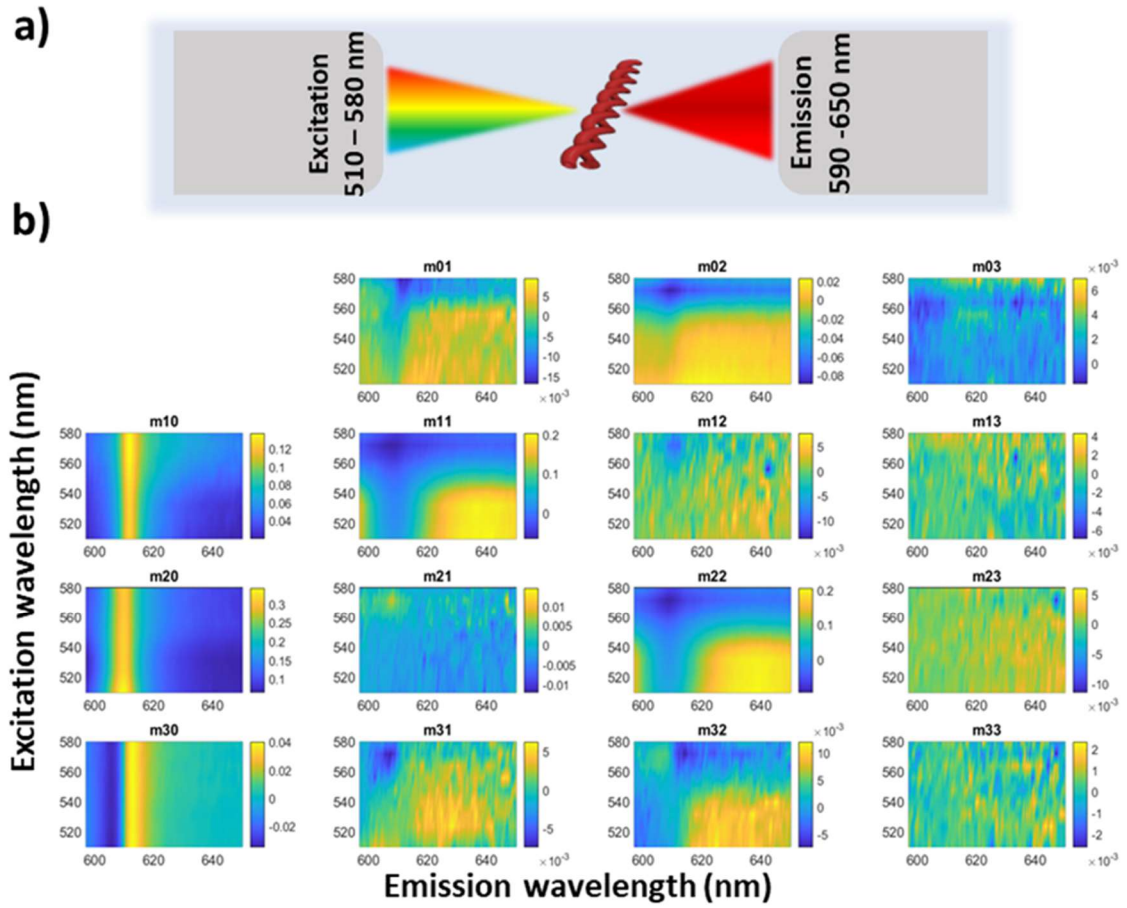

Figure 4.4: *a) Schematics of the excitation and emission configuration with wavelength range are presented. b) The associated normalized 2D- Ex-Em Mueller matrix of the aggregate.*

More significant spectral variations are shown in m_{11} and m_{22} that identify the presence of depolarization of optical signals along with providing fluorescence anisotropy (intrinsic anisotropy) free from the anisotropy due to orientation of the system (extrinsic anisotropy). Depolarization occurs when a molecular system with non-uniform orientational distribution after polarized excitation undergoes rotational diffusion to reduce anisotropy in emission limiting the dipolar orientation analysis. However, in a film this depolarization diminishes due to restricted rotational diffusion, and the dipolar orientations can easily be determined without much ambiguity. These elements (m_{11} and m_{22}) show strong negative signal around 610 nm (in emission) only when the excitation wavelength is above 550 nm where the transverse exciton (see Figure 3.4 of Chapter 3) of the aggregate strongly absorbs, and increase in magnitude as the excitation wavelength increases to 580 nm. In addition, we observe strong anisotropy signature with high positive value at band B (Figure 4.3) only when excited at lower wavelength where the monomer strongly absorbs (510 nm to 540 nm). This long wavelength

emission can either be the result of a vibronic transition, trapped exciton, or originating from monomeric emission. The higher wavelength emission is reasoned as vibronic transition in tubular C8O3 aggregate, while it is identified as self-trapped states in some similar Cyanine based aggregates.[260–263] Therefore, careful analysis is required to identify the exact origin of this peak. The other elements in the Mueller matrix remain very low near to the noise floor of our detection. Further in this Chapter, we will try to analyse the behaviour of anisotropic evolution of various Mueller matrix elements along with identifying the origin of the spectral variations in the diagonal elements by investigating the speculations made in this Section. However, verifying the possibility of trapped exciton requires time-resolved measurements which resides beyond the scope of current methodology.

4.5 2D- Ex-Em Mueller matrix of aggregates at higher emission wavelength

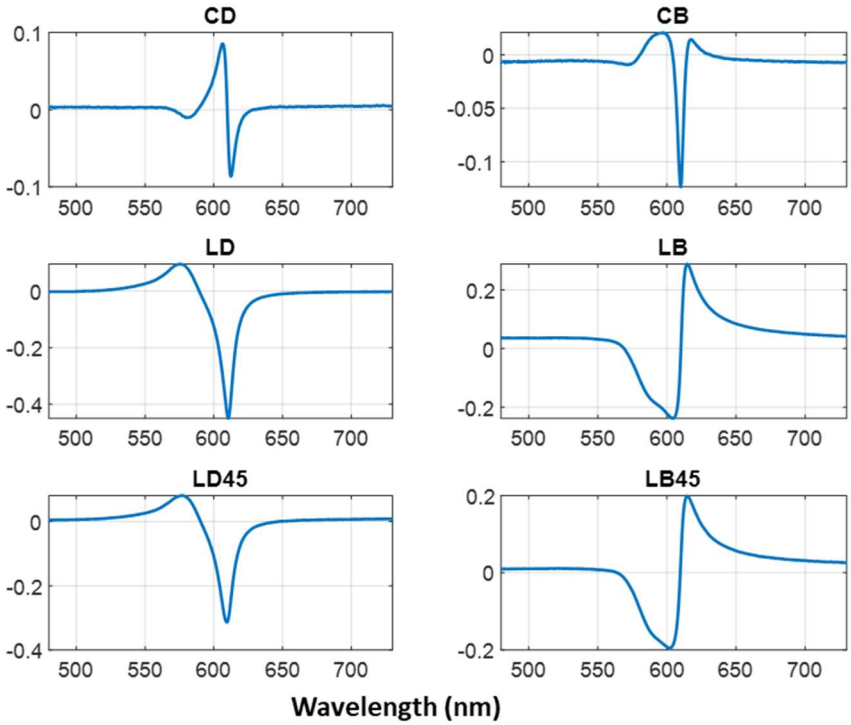

Figure 4.5: *The CD, CB, LD and LB of the C8O3 bundles obtained through transmission Mueller measurement.*

To verify whether the fluorescence anisotropy signals arise from aggregated or monomeric forms, it is important to check the behaviour of the C8O3 aggregates by exciting

their longitudinal exciton. Therefore, we performed a similar 2D- Ex-Em Mueller measurement exciting from 580 nm to 610 nm, while collecting emission from 627 nm. Here, we have used a different sample, and the observables extracted from the transmission Mueller matrix are shown in Figure 4.5. Therefore, the extrinsic anisotropy parameters such as FDLD and FDCD have to be compared with the LD and CD signals in Figure 4.5. However, the diagonal elements remain similar as they corresponds to the intrinsic properties of transition dipole orientation in the aggregate. The slight variations in the signal in these matrix elements compared to Figure 4.3 occur mainly because of the inhomogeneity of the sample. The results presented in Figure 4.6, shows the elements m_{11} and m_{22}, that are initially being negative near the excitation of transverse exciton (from 550- 590 nm), slowly becomes positive as the excitation wavelength approaches the longitudinal absorption (above 590 nm). This signal evolution is in agreement with the transverse and longitudinal excitonic characteristics of the aggregate, that are constant throughout the emission wavelengths.

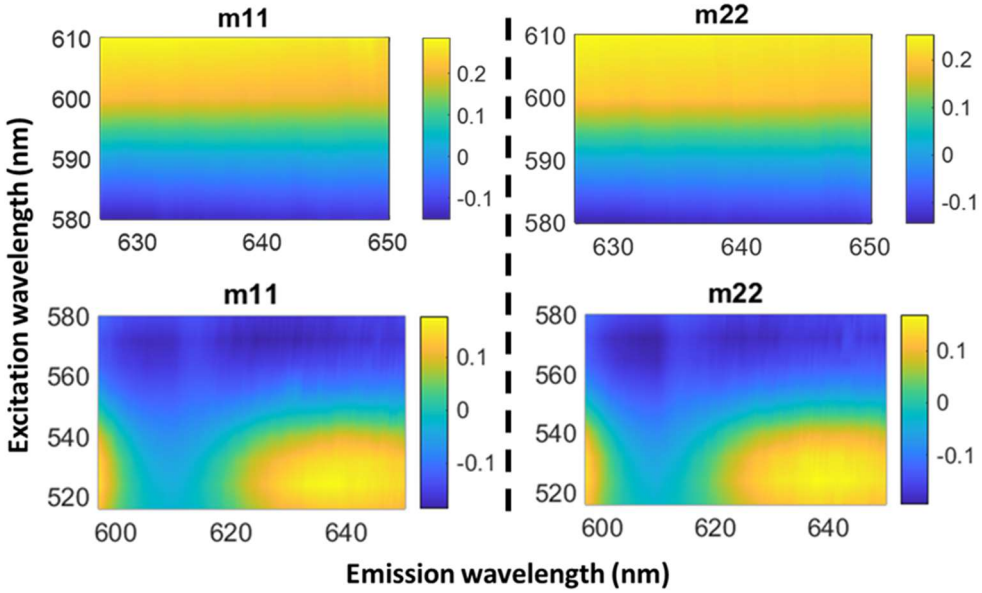

Figure 4.6: *The diagonal matrix elements of the 2D-Ex-Em Mueller matrix, generated by excitating C8O3 aggregates from 516 nm to 610 nm. These elements show the anisotropy evolution over excitation and emission wavelengths. The left panel shows m_{11} and the right panel shows m_{22} matrix elements which are identical to each other.*

This spectral feature of emission band B (see Figure 4.3) that follows the excitation polarization near the transverse and longitudinal exciton, however differs at smaller wavelength of excitation as seen in the wavelength range of 516-550 nm in both m_{11} and m_{22} as seen from Figure 4.6. This signature suggests that the origin of band B is excitonic in nature

when the aggregate is preferentially excited, and that it preserves the polarization features similar to that of band A. Hence, the origin of band B can be understood as the vibronic emission of the aggregate from the lowest excited state. While, at lower wavelength of excitation, both monomer and aggregate is excited giving a mixed polarimetric response. This could probably be due to the interplay of high fractional contribution (discussion in Section 4.2.3) of aggregate emission at band A in comparison to monomer, while it is very low near band B. This argument is supported by the similar positive signal observed below 600 nm in emission for excitation from 510 nm to 540 nm.

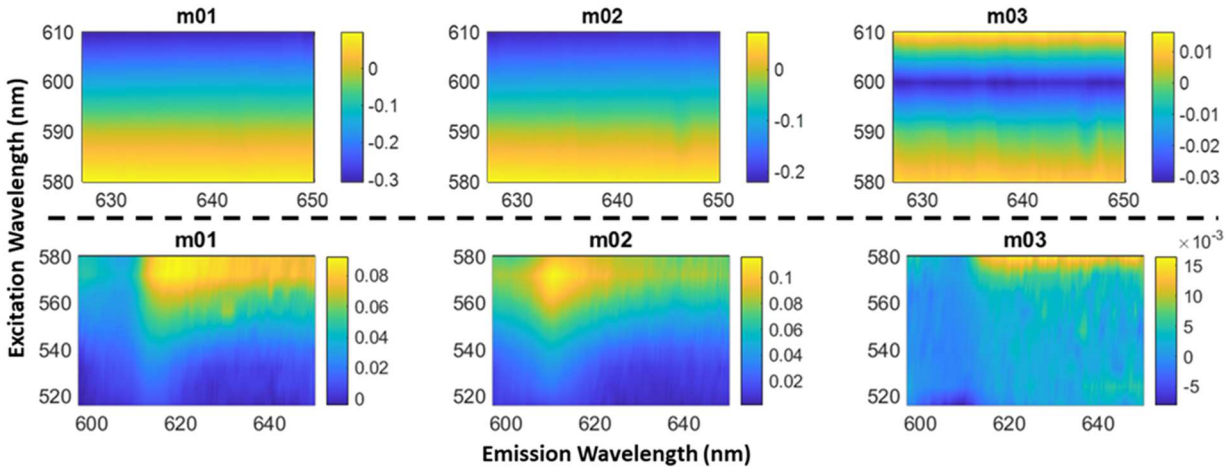

Figure 4.7: *The matrix elements showing wavelength-dependent ground state anisotropy such as FDLD (m_{01}), FDLD′ (m_{02}) and FDCD (m_{03}). The bottom panel corresponds to matrix elements with excitation wavelength from 516 nm to 580 nm, and the top panel corresponds to those with excitation wavelength from 580 nm to 610 nm.*

Apart from the diagonal terms, other elements of the matrix also show interesting signal evolutions when excited near the longitudinal exciton. In Figure 4.7, the signals in m_{01} and m_{02} that correspond to FDLD and FDLD′, respectively, change sign from positive to negative when the excitation changes from transverse to longitudinal absorption of the aggregate, tracing the LD and LD′ behaviour in Figure 4.5. The signal in m_{03} also shows remarkable features. Initially being positive, it falls to zero around 590 nm, moving to a strong negative value at 600 nm, which again goes back to zero to reach a strong positive value around 610 nm. This FDCD signal clearly traces down the bisignate CD signature. It is important to note here that the FDLD and FDCD we obtain are reversed in sign compared with LD and CD signals. This is simply due to the differences in the sign of Mueller matrix elements in transmission and emission as discussed in Chapter 2 (see Sections 2.4.4 and 2.4.8). Furthermore, the Mueller matrix elements

that showed low signals (m_{12}, m_{13} and m_{23}) with excitation at the transverse exciton (510-580 nm) are highly responsive when excited near longitudinal exciton (580-610 nm) as shown in Figure 4.8. These matrix elements indicate that the excitation beam and emitted light show phase changes between linear and circular orthogonal polarizations. This results are intriguing, however, further work is required for understanding the significance of these polarimetric signatures in supramolecular structures.

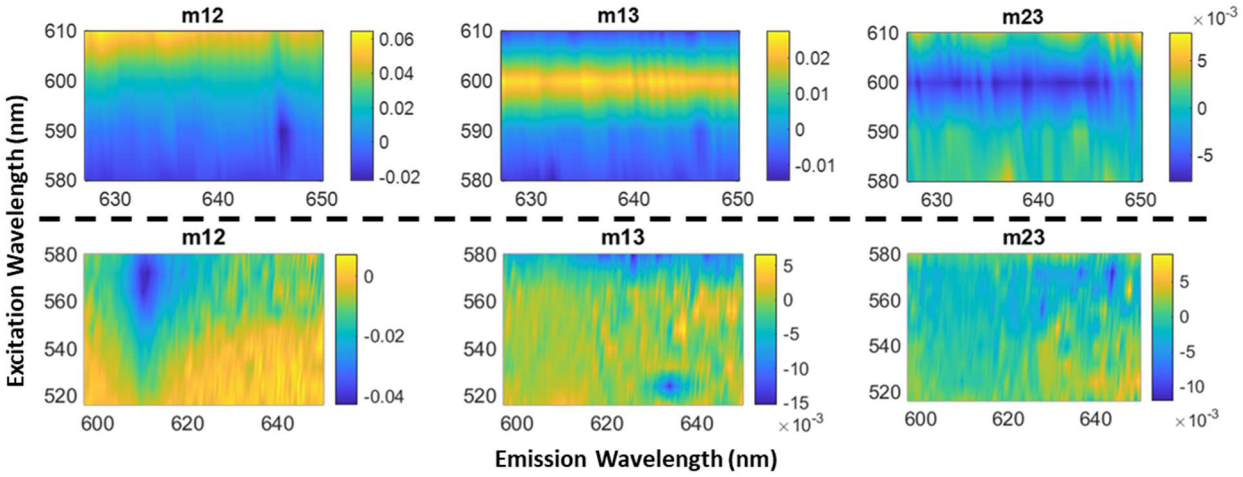

Figure 4.8: *The matrix elements showing wavelength-dependent evolution of the off-diagonal elements*

4.6 Fluorescence polarization evolution

Characterizing the wavelength depended evolution of excitation and emission polarization provides information on the orientation of transition dipoles in a complex molecular system. It could also aids in clarifying the origin of intensity variations in band B presented above in Section 4.3. To better understand the polarization evolution in C8O3 aggregates, we have plotted the fluorescence polarization spectrum for the two emission bands, which is presented in Figure 4.9.

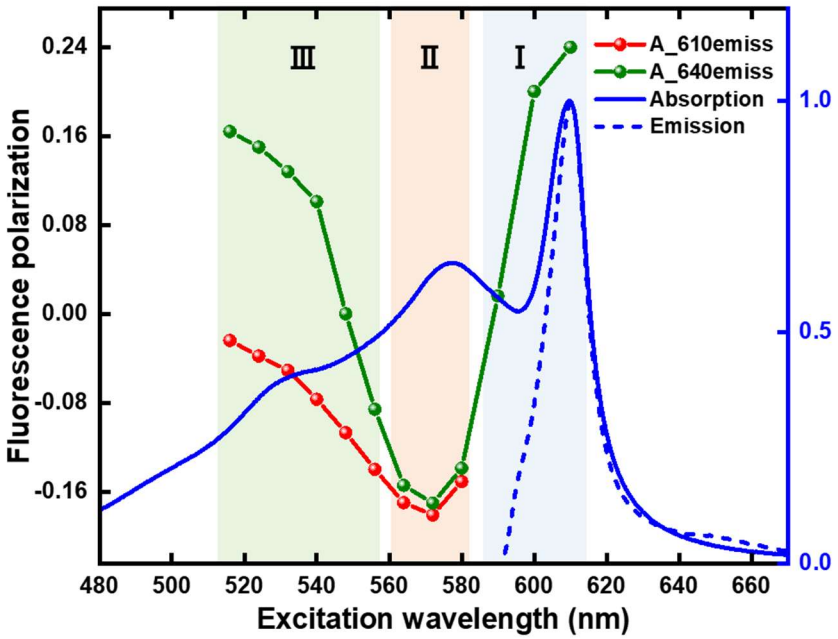

Figure 4.9: *Fluorescence polarization spectra for emission at 610 nm and 640 nm (plotted using Figure 4.6). The three regions are divided based on the fluorescence polarization evolution.*

From the m_{11} and m_{22} elements of the 2D- Ex-Em Mueller matrix (Figure 4.6), we divide the wavelength range from 516 nm to 610 nm into three regions defining the polarimetric properties of longitudinal exciton (region I), the transverse exciton (region II) and the region that combines the features associated with both monomers and aggregates (region III). The fluorescence polarization value is taken as the average of the signal in m_{11} and m_{22} corresponding to each excitation and emission wavelength. The result in Figure 4.9 shows a clear transition when the excitation wavelength changes from the monomeric (region III) to the aggregate (region I and II) absorption for both emission at 610 nm and 640 nm. The fluorescence polarization for the 640 emission, which was almost constant with high positive value up to 540 nm, immediately begins to reduce showing an isotropic absorption or high depolarisation of emission as the aggregate begins to absorb. In contrast, the almost isotropic absorption in the green region in Figure 4.9 for emission at 610 nm begins to be more anisotropic as the excitation wavelength favours aggregate absorption with the signal becoming more negative with increase in excitation wavelength.

Near to the absorption of transverse exciton, both the anisotropy profiles for the two emission converge, conveying that the states involved in the two emission are the same. This fluorescence polarization evolution clearly suggests that the differing anisotropy evolution

towards lower wavelength for both the emission wavelengths originates from the mixed response of the monomer and the aggregate. This argument is supported by the spectral variation observed in the unpolarized emission signal in Figure 4.3 where the band B converges when the aggregate is preferentially excited from 560 to 580 nm. Also, the signals in m_{11} and m_{22} near band B in Figure 4.6 with excitation from 550 nm to 610 nm retains the feature of band A. These results indicate that the band B originates from a mixed response of vibronic emission from monomer and aggregate.

4.7 Comparison of excitation spectra of C8O3 aggregates in solution and in the solid state

The results discussed in Section 4.6 suggests the importance of analysing the contribution of both monomers and aggregates to the emission at band B. Therefore, we performed excitation spectroscopy for the film and compared the result with that of aggregates in solution prepared at two different C8O3/NaOH ratio. Here, the absorption spectrum is measured using Shimadzu UV26000i and the excitation and emission spectra are taken using Fluorolog QM from Horiba Scientific for both solution and film. This measurement in film does not yield a very accurate result since it does not focus the beam on a microscopically small region (similar to Mueller measurement) to avoid exciting multiple aggregate species along with monomer. Therefore, the results presented consists of an ensemble averaged results. Even though, the measurement can provide a global understanding of the different spectroscopic signatures of aggregated samples.

Aggregation stages controlled at different ratios of NaOH have previously been studied, where a ratio of 1:4 gives mostly bundles and 1:3 gives mostly tubular aggregates.[264] In Figure 4.10, we have studied the excitation spectrum at 605 nm and 650 nm emission. The normalized excitation spectrum overlapping with the absorption spectrum clearly identifies the contrast between the properties of aggregate in film and in solution. We see this contrast with the presence of an absorption peak at 530 nm in the excitation spectrum taken from film state while it is absent in the excitation spectrum of aggregates in solution. In addition, higher intensity for emission at 650 nm than 605 nm are observed when excited around 540 nm which strongly supports the mixed fluorescence response with higher contribution from the monomer identified for band B (Figure 4.3) in Section 4.6.

In contrast, the excitation spectra for aggregates in solution at the two emission wavelengths do not show any difference in the spectral profile. This suggests that the monomer contributes mostly to the emission at 650 nm in the film, which could indeed result in a mixed response to the total fluorescence polarization observed at band B. Moreover, we also speculate on the possibility of energy transfer from monomers to aggregate in the film. This appears to us as highly probable in films considering the overlap between the absorption spectrum of the aggregate and the emission spectrum of the monomer, and also considering the restricted proximal arrangement of these two species, making the energy transfer process more feasible.

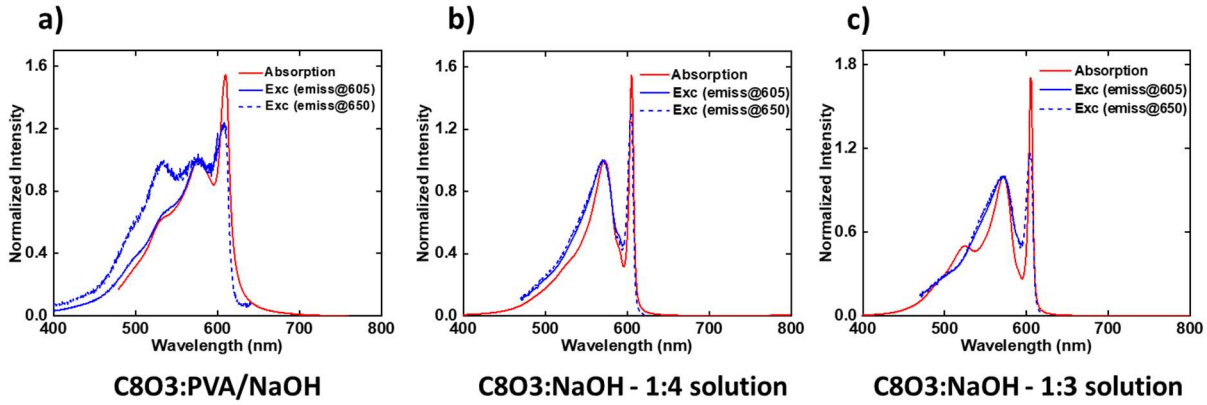

Figure 4.10: *Excitation spectra of a) aggregate film, b) aggregate solution at 1:4 ratio, and c) aggregate solution at 1:3 ratio of C8O3 solution and NaOH solution.*

4.8 2D- Ex-Em Mueller matrix of C8O3 monomers near the aggregate emission

To look more precisely on the contribution of monomers to fluorescence polarization at longer wavelength, we have performed a 2D- Ex-Em Mueller measurement on a film of monomer by exciting from 490 nm to 530 nm, and collecting emission from 600 nm to 650 nm. These films are obtained by annealing the aggregated film by heating it up to 120℃. The absorption spectrum, and the polarimetric observables from the transmission Mueller measurement are presented in Figure 4.11.

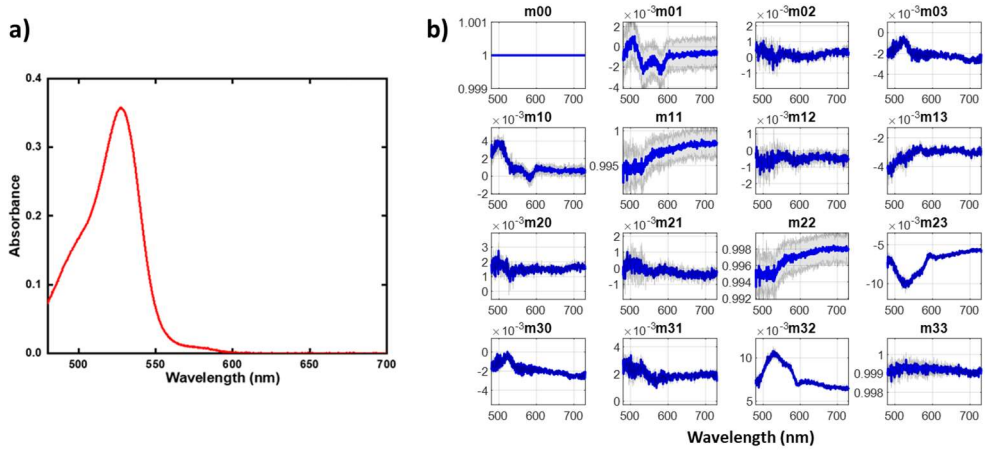

Figure 4.11: *(a) Absorption spectrum (red trace) and transmission Mueller matrix of C8O3 monomeric film. The signals in the Mueller matrix are very low of the order* 10^{-3}*, close to detection limit of the optical setup. The grey-shaded region represents the error bar for each element estimated through the standard deviation calculated from the empty Mueller matrix.*

The 2D- Ex-Em Mueller matrix presented in Figure 4.12 shows fluorescence polarization signature in m_{11} and m_{22} with a value ranging from 0.14 to 0.16. This value is very close to that seen in Figure 4.9 in region III (green line) suggesting that the significant contribution to band B is the emission from monomer. The other elements in the Mueller matrix remain at a very low the level of intensity to reveal any contribution from the monomer to the Mueller matrix of the aggregate.

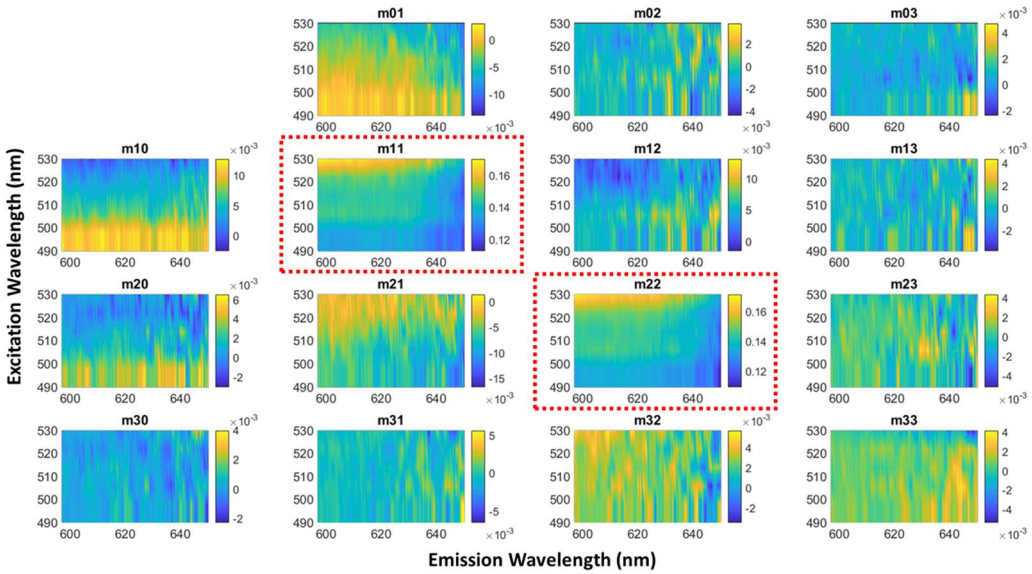

Figure 4.12: *Emission Mueller matrix of C8O3 monomeric film showing positive fluorescence polarization signals in the diagonal elements (highlighted with red dotted box) with values closer to those obtained from the aggregate film (see Figures 4.6 and 4.9).*

4.9 Energy level diagram

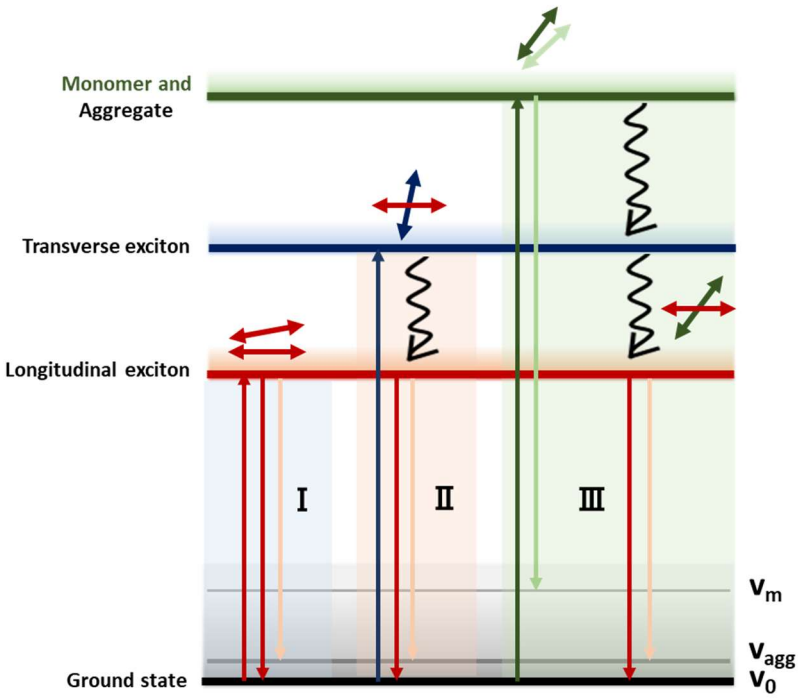

Figure 4.13: *Energy level diagram drawn using the 2D- Ex-Em Mueller matrix which shows the different transitions involved together with the dipole orientations for the electronic and vibronic transitions associated with the absorption regions I, II and III (Figure 4.9), and emission bands A and B (Figure 4.3).*

With the help of the 2D- Ex-Em Mueller matrix, herein, we describe the full ground and excited state polarimetric transition properties of the aggregate, and present the energy level diagram of the system in Figure 4.13. Here we ignore the chiroptical properties described in Chapter 3, and therefore the two split excited states (S^+ and S^-) are not separately shown since they both have longitudinal excitonic characteristics. In Figure 4.13, we show two electronic excited states, longitudinal (red) and transverse states (blue) of aggregate, and an excited state of monomer and aggregate at higher energy (green). For the ground state, we show the lowest vibrational level, v_0 and two ground vibrational states, the lowest among the two correspond to the aggregate marked as v_{agg} and the highest corresponding to monomer marked as v_m. This distribution of vibrational states is chosen to account for the energetic overlapping of monomeric and aggregate emission at band B in Figure 4.3. Here, to understand the energy level distribution, we use the information of fluorescence polarization in Figure 4.9. Once the sample is excited in the regions I and II, transitions involve the longitudinal and transverse excitonic states, respectively. From the transverse excited state, the system relaxes to the

longitudinal excited state. From this state, the system then radiatively emit to v_0 and v_{agg} giving rise to the two emission bands (A and B in Figure 4.3) for aggregate. In addition, when we excite in the region III, we observe two emission lines, one corresponding to the emission from aggregate after relaxing non-radiatively to the longitudinal exciton, and the other from the monomeric excited state to the ground vibrational state of the monomer. Note that exciting the monomer could also involve an energy transfer process from which emission proceeds from the longitudinal excited state of the aggregate.

Herein, we also derive the relative dipole orientations based on the sign of fluorescence polarization in Figure 4.9 and the knowledge that an average angle less than 54° gives a positive value for fluorescence polarization while a negative sign says that the angle is above 54°.[251] In region I in Figure 4.9, the fluorescence polarization is highly positive reaching to a value of 0.24, showing that the emission dipole associated with the longitudinal transition (double arrow in red) is aligned with the ground state dipole (double arrow in red) at an average angle less than 54°. In the region II, the polarization reaches to a minimum value close to -0.16, that gives an average angle higher than 54° for the transverse exciton (double arrow in blue) compared to the ground state dipole. In region III, we have two processes simultaneously occurring with excitation and emission overlapping within similar wavelength regions. Separating the individual fluorescence polarization is difficult with steady state measurements, and one would have to resort to time-resolved measurements to identify the individual components as the two species are expected to show different excited state lifetimes. However, comparing the fluorescence polarization of monomer in film with positive signal close to 0.16 shows that the dipoles are aligned at an angle below 54° (double arrows in green), while the aggregate must be showing an angle above 54° (green double arrow) to give a negative fluorescence polarization value so that the total signal averages to 0 in region III for the red trace. It is important here to note that the actual anisotropy of the aggregate may have been reduced because of the increased scattering due to its large size compared to the size of a monomer. This feature is intrinsic and an unavoidable property of our material.

4.10 Fluorescence dipolar orientation extracted from the Mueller matrix

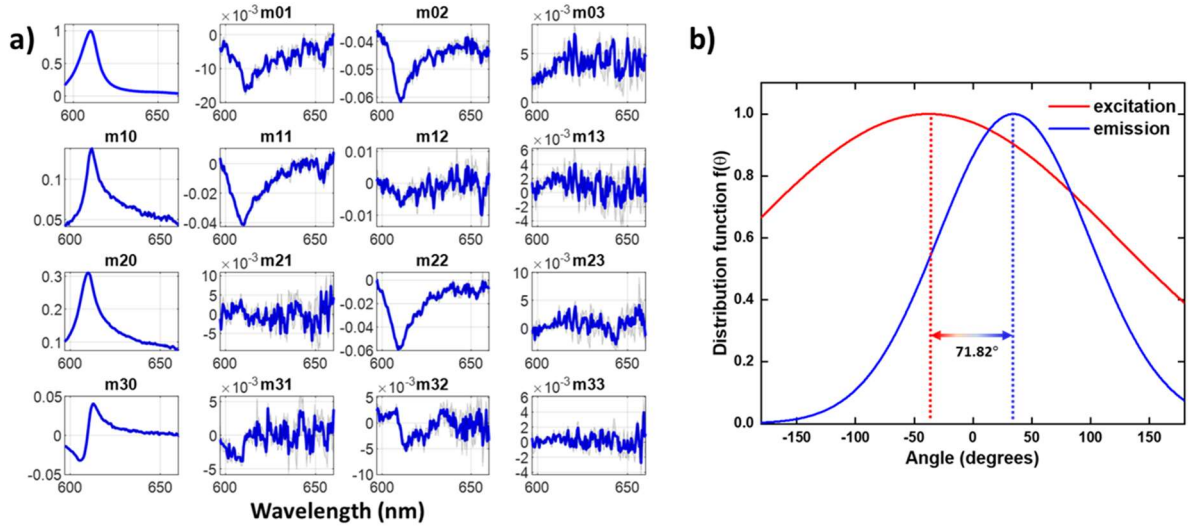

Figure 4.14: *a) Emission Mueller matrix of C8O3 aggregate excited at 580 nm, b) Plot of dipole distribution function for excitation and emission.*

The dipolar orientational order or distribution is another important information that can be extracted from the emission Mueller matrix (Section 4.3.2). This information is essential in understanding the structure-property relation, as clearly stressed by K. Maji et. al, who quantified the orientation parameters and analysed the formation of decorated supramolecular tubes.[243] Herein, we have determined the orientational order of the C8O3 bundled aggregate by analysing the Mueller matrix of the sample excited at 580 nm presented in Figure 4.14.a, and using the theoretical descriptions provided in Section 4.2.2.

Table 4.1: *The ground and excited state dipole orientation parameters used to plot Figure 4.14.*

	Excitation at 580nm	**Emission at 610nm**
Orientation angle	θ_{exc} = -37.44°	θ_{emiss} = 34.38°
Angular distribution	$\Delta\theta_{exc}$ = 158.4°	$\Delta\theta_{emiss}$ = 63.9°
Linear anisotropy	α_L = 0.0641	β_L= 0.331

The angular distribution parameters are estimated from the m_{01}, m_{02}, m_{10} and m_{20} elements of the Mueller matrix using expressions in the Section 4.2.2, and are presented in Table 4.1. The distribution functions for excitation and emission dipole are plotted in Figure 4.14.b. Here, it is important to note that the sign of the orientation angle ($\theta_{exc}/\theta_{emiss}$) based on equation 4.10 has to be decided comparing the sign difference between the m_{01} and m_{10} elements (similarly for m_{02} and m_{20}) of the Mueller matrix. Since the sign reverses for these elements, we chose opposite signs for θ_{exc} and θ_{emiss}. Hence, the calculation yielding similar dipolar angles in magnitude with opposite sign shows that the transverse and longitudinal excitons are oriented with an angle of 71.82°**,** which is consistent with the fluorescence polarization analysis performed in Section 4.9 of this Chapter. The spread of the distribution function for excitation and emission dipoles is also remarkable. This result shows that the emission dipole is more oriented (distribution function is more narrow) in comparison with that of the excitation dipole. Similar results were also identified by K. Maji et. al, from the fluorophores oriented on nanotubes. This difference in orientational order for excitation and emission dipoles that we measure is remarkable and certainly requires further studies to understand its microscopic origin.

4.11 Conclusions

To summarise, in this Chapter, we explored the excited state polarimetric properties of the C8O3 bundled aggregates by performing 2D-Excitation-Emission Mueller Polarimetry. This gave us information on the fluorescence-detected ground state properties such as FDLD, FDCD, and the excited state properties such as LPL and CPL. It also provided information on the fluorescence dipolar orientation that is free from artefacts due to orientational distribution of the system in the sample.

Understanding the anisotropic properties of a system is essential that yields the crucial information on structural and dynamical aspects of the system. High anisotropy and inhomogeneity of a sample hinders the real anisotropy characterization in the conventional methodologies. With the C8O3 aggregate film, that is highly anisotropic and inhomogeneous in addition to showing zero-Stokes shift in emission, accessing the anisotropic features turns out to be highly challenging. Herein, using Mueller polarimetry, we extracted the intrinsic fluorescence polarization and extrinsic anisotropic properties of the aggregate films, and

studied its excitation wavelength dependency. Analysing the associated spectral variations, we derived the distribution of energy levels in these aggregates and presented the corresponding dipole orientations. Additionally, we were able to extract the average angle between the excitation and emission dipoles from the Mueller matrix. Furthermore, we obtained additional information regarding the polarization dephasing between excitation and emission dipoles, and also the dipole distribution order within the sample.

The aggregated sample is very complex not only due to the anisotropic orientation but also due to the presence of multiple components such as the presence of residual monomeric species along with tubular and bundled aggregates. Here, we showed that the characterization of samples with the 2D- Ex-Em Mueller matrix can help in deriving these multi-component anisotropy contributions. However, considering the complexity and sensitivity of supramolecular aggregation, where different types of aggregates are formed at slightly different environmental conditions, better interpretations can be reached when Mueller polarimetry is coupled with lifetime measurements. This procedure could yield a time-dependent anisotropy characterisation where multiple aggregate species can easily be identified without much ambiguity. Moreover, this method could shed interesting light on the existence and influence of self-trapped excitonic states on the emissive properties of our samples.

Chapter 5

Aggregate disassembly pathway: polarimetric characterization through thermal annealing

In this Chapter, we follow the disassembly pathway of a film of bundled aggregates of C8O3 using temperature-dependent Mueller polarimetry. Employing the Mueller formalism is essential in exploring the pathway complexity due to the high anisotropy and inhomogeneity of this aggregated system. Here we show that in addition to the conventional UV-Vis and chiroptical characterizations, following the spectral progression in linear dichroism and degree of polarization as a function of temperature can also provide essential information regarding the polymerization pathway. We explore different experimental protocols that yield targeted observables sensitive to structural variations. Despite the preliminary nature of the experimental results, we were able to observe consistent spectral progressions identifying the transition from bundles to tubular aggregates, which further disassemble to monomeric assembly. With this Chapter, we aim at expanding the efficacy of Mueller polarimetry to new regimes providing essential information that chemists seek for exploring the aggregation pathway complexity.

5.1 Introduction

The emerging field of supramolecular polymerization for functional materials requires the knowledge of molecular packing in the microscopic regime, from the initial nucleation to the elongation process giving rise to higher-order aggregates.[265–269] Molecular assembly guided through weak non-covalent interactions form aggregate products sensitive to changes in internal and external factors such as temperature, solvent, monomeric concentration, etc.[270–272] The importance of studying the polymerization pathway combining thermodynamic and kinetic characterizations, and controlling the supramolecular polymerization is therefore essential.

Understanding the polymerization pathways is also important in modulating the nucleation and elongation stages to direct the polymerization for obtaining desired products.[273–275] These pathway complexities have been largely studied in many molecular systems, beginning with the remarkable studies by Bouman and Meijer in 1995 on the stereomutation of polythiophene derivatives.[276–278] Different theoretical models were adopted to investigate the formation mechanisms of thermodynamically stable on-pathway products, and the kinetically driven off-pathway products (Figure 5.1.b, 5.1.c).[273,278–282] These polymerization pathway models have been developed based on the analysis of temperature-dependent spectral variations in absorption and circular dichroism which are sensitive to structural variations accompanied by optical, electron or atomic force (AFM) microscopy.[274,283,284] For small aggregates or oligomers showing significantly less linear anisotropy and depolarization of optical signals, these methods are efficient in providing the essential information on structural variations. However, for larger fibre-like super-helical structures like C8O3 aggregates, performing a full-polarimetric characterization together with the temperature-dependent spectral variations is necessary to explain the polymerization pathway. In this regard, using Mueller polarimetry as a characterizing technique is advantageous where artifact-free signals can be monitored throughout the aggregation stages. Moreover, it can provide insights on the chiral amplification and chirality transfer as the system evolves along its polymerization pathway.

In this Chapter, we employ Mueller polarimetry and monitor the disassembly of bundled C8O3 aggregates in film by repeated heating-cooling cycles, where the polymeric matrix reduces the diffusion of aggregates when the temperature is lowered. Reducing diffusion is crucial, especially when following the Mueller matrix calculations because of the long measurement timeframe (20-30 min for one Mueller matrix). For such long measurements, the

inhomogeneity of the sample could introduce errors in the analysis by probing multiple species during a single measurement due to diffusion. To better understand the pathway complexity in aggregation, we first discuss some of the recent experimental and theoretical studies performed on various supramolecular systems.

5.2 Molecular aggregation and pathway complexity

5.2.1 Hierarchical polymerization pathway

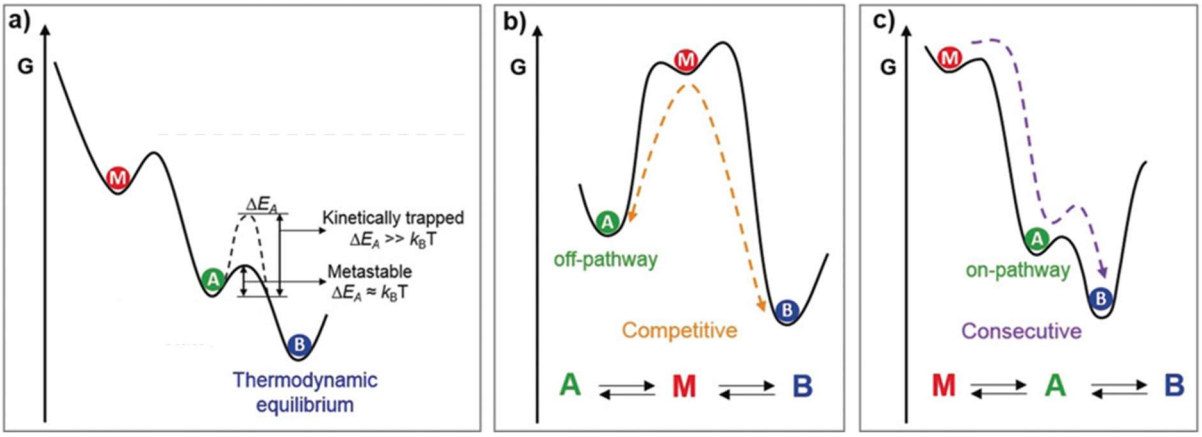

Figure 5.1: *Illustration showing pathway complexity in supramolecular polymerization summarized from the literature. Energy landscape for the polymerization of monomer (M) giving rise to a) kinetic or metastable (A) and thermodynamic (B) products, b) off-pathway product (A) in competitive polymerization between products (A) and (B), c) on-pathway product (A) in a consecutive polymerization process eventually ending with product B. Here,* ΔE_A *in (a) is the activation energy required for the system to move from structure A to B. T is temperature and* K_B *is Boltzmann constant. The energy barrier determines if the structure is kinetically trapped or corresponds to a metastable product. Adapted with permission from Ref*[285].

The weak inter- and intramolecular non-covalent interactions in molecular species can guide a system to polymerize into structures with different energetic minima.[273,283,285] The reversibility of these interactions is therefore an advantage in manipulating the aggregate species to drive them into specific energetic minima. Studying the pathway complexities is highly crucial in this regard. Accordingly, a whole body of research is directed to explore the aggregation pathways with specific concepts brought forward to classify aggregated products according to their kinetic, metastable, or thermodynamic nature (Figure 5.2.1.a), and pathways described as hierarchical, consecutive, competitive, etc (Figure 5.1).[285,286] Studying the

aggregation pathways and associating them with such pathway models and concepts provides accurate insights into modulating the structural features for desired applications. In this Section, we briefly discuss the different aggregation pathways established in the literature that are essential in understanding the experimental results of this Chapter.

Among the wide classes of polymerization pathways, the consecutive supramolecular polymerization process goes through multiple stages of aggregation, where the individual species are formed through structural re-arrangements or the formation of higher ordered structures of their preceding species in the pathway. The latter polymerization pathway is also termed hierarchical, where every stage of polymerization is an advanced macroscopic organization of its precedent structural form forms (A and B in Figure 5.1.c). In contrast, a competitive pathway involves the competition for monomers between different aggregate forms (A and B in Figure 5.1.b). In such polymerization pathways, the species are interconvertible only through the disassembly of aggregates.[287–289]

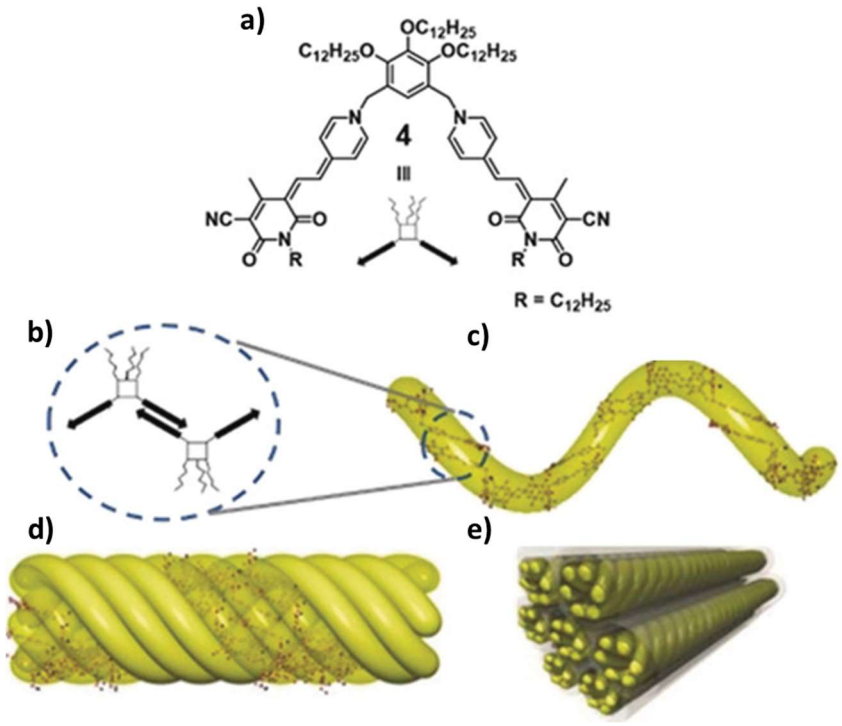

Figure 5.2: *Chemical structure of merocyanine dye (a). The arrangement of molecules in a dimer (b), that aggregates into helical fibril (c), that further form rod-like aggregates (d). These structures eventually bundles to forms hexagonal columns (e). Adapted with permission from Ref*[290].

A well-known example of consecutive aggregation pathway is the hierarchical formation of merocyanine aggregates.[290,291] This cyanine dye initially form an antiparallel dimer, which aggregates to form helical fibrils that further aggregates to densely packed rods as shown in Figure 5.2. These structural formations are monitored through UV-Vis, and CD spectroscopy, and their handedness analysed through AFM images. A similar consecutive aggregation pathway was identified in V-shaped azobenzene-based molecules by Yagai and co-workers.[292] These structures initially form H-type nano-toroids through H-bonding, which further aggregate to form chiral nanotubes through π-stacking. Eventually, these chiral nanotubes aggregate into supercoiled chiral double helices (Figure 5.3). Here again, the characterization techniques employed involve absorption and CD spectroscopy, similar to the case of merocyanine aggregation.

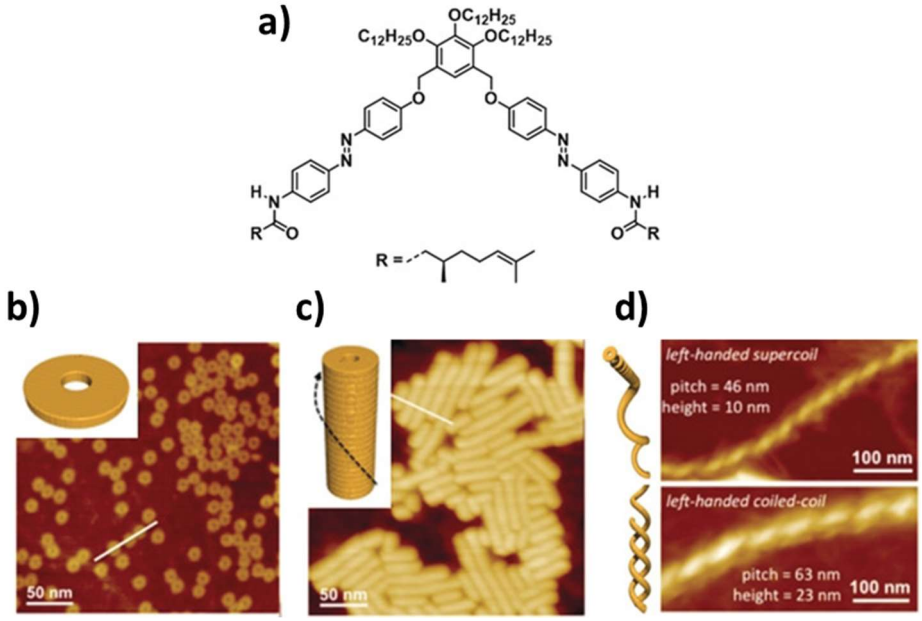

Figure 5.3: *a) Chemical structure of azobenzene based chromophore that initially aggregates into nanotoroids (b), and further into nanotubes (c). These nanotubes further aggregate into helical single (d) and double supercoils (e). The structures are analysed through AFM images. Adapted with permission from Ref [292].*

5.2.2 Pathway complexity analysis using spectroscopy

Spectroscopy has been a great tool in supramolecular chemistry since structural modifications can be correlated with spectral variations. The UV-Vis spectroscopy thus probes energetic variations through which the different stages of aggregation can be conceived. Additionally, the structural chirality and handedness can be determined through chiroptical

spectroscopy. In addition, optical, electronic (SEM, TEM), and atomic force microscopy (AFM) are combined to obtain morphological details of the aggregates.

Heating a supramolecular structure to reach monomeric form and subsequently cooling down the sample with precise control on the rate of cooling helps in distinguishing thermodynamic and kinetic aggregate products whenever the structural formation of different species is sensitive enough to the cooling rates. This analysis is achieved by consistently monitoring the spectral evolution of the sample for different cooling rates. Establishing kinetic and thermodynamic control of the products helped in determining the pathway models for various supramolecular polymers. Meijer and co-workers explored the pathway complexity in the polymerization of oligo(p-phenylenevinylene) (OPVs) and developed various mathematical models to describe one-dimensional polymerization.[273,293] These models include isodesmic, cooperative, and anti-cooperative, defined depending on the energetics of nucleation and elongation processes (Figure 5.4).[281,294,295] Among these pathway models, a polymerization process is termed isodesmic if the binding constant is fixed throughout the polymerization.[279,293] On the other hand, if the nucleation is dis-favoured, it is termed cooperative, and if it is favoured, the polymerization is termed anti-cooperative (Figure 5.4).[296–299] These pathway models have turned important for the community, helping one to characterize the monomeric interactions in the polymerization process (discussed in Section 5.2.1), which has been an essential addition to the development of the field of supramolecular chemistry.

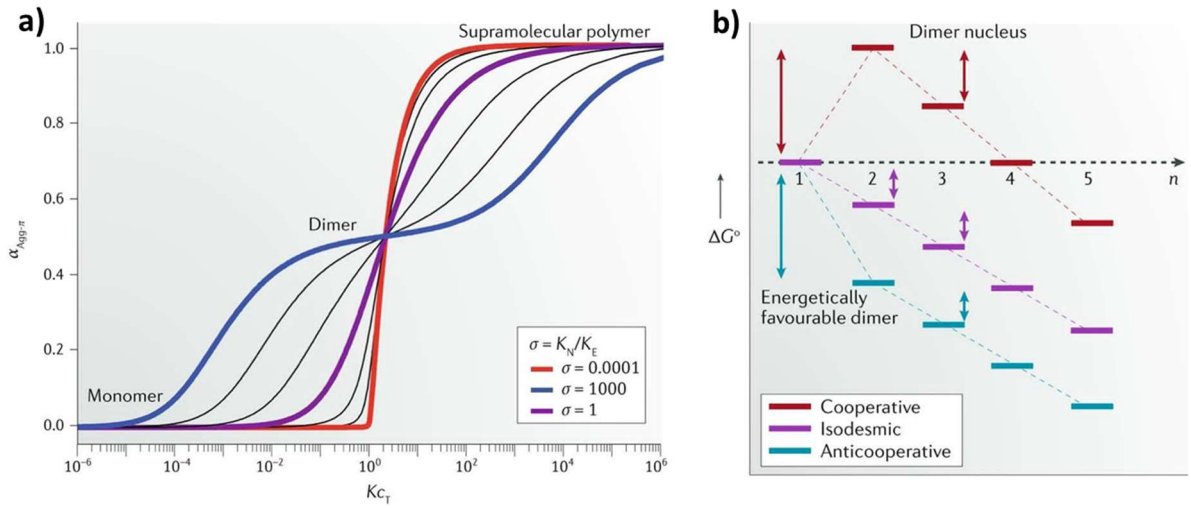

Figure 5.4: *Pathway models such as cooperative, isodesmic and anti-cooperative based on the energetics of nucleation and elongation during polymerization. a) Fraction of aggregates ($\alpha_{Agg-\pi}$) as a function of normalized concentration (K_{C_T}) for different σ values. Here, σ is evaluated as the ratio of nucleation constant (K_N) to elongation constant (K_E). (b) Energy*

(ΔG_0) diagram of supramolecular polymerization as a function of the number of molecules (n) in the aggregate, identifying the cooperative, isodesmic and anti-cooperative polymerization mechanisms. Adapted with permission from Ref [294].

In this Chapter, we aim at studying the dis-assembly pathway of C8O3 aggregates implementing the literature understanding of pathway complexity discussed in this Section. We aim at identifying the different stages of aggregation, and studying the de-polymerization mechanisms at play together with the chirality transfer processes occurring when the system evolves through these different aggregation stages.

5.3 Aggregation pathway of C8O3

Exploring the pathway complexity in aggregates of C8O3 is not straightforward with the conventional methods due to their multi-dimensional anisotropic nature, as previously discussed in Chapters 3 and 4. The aggregation process is instantaneous in solution where the control of different stages of the aggregates can be achieved by varying the ratio of NaOH to the monomeric solution.[300] However, this method gives an averaged result of multiple species in the solution, preventing us from the possibility to probe an accurate aggregation pathway (Figure 5.5). Therefore, temperature-controlled experimental protocols probing the evolution of the spectral profile of various electronic transitions are necessary. However, performing a rate-controlled experiment in the solution phase is not very convenient for Mueller polarimetry since the protocol requires reduced diffusion of the anisotropic structures throughout the acquisition time. Further down in this Chapter, we will explain in detail the experimental protocols using Mueller polarimetry for monitoring the dis-assembly pathway of bundled C8O3 aggregate.

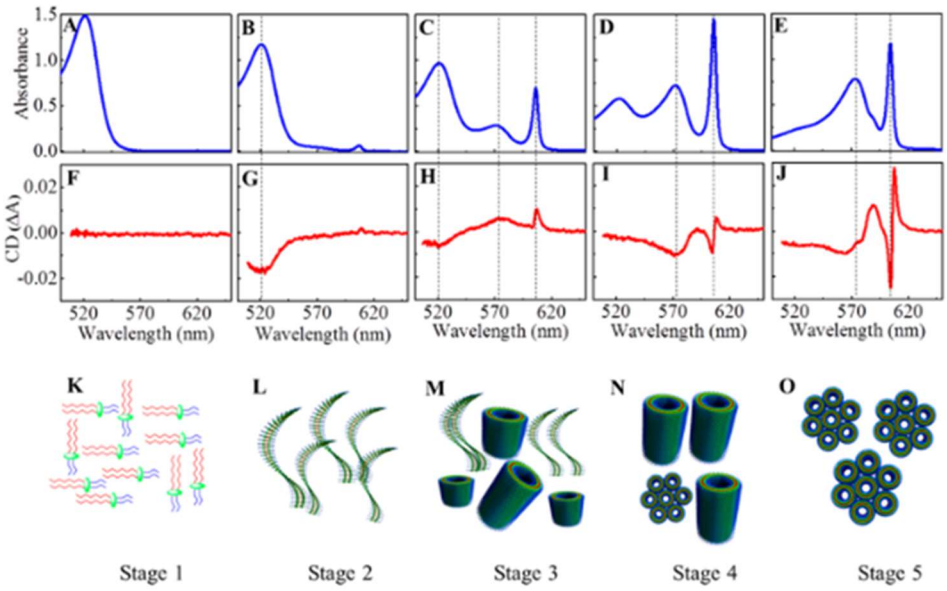

Figure 5.5: *Absorption (A-E) and CD (F-J) spectra through the hierarchical aggregation stages of C8O3 molecules (K-O). Adapted with permission from Ref*[300].

5.4 Experimental protocol for monitoring C8O3 disassembly

The C8O3 aggregate films were prepared as discussed in Section 2.2 of Chapter 2. The samples were characterized using the Mueller polarimetric method detailed in Chapter 2. Before annealing the sample, we perform a transmission Mueller measurement to identify the presence of bundled aggregate. To study the pathway of aggregation, we heat the sample through the temperature range from 30°C to 120°C with a step of 5°C. We used two methods to heat the sample; one with the use of a heating plate, and the other with the help of an oven (from Carbolite Gero). In our preliminary studies, we learned that oven-based heating yields more precise spectral progression due to uniform heating and better control of temperature, whereas using a heating plate could create a gradient of temperature in the film leading to an averaged result along the pathlength of the light beam. Therefore, we decided to use the oven-based heating results in this Chapter for all our analysis.

For every increase in the temperature, we wait for the heating setup to reach the target temperature. Once the temperature is stabilized, the sample is placed inside to heat for 10 min. After heating, the system is allowed to cool down to room temperature naturally. Later, the sample is fixed to the Mueller setup for transmission measurements. This heating-cooling cycles is repeated for every temperature from 30°C to 120°C. Here, we avoid using microscopic

objectives but reduce the probing area by using an aperture ($\sim 0.1 - 0.2\ cm$). Avoiding the microscopes allows us to reduce the possible errors occurring due to the mechanical relaxation of the objectives causing misalignment during such a long experimental protocol.

5.5 Spectral progression in the ground state

5.5.1 Temperature-dependent absorption spectra

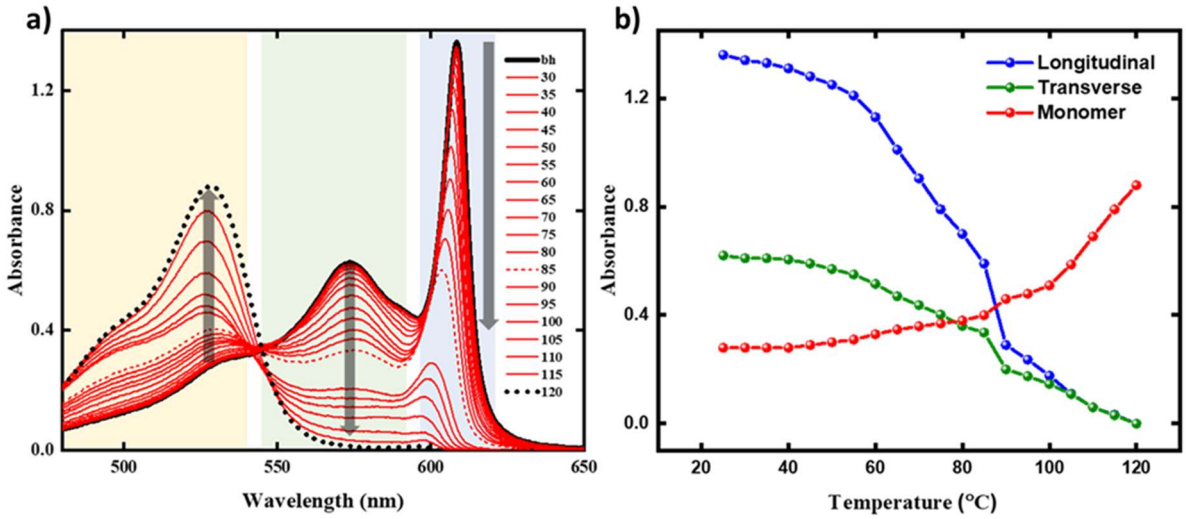

Figure 5.6: *a) Absorption spectrum of C8O3 aggregate film monitored through the temperatures from 30°C to 120°C, b) evolution of the absorbance associated with the longitudinal exciton (blue region around 608 nm), the transverse exciton at 576 nm (green region), and the monomeric transition at 528 nm (yellow region). The solid black curve (bh) in (a) represents the absorption spectra before heating the sample.*

The evolution of absorption spectra of the bundled aggregates is studied throughout the heating process (Figure 5.6). Before heating (black trace), the main peaks in the absorption spectra are at 608 nm, 578 nm, and 532 nm, corresponding to the longitudinal exciton, the transverse exciton, and the residual monomers, respectively (Figure 5.6.a). As we heat the sample, the absorbance at the transverse and the longitudinal peaks reduces, while an increase in absorbance is seen near the monomer. This shows that the concentration of aggregate is reducing along with an increase in the concentration of monomer as the temperature increases. One interesting feature observed is that the rate of evolution of longitudinal absorbance is much faster than the transverse one, while the rise of absorbance of the monomer is closely consistent with the decrease in the absorbance of the transverse exciton (Figure 5.6.b). This suggests that the evolution paths differ in the initial stages for longitudinal and transverse exciton. This

difference might have originated due to the difference in the spectral features between bundles and tubular aggregates where the major spectral variation occurs near the longitudinal absorption (see Figure 3.4 of Chapter 3). Therefore, this difference in the rate of spectral evolution can be associated with the disassembling of bundles into tubular aggregates before disassembling into monomers. In addition, it is important to note that the spectra show an increasing blue shift (a difference of 11 nm) only at the longitudinal transition. This spectral shift is a strong indication of changes in exciton coherence length, where an increase in the blue shift for a J-aggregate suggests a reduction in the coherence length of the aggregate (see Section 1.5.3 of Chapter 1). This feature again reveals that the longitudinal exciton is undergoing disassembly initially to tubular structures and eventually to monomeric species. Further analysis and correlation of the spectral progression with other polarimetric signatures are essential in yielding a better outlook to the analysis. These analyses are presented further in this Chapter.

5.5.2 Linear dichroism and linear birefringence

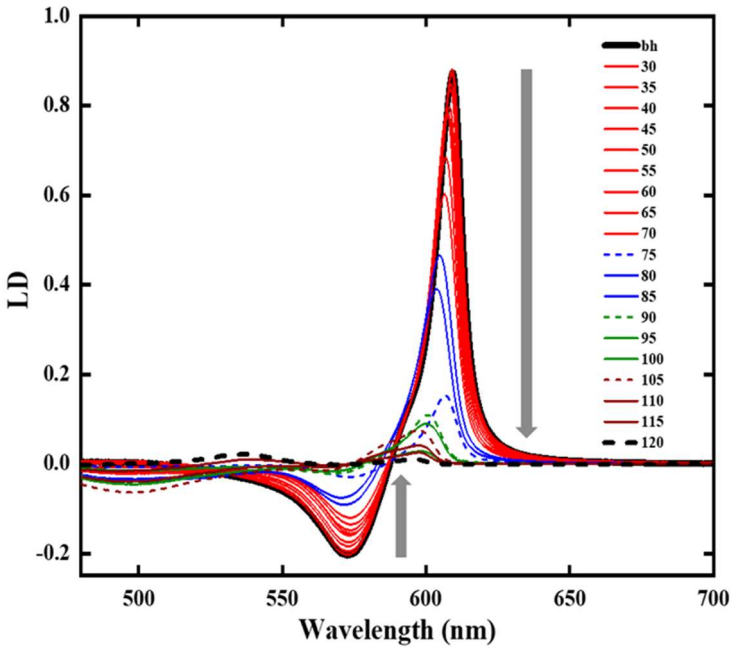

Figure 5.7: *Linear dichroism (LD) spectra of C8O3 aggregate film monitored through the temperature range from 30°C-120°C. Different colours accompany the different and drastic change in spectral features. The solid black curve (bh) represents the LD signal before heating the sample.*

The LD profile in Figure 5.7, which reveals the anisotropic absorption in the ground state, shows that the LD at 610 nm and 580 nm decreases in magnitude with the increase in

temperature. Here again, we observe spectral shifts for the longitudinal transition (similar to the absorption spectra), indicating the reduction of exciton coherence length in the molecular aggregate. In addition, it is interesting to note the emergence of a small LD signal around 500 nm, while no signal is observed at 532 nm, where the monomer absorbs. This spectral feature suggests the formation of an anisotropic assembly of monomers when the tubular aggregate disassembles. The origin of this LD signal with a blue shift compared to the monomeric absorption peak suggests an H-type molecular interaction in the assembly (Section 1.5.3 of Chapter 1). Before concluding on this aspect, further studies are required to clarify the origin of this spectral feature.

The LD signal eventually disappears at high temperatures, while a small LD signal appears near the monomeric absorption maximum. This feature traces back to the LD signal observed for the monomeric assembly at the initial stages of aggregation in solution, as reported in ref [300] (aggregation stage in Figure 5.5.L). Although the spectral evolution provides an overall picture of the disassembling molecular aggregates, the signal evolution shows inconsistency (drastic difference in signal intensity and shift in the crossover) for measurements at certain temperatures (from 75°C). It is not clear for the moment if this spectral variation is due to structural modifications or experimental errors. This inconsistent spectral progression might have occurred because of small spatial changes in the probing region due to the removal of the sample from the experimental setup for heating. It can also occur due to changes in the spatial orientation of aggregates because of thermal motion changing the overall LD signal. We will discuss further in this Chapter about the possible improvements that could help in resolving these issues to obtain more reliable results.

5.5.3 Evolution of the ground state chirality

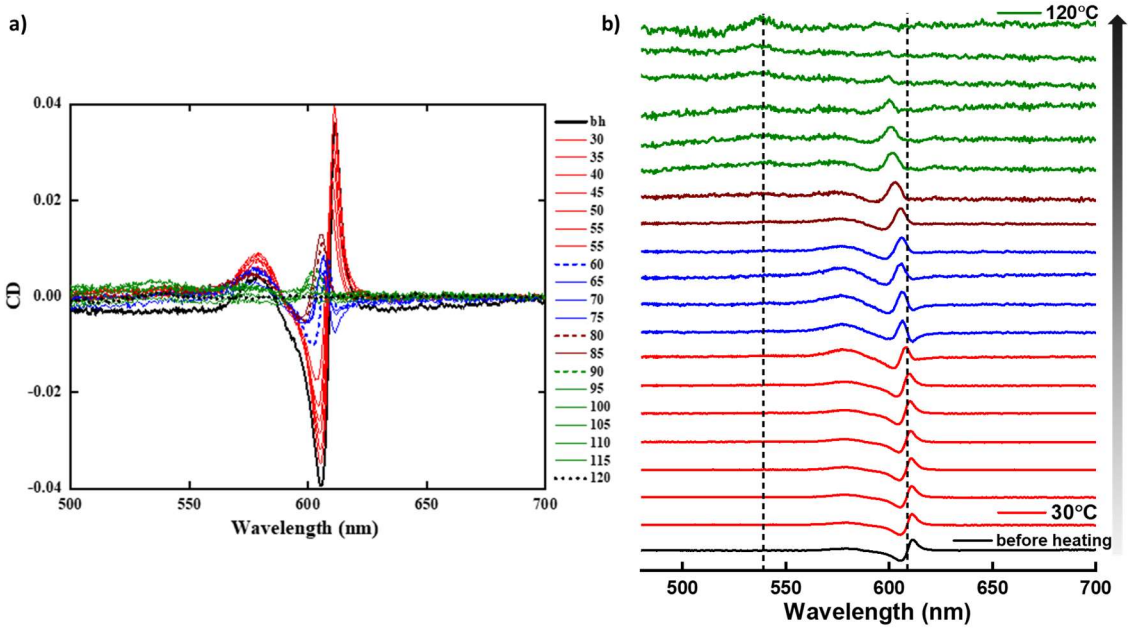

Figure 5.8: *Circular dichroism (CD) spectra of C8O3 aggregate film showing differences in signal strength (a), and (b) spectral variations for temperatures increasing from 30°C upto 120°C. Different colours represent differences in the spectral features. The solid black curve (bh) represents the CD signal before heating the sample. The dotted line at 608 nm represents the bisignation for the CD signal before heating, whereas dotted line at 536 nm monitors the evolution of the CD signal near the monomeric absorption.*

The chiral signatures monitored using the CD spectra show remarkable features when heating the sample with bundled aggregates (Figure 5.8). The variation in CD values and the evolution of spectral shifts around 610 nm can be observed in Figure 5.8.a and Figure 5.8.b, respectively. It is interesting to note that the bisignate CD signal retains its nature for a large range of temperatures (until 85°C) before evolving to monosignate peak (green curves). This bisignate CD signal is identified to originate from bundled aggregate, whereas the monosignation originates from tubular aggregates (Section 3.4.1 of Chapter 3). The spectra also undergo a small blue shift of 1 nm for the crossover of bisignation in red curves compared with the CD signal before heating (black). Moreover, the monosignate signals (green) show a minimum of 8 nm shift between crossover in the black curve and peak maxima of the monosignate signal at 90 °C. This indicates that the structure remains bundled for a range of temperatures (until 85°C), but undergoes a reduction in the exciton coherence length (Section 1.5.3 of Chapter 1).

Furthermore, the signal shows an interesting feature of reversal in the CD signal (blue curves), before the spectra change their profiles into a monosignate peak. This surprising observation of reversal of CD signal is verified through repeated experiments. However, the origin of this chiral signature is currently unclear. We suspect that the reversal of the CD signal originates from the phase change of the polymer as it goes through its glass transition temperature, $T_g \sim 67 - 98°C$. Further studies are required to verify if the spectral variation is induced due to this phase change of the polymeric matrix or if it is an intrinsic aggregation stage that the system goes through during the disassembly pathway. Eventually, the chiral signature of the aggregate disappears, along with an evolution of a small CD signal near the monomeric absorption regime (at 536 nm). This feature is consistent with the evolution of small LD signals observed at high temperatures in Figure 5.7. Herein, it is important to note that the positive CD couplet (positive followed by negative bisignate CD) of the bundled aggregate changes into a positive monosignate signal. This chirality transfer between tubular and bundled aggregates is fascinating as it provides insights into the nature of the chiral coupling between tubular aggregates during bundle formation. Here, the signal evolution suggests a transition from a P-bundle to an M-tubular aggregate. A closely-related reversal in chiral handedness has been identified in OPE derivatives when moving from chiral helices (M-helix) to super-helix (P-super-helix) structure.[289] Although we observe a similar transition, it is essential to combine these results with theoretical studies to clarify the precise mechanisms at play.

5.5.4 Temperature-dependence of the degree of polarization

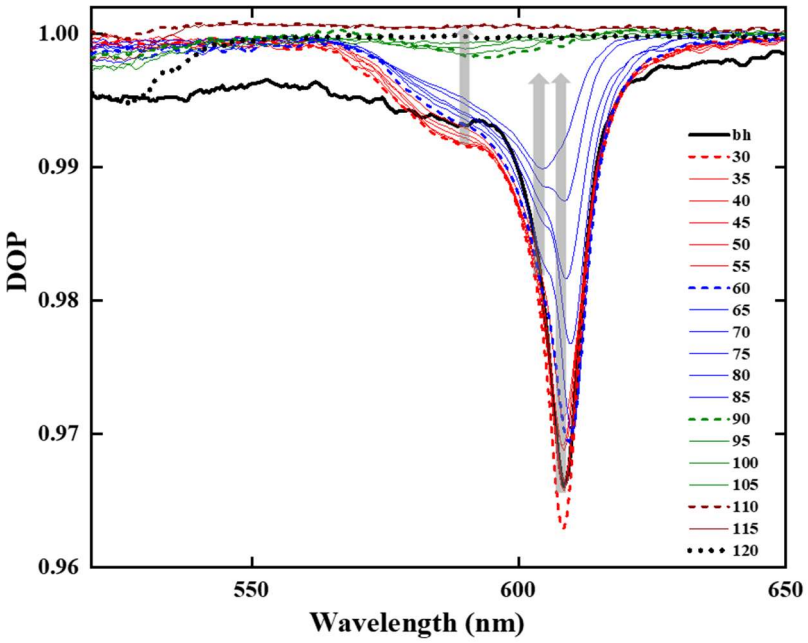

Figure 5.9: *Evolution of degree of polarization (DOP) through the heating-cooling cycles. Different colours represent the drastic spectral variation compared with the preceding signals. The solid black curve (bh) corresponds to the DOP signal before heating the sample.*

Apart from the linear and circular anisotropic information provided by the Mueller formalism, the degree of polarization, often overlooked, can also provide important information on the structural variations. As shown in Figure 5.9, the highly depolarized signal at 608 nm corresponding to the longitudinal exciton becomes more polarized with the increase in temperature. This feature is again a clear indication of the reduction in the size of the aggregates since large structures cause high depolarization through light scattering. It is more interesting to note that as the temperature increases, the DOP peak shows a splitting around 608 nm, and the rate of evolution of the two peaks differs. These spectral variations are consistent with the range of temperatures over which the reversal in the CD signal was observed (blue curves in Figure 5.8). Here we suspect that this splitting of the spectra might have occurred due to the coexistence of tubular and bundled structures. However, it is important to identify the origin of the reversed CD signal in order to correlate and confirm this analysis.

At higher temperatures, the DOP increases to higher values when the structure changes into tubular aggregates identified as green curves. These are the temperatures when the CD signals became monosignate in Figure 5.8. Eventually, we obtain much less depolarization from the aggregate, but, a small increase in the depolarization near the monomeric absorption

region is observed. This evolution of depolarization signal is consistent with the monomeric assembly formation identified in other polarimetric signals (LD, CD).

Herein, we emphasize that apart from chiroptical characterization, depolarization signals also display important information regarding the structural modifications. This again demonstrates the importance of employing Mueller polarimetry to monitor structural modifications, where the combination of different polarimetric observables provides multiple polarization-dependent signals sensitive to structural perturbations.

5.6 Drive towards aggregation

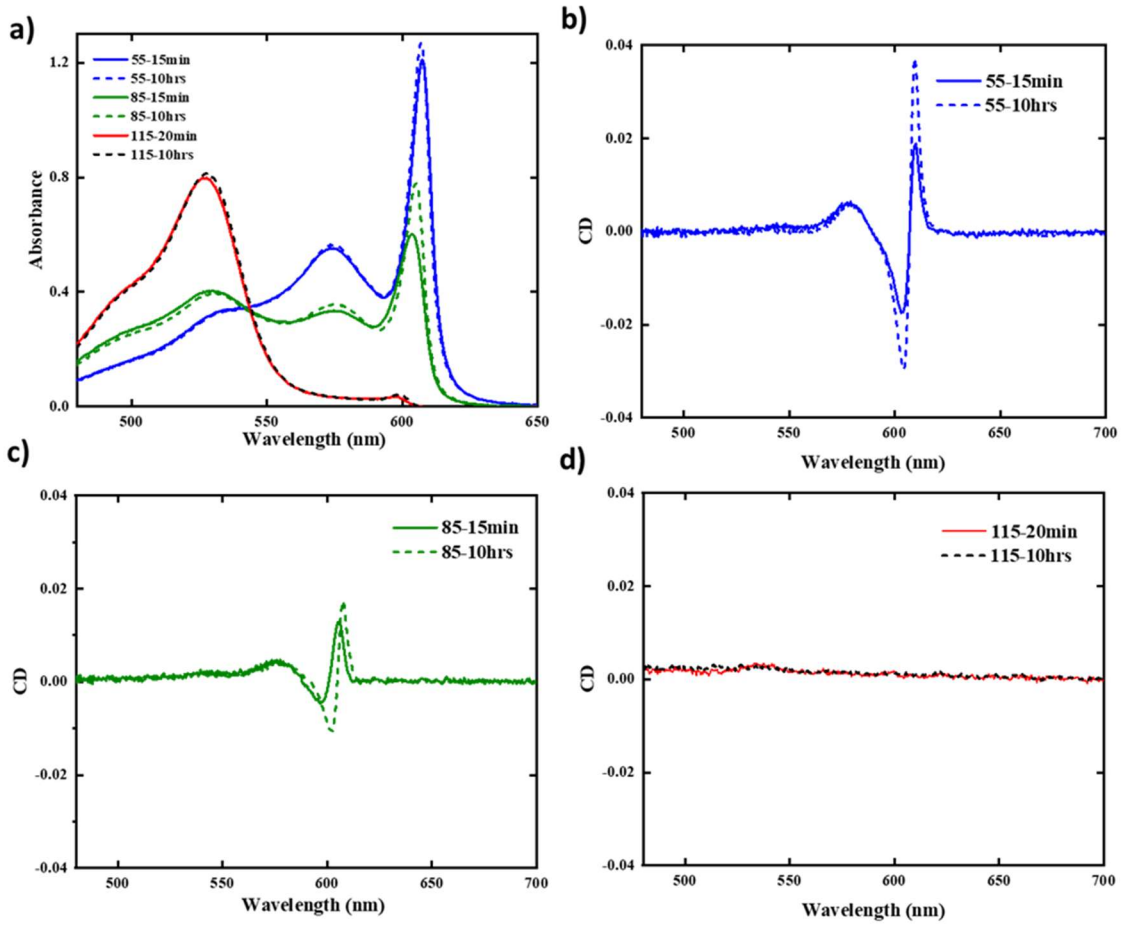

Figure 5.10: *Absorption (a) and CD (b, c, d) spectra of C8O3 aggregate film monitored over a time difference of 10-20 min and 10 hr of cooling after heating the film to 55°C, 85°C and 115°C.*

We then analysed the evolution of the system when allowed to relax for a long time after heating the sample. For the preceding results, the samples were measured for pathway analysis roughly 15-20 min after cooling down to room temperature. Playing with time at this

stage will allow us to check whether the system keeps evolving if cooled for a longer time. Therefore, we measured the sample at the same probing region after 15-20 min of cooling, and after 10 hrs of cooling. As shown in Figure 5.10, we observe that the system evolves towards the bundled state with a strong chiral signature (large CD signals) and an increase in absorbance near the transverse and longitudinal transitions when the system is heated to 55°C and 85°C, and allowed to cool for 10 hrs. This tendency to lead the system back into aggregates with large CD values is observed only in Figure 5.10.b and 5.10.c. This shows that the drive towards aggregation occurs only when the system retains fragments of chiral species (Figure 5.10.a, 5.10.b, 5.10.c). However, once the system is disassembled into monomeric form, it shows no tendency to move towards an aggregated phase as seen from the overlapping CD signals in Figure 5.10.d for both 20 min and 10 hrs of cooling.

5.7 Spectral evolution: reaching the steady state

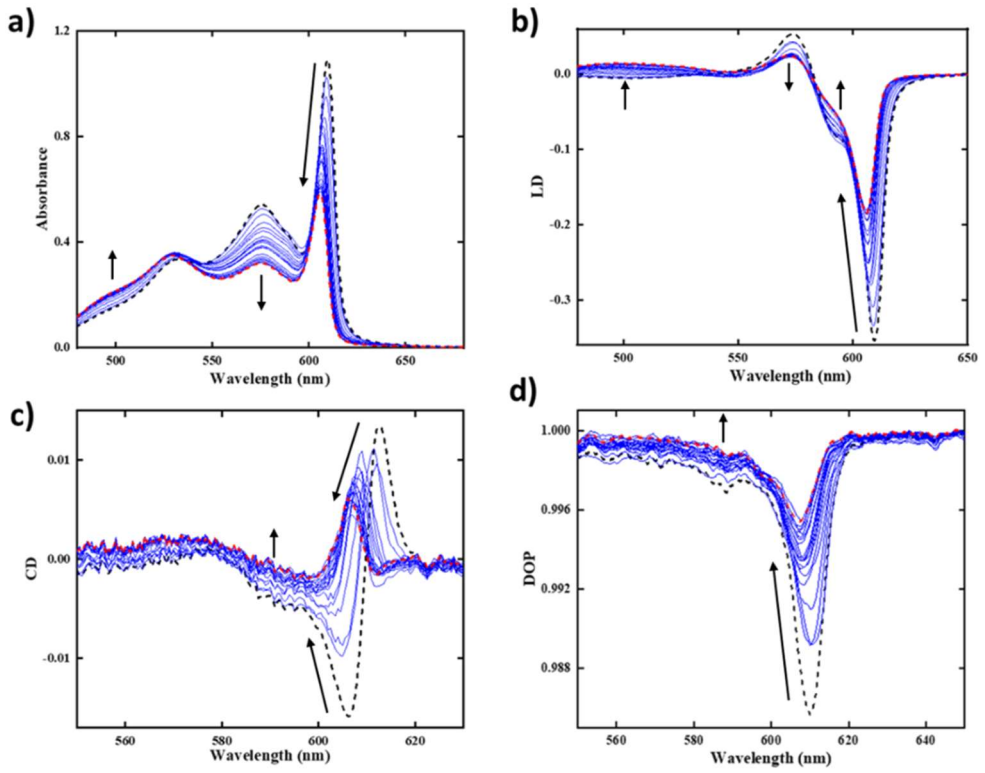

Figure 5.11: *a) Absorption, b) LD, c) CD and d) DOP spectra of C8O3 aggregate film heated at 50°, and monitored the spectral variation as the sample evolves to reach the steady state.*

The results discussed in Section 5.6 led us to explore the evolution of the aggregate system under constant heating to reach the steady state. To monitor the spectral progression of the system to reach a thermodynamic equilibrium (see Figure 5.1.a), we heated the sample at a

constant temperature of 50°. Here again, before measuring the sample, the system is brought to room temperature after heating for 5 min for the initial 11 measurements and 10 min for the subsequent measurements. This change in timeframe is adopted due to the fast structural variations in the initial stages and slower variations as the structure is more perturbed. The spectral progressions obtained in this procedure are presented in Figure 5.11. The evolution of the system is consistent with the previous results, where the absorbance for the transitions corresponding to the aggregate reduces along with an increase in absorbance for the monomer. Additionally, the peak at 610 nm shows blue shifts, while the peak at 576 nm shows no spectral shift, similar to the observation made in Section 5.5. The LD profile also shows consistent evolution in agreement with the absorption profile. Interestingly, we observe the progressive evolution of the peak at 590 nm in the LD profile, which was not clearly observed when the temperature was increased in Section 5.5.

A more interesting spectral progression is observed in the CD signal (Figure 5.11.c), where the bisignate CD profile changes to a monosignate profile. We relate this change to the transition from bundled to tubular aggregates. In addition, the signal undergoes a blue shift as similarly observed in section 5.3.3, which could be associated with the reduction in the exciton coherence length (see Section 1.5.3 of Chapter 1). Furthermore, the emergence of a small negative signal is observed at 611 nm. This feature of the signal looks similar to the reversal of CD discussed in Section 5.5.3, however, its precise origin is currently unclear.

The progression of DOP is also remarkable with its high sensitivity to structural changes. It subsequently shows spectral shifts and small splitting of the peak at 608 nm as previously observed. It is also important to note here that the signals saturate with identifying the presence of tubular aggregates, which conveys the idea that the breaking temperature of bundles is lower than the tubular aggregate. This difference in structural strength is characteristic of the hierarchical aggregation pathway discussed in Section 5.2.1, where the initial aggregation stages undergo strong interaction, and the strength diminishes for the subsequent stages reaching the energetic minima at the thermodynamic equilibrium (see energy landscape in Figure 5.1.a).

5.8 Deciphering the disassembly pathway using polarimetric signals

Following the spectral progressions discussed in Sections 5.5 and 5.7, herein, we derive the disassembly pathway of the chiral bundled C803 aggregate, utilizing all the polarimetric information provided by the Mueller formalism. The spectral evolution suggests a hierarchical or consecutive pathway for the aggregate similar to the examples discussed in Section 5.2. This pathway characterized from the aggregate film shows similarity to that identified in the solution state (Section 5.3).[300] However, with the protocols employed throughout this Chapter, we obtained more information on the growth of the aggregates along with the spectral features of individual aggregation stages.

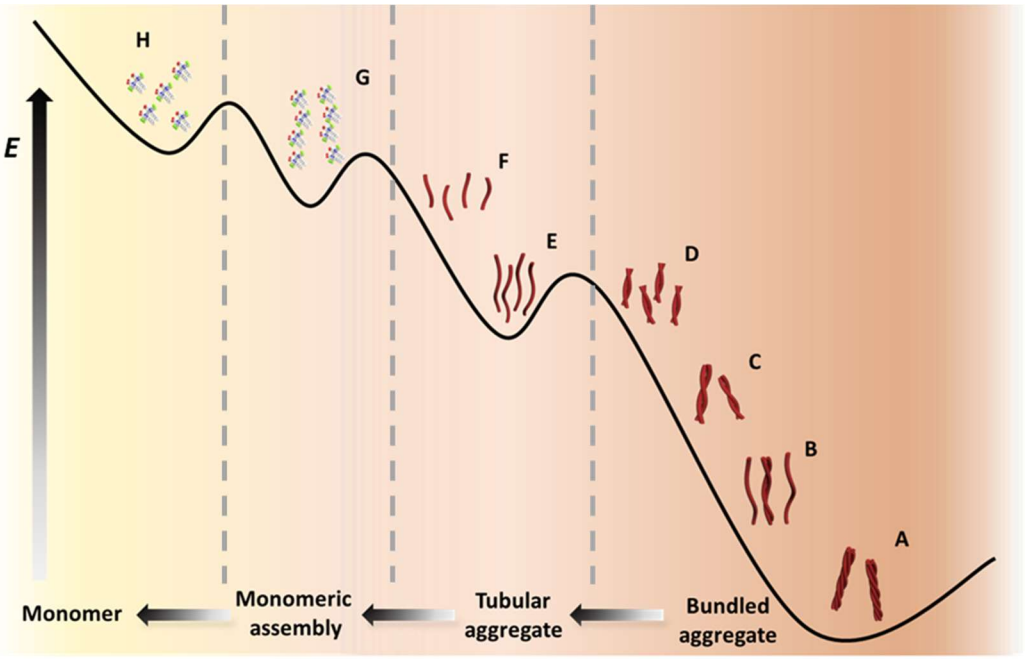

Figure 5.12: *Graphical illustration showing the energy landscape for the different aggregation stages of C8O3 drawn with insights from absorption, CD, LD, and DOP spectral progressions discussed in Sections 5.5 and 5.7.*

The energetic landscape for different aggregation stages is presented in Figure 5.12. The blue shifts observed near the longitudinal transition in the absorption, LD, and CD spectra, along with reducing CD signal can be interpreted as the manifestation of the disassembly of bundles, that reduces the exciton coherence length. In addition, the splitting of DOP spectra suggests the coexistence of tubular and bundled aggregates. These spectral features are interpreted as the aggregation stages A and B in Figure 5.12.

Later the system breaks into smaller fragments of bundles, as indicated by the bisignate profile of the CD signal which is retained for a long time along with the reduction of the signal strength in the LD profile. These spectral features are identified as stages C and D in Figure 5.12. The spectra eventually become monosignate identifying the transition into tubular aggregates (Figure 5.12.E, 5.12.F), which undergo further fragmentation to eventually become monomeric assemblies (Figure 5.12.G) and finally into monomers (Figure 5.12.H).

The origin of the intermediate aggregation stages represented as blue curves in the CD spectra (Figure 5.8) remain unclear. Therefore the chiral nature of these structures is not taken into consideration in the energy landscape (stage B). There exist multiple reasons for the origin of this CD signal. As discussed earlier in Section 5.5.3, this CD signal could have originated from the phase change of the polymer, inducing structural changes in the aggregate, or from modified interactions (H-type or J-type) between the longitudinal transition dipoles in the bundle (see Section 1.5.3 of Chapter 1). In addition, this CD signal may have appeared due to the heterogeneity of the sample with the presence of bundles and tubes with opposite handedness in the probing region. Further studies are therefore essential to identify the origin of these CD profiles showing a reversal in chirality. Although the spectral progression leads to identifying the major aggregation stages, this disassembly pathway might have been influenced not only by temperature but also by the changes occurring to the polymeric matrix as it goes through its glass transition temperature.

The disassembly pathway presented in this Chapter, explored using Mueller polarimetry clearly reveals the importance of multiple polarization analysis to monitor the structural evolution of complex systems such as C8O3 aggregates. Despite the reproducibility of the spectral progression in repeated studies, the current analysis suffers from the absence of precision in the control of the rate of heating and cooling. In addition, it is highly important to adapt a heating controller to the measurement set-up to prevent unwanted errors likely to emerge in the context of thermal studies (such bas change in probing region).

To study the spectral evolution of the aggregate in a more controlled manner, it is thus important to reduce the disturbance imposed on the sample and control the rate of heating and cooling with more precision to the temperature (see for instance the spectral inconsistency discussed in Section 5.5.2). This technical improvement will also allow us to study both the kinetic and thermodynamic pathway complexities of the aggregation process. To achieve this, we propose to couple the Mueller polarimetric setup with the Linkam heating stage (Linkam

94 THMS600) so that we do not have to remove the sample from the experimental setup. With this alternative addition to the experiment protocol, we aim at enhancing the precision of the spectral monitoring and thereby obtain accurate pathway analysis. This will aid in identifying and correlating the polymerization pathway to the current models established in the literature as discussed in Section 5.2.2.

5.9 Conclusions

In this Chapter, we have explored the pathway complexity of C8O3 aggregates using Mueller polarimetry by monitoring the disassembly of the bundled aggregates. Studying the pathway complexity of supramolecular aggregates helps in modulating the structures for obtaining desired properties. The conventional methods used for exploring the pathway complexities in supramolecular polymerization require rate-controlled temperature-dependent spectroscopy involving UV-Vis and chiroptical characterization. Performing similar analysis in C8O3 aggregates is highly challenging due to the high anisotropy and inhomogeneity of the sample, which demands artefact-free polarimetric analysis. Here again, Mueller polarimetry is efficient in deriving artefact-free signals and thereby helping the studies on pathway complexity. In this Chapter, we confronted the experimental protocols using Mueller polarimetry to various challenges regarding temperature-dependent characterization methods. Despite the preliminary nature of our results, this Chapter shows the efficacy of Mueller formalism in providing an ensemble of observables for characterizing supramolecular polymers that demand extreme care with spectral analysis when studying the pathway complexity. We show that, in addition to UV-Vis and CD spectroscopy, consistent and unique spectral progressions are shown by other polarimetric characterization such as LD and DOP. Accessing these signals can provide information that is otherwise hardly observed from standard UV-Vis and chiroptical analysis.

In our measurements, we monitored the evolution of bundled aggregates to monomers, which is not a single-step process, but rather goes through multiple hierarchical stages identified initially as fragments of bundles that becomes tubular structures and eventually disassemble into monomeric species. These hierarchical stages were characterized by monitoring the spectral evolution of the observables in transmission Mueller matrix, where the multiple polarimetric information are combined to draw the disassembly pathway. These analyses led us to propose a hierarchical disassembly pathway for the C8O3 bundled aggregates. We also observed an interesting behaviour of reversal of chiral signatures before

the system changes from bundled to tubular form. The origin of this phenomenon is currently not clear and obviously demands more experimental studies.

We further discussed methods to bring better precision to the spectral analysis by eliminating possible experimental errors in monitoring the disassembly pathway of C8O3 aggregates. This mainly includes adapting the experimental set-up to a temperature controller that aids in performing rate-controlled thermodynamic and kinetic experimental protocols along with reducing the potential errors due to disturbances in the sample. Once this control in the experiment is achieved, a precise understanding of the different aggregation stages and their thermodynamic and kinetic natures can be understood. These kinetic and thermodynamic characterizations could help in developing a polymerization pathway model specific to our system, and to quantify its energetic landscape. Moreover, the influence of the phase transition of polymer in the aggregation pathway can also be investigated from a chiroptical perspective.

Chapter 6

General conclusions and perspectives

6.1 General conclusions

Chiroptical features of supramolecular polymers form a research field that currently funnels attention in a combination of knowledge, ranging from organic synthesis to optics, combining theoretical effort with experimental endeavours, and targeting different technological and functional applications.

This thesis mainly aimed at discussing the challenges that can emerge when characterizing the photophysical properties of such supramolecular structures, in particular regarding their chiroptical signatures. The challenges fundamentally arise from the high anisotropy, sample inhomogeneity, and inner-filtering effect, generated by such complex molecular systems. This complexity induces artefacts in optical signals that must be well controlled to assess quantitatively these chiroptical features. To do so, we relied throughout this thesis on Mueller polarimetry, showing in particular, how efficient this tool is for removing artefacts and thereby accessing essential pieces of information that would hardly be observable using conventional characterization methods.

In the first chapter of this thesis, we summarized the current context and understanding of the emergence of chirality in molecular and supramolecular structures. We presented some recent theoretical and experimental developments in the field necessary to comprehend for moving forward with the other chapters of this thesis.

Chapter 2 exposed the origins of the different optical artefacts that can potentially pollute polarimetric observables, in particular, chiroptical signals. These artefacts can arise either from the inherent properties of the materials under study or from the experimental methods chosen to perform such studies. We showed in this Chapter how Mueller polarimetry allows for artefact-free characterization of complex materials and how this approach leads to extracting the intrinsic polarimetric signatures of chiral supramolecular systems.

To illustrate the efficiency of Muller polarimetry, Chapter 3 gathered our experimental results obtained for the precise characterization of the chiroptical properties of a film of bundled C8O3 aggregates. Mueller polarimetry led us to identify remarkably strong intrinsic chiroptical features associated with such complex structures and to show how they could be exploited as efficient emitters of circularly polarized light (CPL). We also discovered in this molecular system a unique signature of bisignate CPL associated with the right *vs.* left circularly polarized emission lines from two excited states emerging from the strong coupling of Frenkel excitons. Additionally, we observed a high correlation between absorption and emission dissymmetry factors that indicated that the chirally active absorption and emission processes involve the same transition on such structures. These observations and results led us to present an energy level diagram of the bundled aggregate that could correspond well to the surprising chiroptical signatures brought forward by Mueller polarimetry.

Besides analysing chiroptical observables like circular dichroism (CD)and circularly polarized luminescence (CPL), Mueller polarimetry also gives details on other polarimetric features such as linear dichroism (LD), linear birefringence (LB), circular birefringence (CB), and degree of polarization (DOP), in particular using transmission Mueller matrices. Extended to excited state polarization dynamics, Mueller polarimetry leads to extracting specific polarimetric signatures such as linearly polarized luminescence (LPL), fluorescence-detected linear dichroism (FDLD), fluorescence-detected circular dichroism (FDCD), and measuring with no ambiguity fluorescence polarizations or fluorescence anisotropies. We have observed such signatures on our bundled C8O3 aggregate systems and extended our methodology to excited state polarization analysis. These results were analysed in Chapter 4 using an original

2D-Excitation-Emission Mueller polarimetric approach. This new method, presented in the Chapter, enabled us to study the excitation-wavelength depended emission polarimetric properties of these aggregates, and to extend the energy level diagram of the aggregated system with the dipolar orientations associated with the different electronic and vibronic transitions.

Apart from this study of the polarization dynamics of supramolecular structures, we also wanted to explore the emergence, evolution, and transfer of chirality at play at the different stages of the supramolecular aggregation/polymerization process. To this aim, we investigated in Chapter 5 the disassembly pathway of our bundled C8O3 aggregates initiated by heating the sample. This investigation of temperature-dependent spectral evolution was done using transmission Mueller polarimetry. We monitored the polarimetric evolution of the various transitions that can be observed as a function of temperature in the bundled aggregate revealing that the disassembly pathway is not a single disintegrating process, but rather follows a specific hierarchical pathway. To understand the pathway complexity, we followed the evolution of the polarization signals in absorption, LD, CD, and DOP. With this method, we showed the importance of multiple polarization analyses for monitoring and characterizing the complex structural evolutions of the C8O3 aggregates.

6.2 Perspectives

At this final stage, we present a few perspectives that, in our opinion, contribute to emphasizing the relevance of Mueller polarimetry in the context of molecular science and the relevance of our C8O3 systems for chiroptical applications.

A. Mueller polarimetry on lanthanide complex: revealing chirality reversal

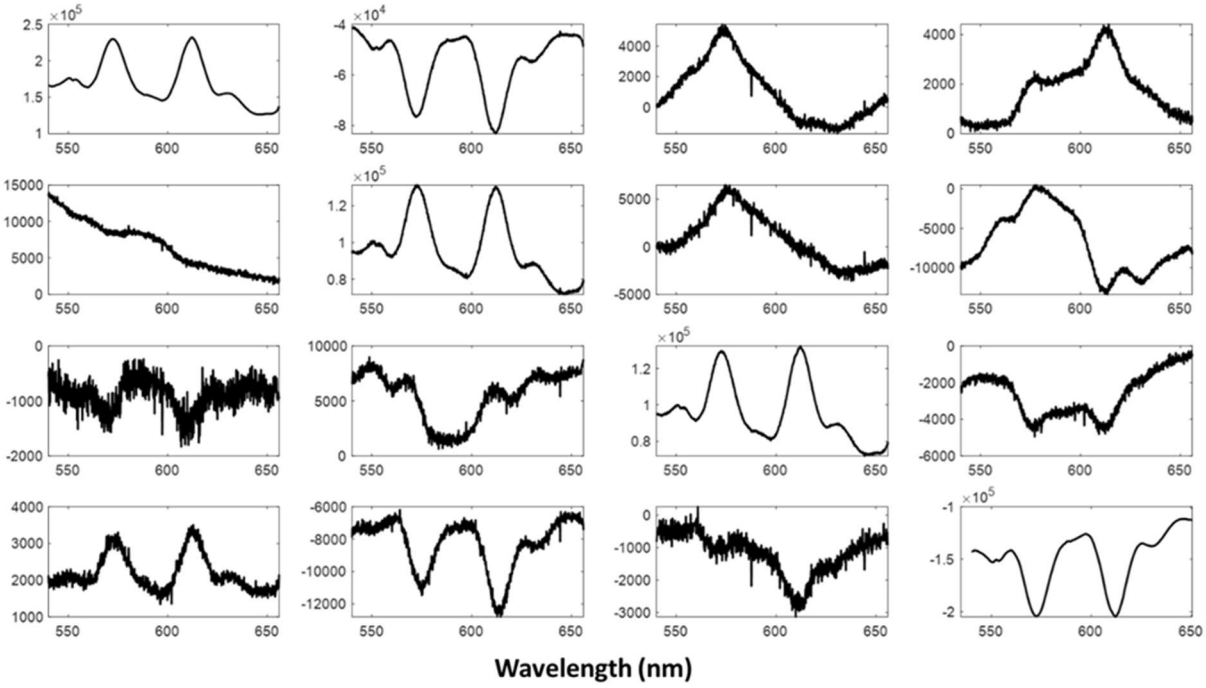

Figure 6.1: *Unnormalized emission Mueller matrix of 5mM Eu(facam)$_3$ in DMSO excited at 380 nm.*

The Mueller polarimetric setup employed for the studies gathered in this thesis was designed for characterizing molecular systems in the visible range from 400 to 800 nm. Recently, a UV-Mueller setup was developed in the laboratory to work in the UV-Vis wavelength range, starting from 300 nm. Such an extension to the UV range is very demanding within the same experimental methodologies and protocols involved with the polarization state generator (PSG) and polarization state analyzer. With these methods, we performed some preliminary studies on the Eu(Facam)$_3$ complex, which is a commercially available lanthanide complex displaying a CPL signal with large g_{lum}~-0.7 values.[301,302] Using our UV-Mueller polarimetry setup, we excited the sample at 380 nm and measured the emission Mueller matrix

(unnormalized) presented in Figure 6.1. In this unnormalized Mueller matrix, we saw an intriguing spectral signature of chirality reversal from the m_{33} element of the Mueller matrix. This matrix element, that quantifies the level of chirality preservation, is silent for C8O3 aggregates and other chiral molecules, but has been observed consistently when studying the response of van der Waals heterostructures made of transition metal dichalcogenides (TMDs) coupled to graphene.[303] In these structures, the high coherence of the so-called "valley polarization" is measured directly on a positive m_{33} coefficient. In contrast, we observed here for $Eu(facam)_3$ a reversed (negative) sign for m_{33}. This negative coefficient suggests a reversal in the chiral response for the ground and excited states. In other words, this matrix element seems to indicate that the system is most favourably excited under σ^+ circular polarization while emitting mostly σ^- circular polarization. This feature of chirality reversal is interesting by itself and clearly demands further experimental and theoretical studies (Figure 6.2).

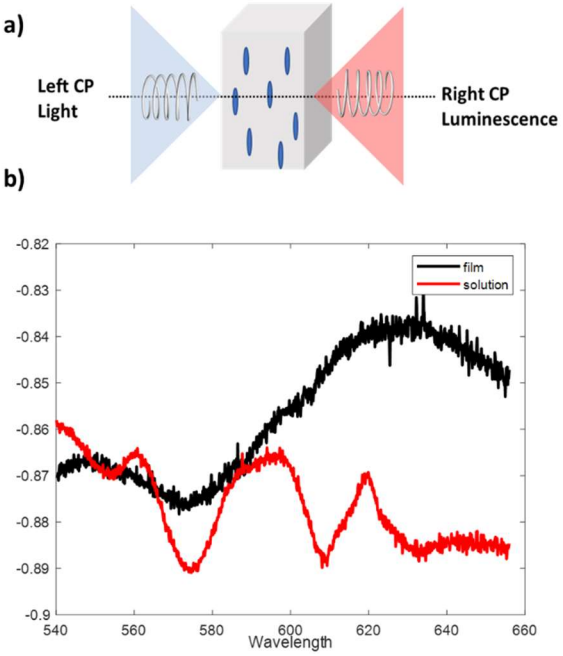

Figure 6.2: *a) Schematic showing chirality reversal with on the left-hand side, a left circularly polarized exaction, and on the right hand-side, the induced emission right circularly polarized, b) the corresponding m33 element of $Eu(facam)_3$ in DMSO (red) and in PMMA film (black).*

If such preliminary results are promising, we must however note that the CPL signals recorded in our experiments turn much lower than the signals reported in the recent literature. These literature reports however stresses that CPL activity in these complexes is extremely sensitive to the presence of water.[304,305] Since the material and the solvent we used here are hygroscopic, the influence of water molecules cannot be avoided. Hence, bringing a proper

sample preparation method by reducing the water content in the measuring sample is extremely important. Before any conclusion can be drawn regarding chirality reversal, our experiments must be carefully verified, in order to validate whether the CPL signal obtained here is intrinsic to the material or rather due to water contamination. With such experimental conditions gathered, it will become possible to start verifying and understanding the origin of chirality reversal in this material, both from chiroptical and theoretical perspectives. Since this property of chirality reversal most probably, originates from structural changes between ground and excited states, modifying the electric and magnetic dipole coupling, such studies are very interesting to push forward.

B. Enhancing CPL through light-matter strong coupling

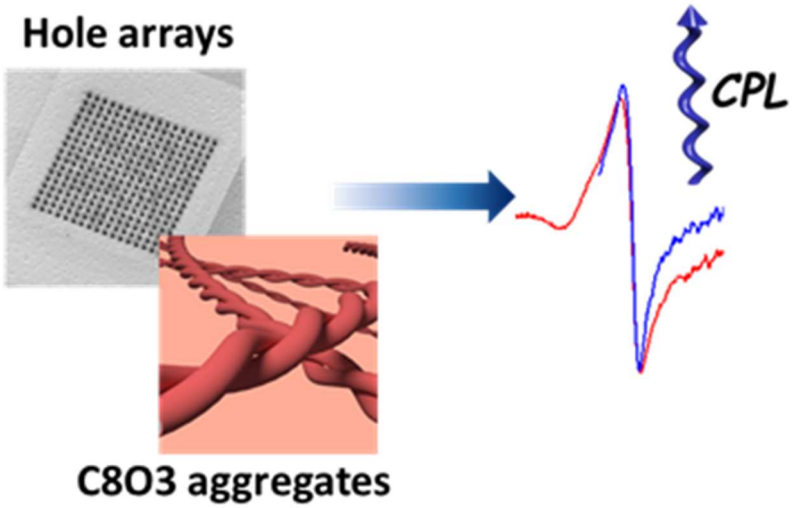

Figure 6.3: *Schematic illustrating the CPL enhancement in C8O3 aggregates through electronic strong coupling with hole arrays.*

Improving the CPL activity of materials has long been a target for advanced optoelectronic applications.[306] A wide variety of organic and inorganic materials and supramolecular structures were developed with this particular aim. But in the molecular realm, only lanthanide complexes have been shown to reach near the limits of emission dissymmetry (close to 2) as discussed in Chapter 1 and in reference [306]. Despite this asset, such complexes are of limited interest in terms of chiroptical applications because of their low quantum yield. In this respect, research interests have focused recently on bringing forward new, alternative, materials for optimized applications. In this context, light-matter strong coupling could open a promising route. Strong coupling has grown up in the past years as an efficient way for changing materials' responses.[307] It has shown a capacity to even modulate the structural properties of molecular

aggregates.[308] Recently, theoretical studies conducted by F. Spano and colleagues proposed that light-matter strong coupling can enhance the exciton coherence length by decoupling exciton-vibrational coupling to reduce disorder in the system.[309] This can give an absolute advantage of strong coupling in the field of supramolecular chirality because of the close relation between chiroptical strengths and the exciton coherence length of aggregates as discussed in Chapter 1 of the thesis. Indeed, if strong coupling enhances the exciton coherence length, an enhancement in the CPL signal in helical J-aggregates should be expected. In this regard, we initiated new studies on the phenomenon of light-matter strong coupling with C8O3 aggregates on hole arrays (Figure 6.3). These initial studies, however, faced with the fact that C8O3 aggregates have a very low structural stability once deposited on the gold film with the plasmonic hole arrays. Improved stabilization strategies are thus crucially needed. One could in this regard resort to a chemistry engineering approach with tailored changes in the aggregate chemical structure or dedicated passivation of the metal surface to reach a proper stabilization between the supramolecular film and the plasmonic cavity. In all cases, the possibility to enhance chiroptical features through light-matter strong coupling clearly shapes a new topic that will obviously be explored in the laboratory.

C. Biasing supramolecular chirality of C8O3 aggregate ensembles

As discussed in Chapter 3 of the thesis, the spontaneous symmetry breaking during the aggregation of C8O3 molecules results in an apparently racemic distribution of both P- and M-chiral bundles.[310] While we developed methods to selectively measure the individual properties of each of these enantiomers, it appears however interesting to bias the chirality of the aggregation and bundling processes so that a macroscopic phase of a given chirality could emerge from the process. This would constitute a more interesting advance for exploiting the strong chiroptical features of C8O3 bundles as efficient CPL emitters, with one helicity of light emitted from an extended area of the supramolecular film. Various methods through induced circular dichroism can be employed. We have initiated some experiments in this direction using chiral solvents for aggregation, hoping that the chirality of the solvent could stabilize one enantiomeric form of aggregation over the other. We have used chiral solvents such as Limonene and Carvone and tried to induce aggregation by the addition of water. The reduced miscibility of these solvents with water did not however yield any aggregates. Although aggregation was not achieved, we were able to induce chirality at the monomer level using Carvone as a solvent (Figure 6.4). These preliminary results and experiments should be

developed further by finding the right solvent combination that could induce aggregation and bias chiral signatures up to the bundling stage of aggregation.

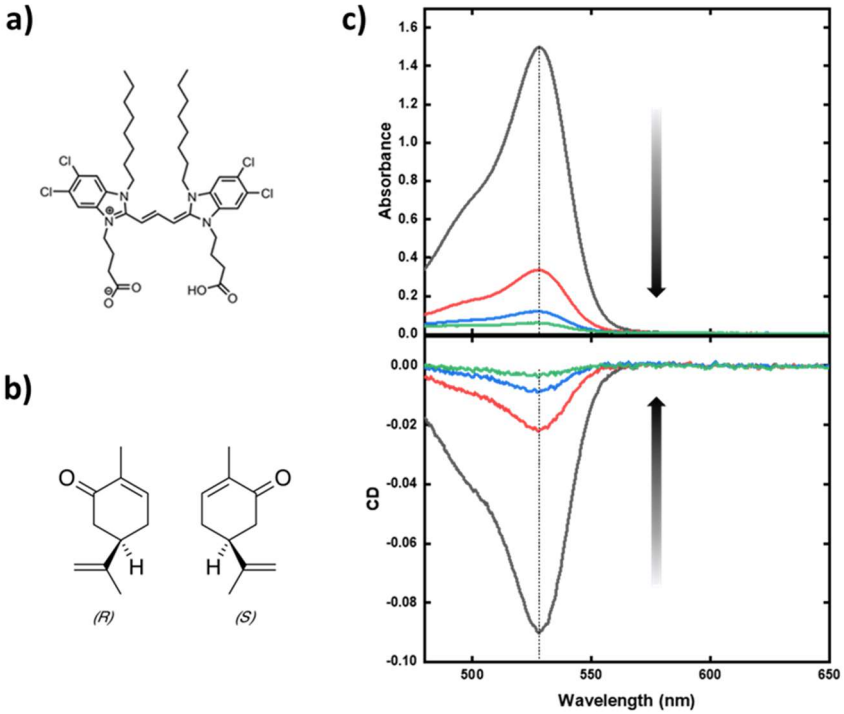

Figure 6.4: *a) Molecular structure of C8O3, and b) S(+)- and R(-)-Carvone. c) Absorption and CD spectra of C8O3 monomers of different concentration in S(+)-Carvone. The CD (g_{abs}) signal shows values ranging to a maximum of 0.95 from C8O3 monomers indicating that chirality is induced from the solvent to the C8O3 monomers.*

D. Origin and evolution of chirality in bundled C8O3 aggregates: theoretical studies

The remarkable and surprising chiroptical signatures of C8O3 aggregates form the core material of the thesis. The unique monosignate and bisignate nature of the CD signals observed for tubular and bundled aggregate, respectively, turn out to be fascinating when looking at the origin and the evolution of such chiral signatures. In addition, the identification of such high dissymmetry factors in CD and CPL along with a very small energy gap (of the order of thermal energy) is also more than intriguing. The paradox comes from the fact that the exciton model suggests that a high dissymmetry factor resulting from strong exciton coupling must be associated with a large energy gap. On the contrary, we observe a very small energy gap of 28 meV in our artefact-free experiments on the bundled aggregates. Therefore, theoretical studies focusing on the origin of such strong chiral signals recorded from these structures might

provide extremely interesting information on the system and on the exciton coupling mechanisms. Together with the evolution of the CD signal studied in Chapter 5, a theoretical understanding of the spectral evolution can be developed to elucidate the mechanisms at play in the emergence of the measured chiroptical signals in these aggregates. Performing this theoretical study demands a thorough characterization of the photophysical properties of the monomeric, tubular, and bundled forms of the C8O3 molecules, just like presented in the thesis. Hence, the target would be to expand these initial studies with theoretical insight capable of describing the molecular packing and geometric parameters based on the experimental results presented in this thesis. Such efforts would culminate with an exhaustive theoretical framework, based on the exciton model, within which the origin of all the relevant spectral and chiroptical properties can be understood.

E. Temperature-dependent excited state polarimetry

In Chapter 3, we discussed what we coined as an anti-Kasha emissive behaviour for the C8O3 bundled aggregates. This surprising behaviour was suggested because of the bisignate profile of the CPL signal. We used the terminology "anti-Kasha" because of the observation of emission lines from multiple (in our case, two) excited states. We suggested that this unusual emission from the two excited states is made possible by the high structural rigidity of the system that reduces vibrational relaxation from the second excited state to the lowest first excited state. This simple picture still needs to be further clarified and validated. Considering that the energy gap (28 meV) is very close to the room-temperature thermal energy (25 meV), the possibility that the higher energy emission peak from the second excited state could have originated through thermal excitation from the first excited state(lowest in energy with respect to the second by a thermal quantum of energy). It is here necessary to perform an extensive temperature-dependent polarimetry study of the emission lines to analyse their relative population at various temperatures (analysed from the changes in the bisignate CPL signal). By performing this polarimetry study at different temperatures, we hope to show that, monitoring the CPL activity can be an efficient method to determine the origin of multiple excited state emissions. If this thermal population mechanism is present in the bundled aggregates, it must compete with radiative/non-radiative relaxation paths at each of the excited states. It will then be very interesting to put numbers on the relative rates of such decay processes. This can be done by performing time-resolved fluorescence spectroscopy and transient absorption spectroscopy for each of the excited states. This also constitutes an important extension of the thesis. In this regard, a unique combination of time-resolved

spectroscopic tools and Mueller polarimetry is particularly appealing to involve and exploit when aiming at understanding the unique chiroptical features associated with these fascinating C8O3 supramolecular assemblies.

Bibliography

(1) Whyte, L. L. Chirality. *Nature* **1957**, *180* (4584), 513–513.

(2) Hegstrom, R. A.; Kondepudi, D. K. The Handedness of the Universe. *Scientific American* **1990**, *262* (1), 108–115.

(3) Mason, S. The Origin of Chirality in Nature. *Trends in Pharmacological Sciences* **1986**, *7*, 20–23.

(4) Blackmond, D. G. The Origin of Biological Homochirality. *Cold Spring Harb Perspect Biol* **2010**, *2* (5), a002147.

(5) Braun, H.-B.; Kulda, J.; Roessli, B.; Visser, D.; Krämer, K. W.; Güdel, H.-U.; Böni, P. Emergence of Soliton Chirality in a Quantum Antiferromagnet. *Nature Phys* **2005**, *1* (3), 159–163.

(6) Guo, X.; Liao, J.; Wang, E. Spin Hydrodynamic Generation in the Charged Subatomic Swirl. *Sci Rep* **2020**, *10* (1), 2196.

(7) Lorchat, E.; Azzini, S.; Chervy, T.; Taniguchi, T.; Watanabe, K.; Ebbesen, T. W.; Genet, C.; Berciaud, S. Room-Temperature Valley Polarization and Coherence in Transition Metal Dichalcogenide–Graphene van Der Waals Heterostructures. *ACS Photonics* **2018**, *5* (12), 5047–5054.

(8) Inaki, M.; Liu, J.; Matsuno, K. Cell Chirality: Its Origin and Roles in Left–Right Asymmetric Development. *Philos Trans R Soc Lond B Biol Sci* **2016**, *371* (1710), 20150403.

(9) Dou, X.; Mehwish, N.; Zhao, C.; Liu, J.; Xing, C.; Feng, C. Supramolecular Hydrogels with Tunable Chirality for Promising Biomedical Applications. *Acc. Chem. Res.* **2020**, *53* (4), 852–862.

(10) Liang, B.; Zhang, L.; Jiang, Y.; Chen, S.; Yuan, M. Metal Halide Perovskites: Promising Materials toward next-Generation Circularly Polarized Luminescence. *Journal of Materials Chemistry C* **2023**, *11* (15), 4993–5008.

(11) Liu, Y.; Xing, P. Circularly Polarized Light Responsive Materials: Design Strategies and Applications. *Adv. Mater.*, **2023,** 2300968.

(12) Song, I.; Ahn, J.; Ahn, H.; Lee, S. H.; Mei, J.; Kotov, N. A.; Oh, J. H. Helical Polymers for Dissymmetric Circularly Polarized Light Imaging. *Nature* **2023**, *617* (7959), 92–99.

(13) Wang, X.; Ma, S.; Zhao, B.; Deng, J. Frontiers in Circularly Polarized Phosphorescent Materials. *Adv. Funct. Mater.* **2023**, *33* (20), 2214364.

(14) Yang, X.; Jin, X.; Zheng, A.; Duan, P. Dual Band-Edge Enhancing Overall Performance of Upconverted Near-Infrared Circularly Polarized Luminescence for Anticounterfeiting. *ACS Nano* **2023**, *17* (3), 2661–2668.

(15) Zhao, S.; Li, G.; Guo, Q.; Wang, Y.; Zhang, M.; Zhou, Y.; Jin, S.; Zhu, M.; Zhuang, T. Visualizing Circularly Polarized Long Afterglow for Information Security. *Adv. Opt. Mater.* **2023**, *11* (10), 2202933.

(16) Deng, Y.; Wang, M.; Zhuang, Y.; Liu, S.; Huang, W.; Zhao, Q. Circularly Polarized Luminescence from Organic Micro-/Nano-Structures. *Light Sci Appl* **2021**, *10* (1), 76.

(17) Frédéric, L.; Desmarchelier, A.; Plais, R.; Lavnevich, L.; Muller, G.; Villafuerte, C.; Clavier, G.; Quesnel, E.; Racine, B.; Meunier-Della-Gatta, S.; Dognon, J.-P.; Thuéry, P.; Crassous, J.; Favereau, L.; Pieters, G. Maximizing Chiral Perturbation on Thermally Activated Delayed Fluorescence Emitters and Elaboration of the First Top-Emission Circularly Polarized OLED. *Adv. Funct. Mater.* **2020**, *30* (43), 2004838.

(18) Wong, M. Y.; Zysman-Colman, E. Purely Organic Thermally Activated Delayed Fluorescence Materials for Organic Light-Emitting Diodes. *Adv Mater* **2017**, *29* (22), 1605444.

(19) Ward, T. J.; Ward, K. D. Chiral Separations: A Review of Current Topics and Trends. *Anal. Chem.* **2012**, *84* (2), 626–635.

(20) Zhan, X.; Xu, F.-F.; Zhou, Z.; Yan, Y.; Yao, J.; Zhao, Y. S. 3D Laser Displays Based on Circularly Polarized Lasing from Cholesteric Liquid Crystal Arrays. *Adv Mater* **2021**, *33* (37), 2104418.

(21) Liu, M.; Zhang, L.; Wang, T. Supramolecular Chirality in Self-Assembled Systems. *Chem. Rev.* **2015**, *115* (15), 7304–7397.

(22) Genet, C. Chiral Light–Chiral Matter Interactions: An Optical Force Perspective. *ACS Photonics* **2022**, *9* (2), 319–332.

(23) Nagib, D. A. Asymmetric Catalysis in Radical Chemistry. *Chem. Rev.* **2022**, *122* (21), 15989–15992.

(24) Lininger, A.; Palermo, G.; Guglielmelli, A.; Nicoletta, G.; Goel, M.; Hinczewski, M.; Strangi, G. Chirality in Light–Matter Interaction. *Adv Mater* **2022**, 2107325.

(25) Li, T. E.; Chen, H.-T.; Subotnik, J. E. Comparison of Different Classical, Semiclassical, and Quantum Treatments of Light–Matter Interactions: Understanding Energy Conservation. *J. Chem. Theory Comput.* **2019**, *15* (3), 1957–1973.

(26) Valeur, B.; Berberan-Santos, M. N. *Molecular Fluorescence: Principles and Applications*; John Wiley & Sons, **2012**.

(27) Gal, J. Molecular Chirality in Chemistry and Biology: Historical Milestones. *Helvetica Chimica Acta* **2013**, *96* (9), 1617–1657.

(28) Brosseau, C. Chapter 3 - Polarization and Coherence Optics: Historical Perspective, Status, and Future Directions. In *Progress in Optics*; Elsevier, **2010**; Vol. 54, pp 149–208.

(29) Kahr, B. Polarization in France. *Chirality* **2018**, *30* (4), 351–368.

(30) Leclercq, F. Arago, Biot, and Fresnel Elucidate Circular Polarization. *Revue dhistoire des sciences 66* (2), 395–416.

(31) Busch, K. W.; Busch, M. A. *Chiral Analysis*; Elsevier, **2011**.

(32) Berova, N.; Nakanishi, K.; Woody, R. W. *Circular Dichroism: Principles and Applications*; John Wiley & Sons, **2000.**

(33) Longhi, G.; Castiglioni, E.; Koshoubu, J.; Mazzeo, G.; Abbate, S. Circularly Polarized Luminescence: A Review of Experimental and Theoretical Aspects. *Chirality* **2016**, *28* (10), 696–707.

(34) Riehl, J. P.; Richardson, F. S. Circularly Polarized Luminescence Spectroscopy. *Chem. Rev.* **1986**, *86* (1), 1–16.

(35) I. Lerrick, R.; L. Winstanley, T. P.; Haggerty, K.; Wills, C.; Clegg, W.; W. Harrington, R.; Bultinck, P.; Herrebout, W.; C. Benniston, A.; J. Hall, M. Axially Chiral BODIPYs. *Chem Comm* **2014**, *50* (36), 4714–4716.

(36) Mądry, T.; Czapik, A.; Kwit, M. Point-to-Axial Chirality Transmission: A Highly Sensitive Triaryl Chirality Probe for Stereochemical Assignments of Amines. *J. Org. Chem.* **2020**, *85* (16), 10413–10431.

(37) Berova, N.; Polavarapu, P. L.; Nakanishi, K.; Woody, R. W. *Comprehensive Chiroptical Spectroscopy, Volume 2: Applications in Stereochemical Analysis of Synthetic Compounds, Natural Products, and Biomolecules*; John Wiley & Sons, **2012**.

(38) Riant, O.; Samuel, O.; Kagan, H. B. A General Asymmetric Synthesis of Ferrocenes with Planar Chirality. *J. Am. Chem. Soc.* **1993**, *115* (13), 5835–5836.

(39) Cei, M.; Di Bari, L.; Zinna, F. Circularly Polarized Luminescence of Helicenes: A Data-Informed Insight. *Chirality* **2023**, *35* (4), 192–210.

(40) Isla, H.; Crassous, J. Helicene-Based Chiroptical Switches. *Comptes Rendus Chimie* **2016**, *19* (1), 39–49.

(41) Srebro-Hooper, M.; Crassous, J.; Autschbach, J. Photophysical and Chiroptical Properties of Metal–Organic Helicenic Systems: Experiment vs. Theory. In *Helicenes*; John Wiley & Sons, Ltd, 2022; pp 395–421.

(42) Zinna, F.; Di Bari, L. Lanthanide Circularly Polarized Luminescence: Bases and Applications. *Chirality* **2015**, *27* (1), 1–13.

(43) Deng, M.; Schley, N. D.; Ung, G. High Circularly Polarized Luminescence Brightness from Analogues of Shibasaki's Lanthanide Complexes. *Chem. Commun.* **2020**, *56* (94), 14813–14816.

(44) Zinna, F.; Arrico, L.; Funaioli, T.; Bari, L. D.; Pasini, M.; Botta, C.; Giovanella, U. Modular Chiral Eu(III) Complexes for Efficient Circularly Polarized OLEDs. *J. Mater. Chem. C* **2022**, *10* (2), 463–468.

(45) Marydasan, B.; Suryaletha, K.; Lena, A. M.; Sachin, A.; Kawai, T.; Thomas, S.; Kumar, J. Chiral Nanostructures Derived from Europium(III) Complexes for Enhanced Circularly Polarised Luminescence and Antibacterial Activity. *J. Mater. Chem. C* **2022**, *10* (37), 13954–13963.

(46) Wu, W.; Pauly, M. Chiral Plasmonic Nanostructures: Recent Advances in Their Synthesis and Applications. *Mater Adv* **2022**, *3* (1), 186–215.

(47) Cho, N. H.; Guerrero-Martínez, A.; Ma, J.; Bals, S.; Kotov, N. A.; Liz-Marzán, L. M.; Nam, K. T. Bioinspired Chiral Inorganic Nanomaterials. *Nat Rev Bioeng* **2023**, *1* (2), 88–106.

(48) Kumar, J.; Thomas, K. G.; Liz-Marzán, L. M. Nanoscale Chirality in Metal and Semiconductor Nanoparticles. *Chem. Commun.* **2016**, *52* (85), 12555–12569.

(49) Nizar, N. S. S.; Sujith, M.; Swathi, K.; Sissa, C.; Painelli, A.; Thomas, K. G. Emergent Chiroptical Properties in Supramolecular and Plasmonic Assemblies. *Chem. Soc. Rev.* **2021**, *50* (20), 11208–11226.

(50) Cram, D. J. The Design of Molecular Hosts, Guests, and Their Complexes (Nobel Lecture). *Angew. Chem., Int. Ed. Engl.* **1988**, *27* (8), 1009–1020.

(51) Lehn, J.-M. Supramolecular Chemistry—Scope and Perspectives Molecules, Supermolecules, and Molecular Devices (Nobel Lecture). *Angew. Chem., Int. Ed. Engl.* **1988**, *27* (1), 89–112.

(52) Lehn, J.-M. Perspectives in Supramolecular Chemistry—From Molecular Recognition towards Molecular Information Processing and Self-Organization. *Angew. Chem., Int. Ed. Engl.* **1990**, *29* (11), 1304–1319.

(53) Uhlenheuer, D. A.; Petkau, K.; Brunsveld, L. Combining Supramolecular Chemistry with Biology. *Chem. Soc. Rev.* **2010**, *39* (8), 2817–2826.

(54) Aldaye, F. A.; Palmer, A. L.; Sleiman, H. F. Assembling Materials with DNA as the Guide. *Science* **2008**, *321* (5897), 1795–1799.

(55) Lehn, J.-M. Toward Complex Matter: Supramolecular Chemistry and Self-Organization. *Proceedings of the National Academy of Sciences* **2002**, *99* (8), 4763–4768.

(56) Menger, F. M. Supramolecular Chemistry and Self-Assembly. *Proceedings of the National Academy of Sciences* **2002**, *99* (8), 4818–4822. https://doi.org/10.1073/pnas.062524299.

(57) Kolesnichenko, I. V.; Anslyn, E. V. Practical Applications of Supramolecular Chemistry. *Chem. Soc. Rev.* **2017**, *46* (9), 2385–2390.

(58) Würthner, F.; Kaiser, T. E.; Saha-Möller, C. R. J-Aggregates: From Serendipitous Discovery to Supramolecular Engineering of Functional Dye Materials. *Angew. Chem., Int. Ed.* **2011**, *50* (15), 3376–3410.

(59) Davis, A. V.; Yeh, R. M.; Raymond, K. N. Supramolecular Assembly Dynamics. *Proceedings of the National Academy of Sciences* **2002**, *99* (8), 4793–4796.

(60) Scheibe, G. Über Die Veränderlichkeit Der Absorptionsspektren in Lösungen Und Die Nebenvalenzen Als Ihre Ursache. *Angew Chem* **1937**, *50* (11), 212–219.

(61) Scheibe, G.; Kandler, L.; Ecker, H. Polymerisation und polymere Adsorption als Ursache neuartiger Absorptionsbanden von organischen Farbstoffen. *Naturwissenschaften* **1937**, *25* (5), 75–75.

(62) Jelley, E. E. Spectral Absorption and Fluorescence of Dyes in the Molecular State. *Nature* **1936**, *138* (3502), 1009–1010.

(63) Jelley, E. E. Molecular, Nematic and Crystal States of I: I-Diethyl--Cyanine Chloride. *Nature* **1937**, *139* (3519), 631–631.

(64) Schnitzer, T.; Preuss, M. D.; van Basten, J.; Schoenmakers, S. M. C.; Spiering, A. J. H.; Vantomme, G.; Meijer, E. W. How Subtle Changes Can Make a Difference: Reproducibility in Complex Supramolecular Systems. *Angew. Chem., Int. Ed.* **2022**, *61* (41), e202206738.

(65) Jonkheijm, P.; Hoeben, F. J. M.; Kleppinger, R.; van Herrikhuyzen, J.; Schenning, A. P. H. J.; Meijer, E. W. Transfer of π-Conjugated Columnar Stacks from Solution to Surfaces. *J. Am. Chem. Soc.* **2003**, *125* (51), 15941–15949.

(66) Hermans, T. M.; Broeren, M. A. C.; Gomopoulos, N.; van der Schoot, P.; van Genderen, M. H. P.; Sommerdijk, N. A. J. M.; Fytas, G.; Meijer, E. W. Self-Assembly of Soft Nanoparticles with Tunable Patchiness. *Nature Nanotech* **2009**, *4* (11), 721–726.

(67) Wolffs, M.; Korevaar, P. A.; Jonkheijm, P.; Henze, O.; Feast, W. J.; Schenning, A. P. H. J.; Meijer, E. W. The Role of Heterogeneous Nucleation in the Self-Assembly of Oligothiophenes. *Chem. Commun.* **2008**, No. 38, 4613–4615.

(68) Korevaar, P. A.; George, S. J.; Markvoort, A. J.; Smulders, M. M. J.; Hilbers, P. A. J.; Schenning, A. P. H. J.; De Greef, T. F. A.; Meijer, E. W. Pathway Complexity in Supramolecular Polymerization. *Nature* **2012**, *481* (7382), 492–496.

(69) Tidhar, Y.; Weissman, H.; Wolf, S. G.; Gulino, A.; Rybtchinski, B. Pathway-Dependent Self-Assembly of Perylene Diimide/Peptide Conjugates in Aqueous Medium. *Chemistry – A European Journal* **2011**, *17* (22), 6068–6075.

(70) Matern, J.; Dorca, Y.; Sánchez, L.; Fernández, G. Revising Complex Supramolecular Polymerization under Kinetic and Thermodynamic Control. *Angew. Chem., Int. Ed.* **2019**, *58* (47), 16730–16740.

(71) Tidhar, Y.; Weissman, H.; Wolf, S. G.; Gulino, A.; Rybtchinski, B. Pathway-Dependent Self-Assembly of Perylene Diimide/Peptide Conjugates in Aqueous Medium. *Chem. Eur. J.* **2011**, *17* (22), 6068–6075.

(72) Kar, S.; Swathi, K.; Sissa, C.; Painelli, A.; Thomas, K. G. Emergence of Chiroptical Properties in Molecular Assemblies of Phenyleneethynylenes: The Role of Quasi-Degenerate Excitations. *J. Phys. Chem. Lett.* **2018**, *9* (16), 4584–4590.

(73) Huang, S.; Yu, H.; Li, Q. Supramolecular Chirality Transfer toward Chiral Aggregation: Asymmetric Hierarchical Self-Assembly. *Adv. Sci* **2021**, *8* (8), 2002132.

(74) Huang, Z.; Kang, S.-K.; Lee, M. Induction of Supramolecular Chirality in Self-Assembled Nanofibers Triggered by Environmental Change. *J. Mater. Chem.* **2011**, *21* (39), 15327–15331.

(75) Azeroual, S.; Surprenant, J.; Lazzara, T. D.; Kocun, M.; Tao, Y.; Cuccia, L. A.; Lehn, J.-M. Mirror Symmetry Breaking and Chiral Amplification in Foldamer-Based Supramolecular Helical Aggregates. *Chem. Commun.* **2012**, *48* (17), 2292–2294.

(76) Kirstein, S.; von Berlepsch, H.; Böttcher, C.; Burger, C.; Ouart, A.; Reck, G.; Dähne, S. Chiral J-Aggregates Formed by Achiral Cyanine Dyes. *ChemPhysChem* **2000**, *1* (3), 146–150.

(77) Hananel, U.; Ben-Moshe, A.; Diamant, H.; Markovich, G. Spontaneous and Directed Symmetry Breaking in the Formation of Chiral Nanocrystals. *Proceedings of the National Academy of Sciences* **2019**, *116* (23), 11159–11164.

(78) Pawlik, A.; Kirstein, S.; De Rossi, U.; Daehne, S. Structural Conditions for Spontaneous Generation of Optical Activity in J-Aggregates. *J. Phys. Chem. B* **1997**, *101* (29), 5646–5651.

(79) Banwell, C. N.; McCash, E. M. *Fundamentals of Molecular Spectroscopy*; McGraw-Hill, 1994.

(80) Condon, E. U. Theories of Optical Rotatory Power. *Rev. Mod. Phys.* **1937**, *9* (4), 432–457.

(81) Craig, D. P.; Thirunamachandran, T. *Molecular Quantum Electrodynamics: An Introduction to Radiation-Molecule Interactions*; Courier Corporation, **1998**.

(82) Tanaka, H.; Ikenosako, M.; Kato, Y.; Fujiki, M.; Inoue, Y.; Mori, T. Symmetry-Based Rational Design for Boosting Chiroptical Responses. *Commun Chem* **2018**, *1* (1), 1–8.

(83) Zhang, X.; Nau, W. M. Chromophore Alignment in a Chiral Host Provides a Sensitive Test for the Orientation – Intensity Rule of Induced Circular Dichroism. *Angew. Chem., Int. Ed.* **2000**, *39* (3), 544–547.

(84) Holmgaard List, N.; Knoops, J.; Rubio-Magnieto, J.; Idé, J.; Beljonne, D.; Norman, P.; Surin, M.; Linares, M. Origin of DNA-Induced Circular Dichroism in a Minor-Groove Binder. *J. Am. Chem. Soc.* **2017**, *139* (42), 14947–14953.

(85) Zhang, Y.; Yu, W.; Li, H.; Zheng, W.; Cheng, Y. Induced CPL-Active Materials Based on Chiral Supramolecular Co-Assemblies. *Chem. Eur. J.* **2023**, *29* (22), e202204039.

(86) Allenmark, S. Induced Circular Dichroism by Chiral Molecular Interaction. *Chirality* **2003**, *15* (5), 409–422.

(87) Harata, K. Induced Circular Dichroism of Cycloamylose Complexes with Meta- and Para-Disubstituted Benzenes. *Bioorganic Chemistry* **1981**, *10* (3), 255–265.

(88) Somasundaran, S. M.; Kompella, S. V. K.; Mohan T. M, N.; Das, S.; Abdul Vahid, A.; Vijayan, V.; Balasubramanian, S.; Thomas, K. G. Structurally Induced Chirality of an Achiral Chromophore on Self-Assembled Nanofibers: A Twist Makes It Chiral. *ACS Nano* **2023,** *17***,** 11054–11069.

(89) Inskeep, W. H.; Miles, D. W.; Eyring, H. Circular Dichroism of Nucleoside Derivatives. VIII. Coupled Oscillator Calculations of Molecules with Fixed Structure. *J. Am. Chem. Soc.* **1970**, *92* (13), 3866–3872.

(90) Holmgaard List, N.; Knoops, J.; Rubio-Magnieto, J.; Idé, J.; Beljonne, D.; Norman, P.; Surin, M.; Linares, M. Origin of DNA-Induced Circular Dichroism in a Minor-Groove Binder. *J. Am. Chem. Soc.* **2017**, *139* (42), 14947–14953.

(91) Kasha, M.; Rawls, H. R.; Ashraf El-Bayoumi, M. The Exciton Model in Molecular Spectroscopy. *Pure Appl. Chem.* **1965**, *11* (3), 371–392.

(92) Davydov, A. S. *Theory of Molecular Excitons*; Springer US: Boston, MA, 1971.

(93) Kasha, M. Characterization of Electronic Transitions in Complex Molecules. *Discuss. Faraday Soc.* **1950**, *9* (0), 14–19.

(94) Kuhn, W. The Physical Significance of Optical Rotatory Power. *Trans. Faraday Soc.* **1930**, *26* (0), 293–308.

(95) McRae, E. G.; Kasha, M. Enhancement of Phosphorescence Ability upon Aggregation of Dye Molecules. *The Journal of Chemical Physics* **2004**, *28* (4), 721–722.

(96) Kasha, M. Energy Transfer Mechanisms and the Molecular Exciton Model for Molecular Aggregates1, 2. *rare* **2012**, *178* (2).

(97) Harada, N.; Ohashi, M.; Nakanishi, K. The Benzoate Sector Rule, a Method for Determining the Absolute Configurations of Cyclic Secondary Alcohols. *J. Am. Chem. Soc.* **1968**, *90* (26), 7349–7351.

(98) Harada, N.; Chen, S.-M. L.; Nakanishi, K. Quantitative Definition of Exciton Chirality and the Distant Effect in the Exciton Chirality Method. *J. Am. Chem. Soc.* **1975**, *97* (19), 5345–5352.

(99) Hochstrasser, R. M.; Kasha, M. Application of the Exciton Model to Mono-Molecular Lamellar Systems. *Photochemistry and Photobiology* **1964**, *3* (4), 317–331.

(100) Thomas, R.; Kumar, J.; George, J.; Shanthil, M.; Naidu, G. N.; Swathi, R. S.; Thomas, K. G. Coupling of Elementary Electronic Excitations: Drawing Parallels Between Excitons and Plasmons. *J. Phys. Chem. Lett.* **2018**, *9* (4), 919–932.

(101) Barotov, U.; Thanippuli Arachchi, D. H.; Klein, M. D.; Zhang, J.; Šverko, T.; Bawendi, M. G. Near-Unity Superradiant Emission from Delocalized Frenkel Excitons in a Two-Dimensional Supramolecular Assembly. *Adv. Opt. Mater.* **2023**, *11* (2), 2201471.

(102) Sebastian, E.; Philip, A. M.; Benny, A.; Hariharan, M. Null Exciton Splitting in Chromophoric Greek Cross (+) Aggregate. *Angew. Chem., Int. Ed.* **2018**, *57* (48), 15696–15701.

(103) Swathi, K.; Sissa, C.; Painelli, A.; Thomas, K. G. Supramolecular Chirality: A Caveat in Assigning the Handedness of Chiral Aggregates. *Chem. Commun.* **2020**, *56* (59), 8281–8284.

(104) Demchenko, A. P.; Tomin, V. I.; Chou, P.-T. Breaking the Kasha Rule for More Efficient Photochemistry. *Chem. Rev.* **2017**, *117* (21), 13353–13381.

(105) Bertocchi, F.; Sissa, C.; Painelli, A. Circular Dichroism of Molecular Aggregates: A Tutorial. *Chirality* **2023**, *35* (10), 681-691.

(106) Hestand, N. J.; Spano, F. C. Expanded Theory of H- and J-Molecular Aggregates: The Effects of Vibronic Coupling and Intermolecular Charge Transfer. *Chem. Rev.* **2018**, *118* (15), 7069–7163.

(107) Spano, F. C.; Clark, J.; Silva, C.; Friend, R. H. Determining Exciton Coherence from the Photoluminescence Spectral Line Shape in Poly(3-Hexylthiophene) Thin Films. *J. Chem. Phys.* **2009**, *130* (7), 074904.

(108) Spano, F. C. Modeling Disorder in Polymer Aggregates: The Optical Spectroscopy of Regioregular Poly(3-Hexylthiophene) Thin Films. *J. Chem. Phys.* **2005**, *122* (23), 234701.

(109) Kaiser, T. E.; Scheblykin, I. G.; Thomsson, D.; Würthner, F. Temperature-Dependent Exciton Dynamics in J-Aggregates—When Disorder Plays a Role. *J. Phys. Chem. B* **2009**, *113* (48), 15836–15842.

(110) Spano, F. C.; Meskers, S. C. J.; Hennebicq, E.; Beljonne, D. Probing Excitation Delocalization in Supramolecular Chiral Stacks by Means of Circularly Polarized Light: Experiment and Modeling. *J. Am. Chem. Soc.* **2007**, *129* (22), 7044–7054.

(111) Spano, F. C.; Meskers, S. C. J.; Hennebicq, E.; Beljonne, D. Using Circularly Polarized Luminescence to Probe Exciton Coherence in Disordered Helical Aggregates. *J. Chem. Phys* **2008**, *129* (2), 024704.

(112) Scholes, G. D. Limits of Exciton Delocalization in Molecular Aggregates. *Faraday Discuss.* **2019**, *221* (0), 265–280.

(113) van Dijk, L.; Bobbert, P. A.; Spano, F. C. Extreme Sensitivity of Circular Dichroism to Long-Range Excitonic Couplings in Helical Supramolecular Assemblies. *J. Phys. Chem. B* **2010**, *114* (2), 817–825.

(114) Spano, F. C.; Meskers, S. C. J.; Hennebicq, E.; Beljonne, D. Using Circularly Polarized Luminescence to Probe Exciton Coherence in Disordered Helical Aggregates. *J. Chem. Phys* **2008**, *129* (2), 024704.

(115) Tempelaar, R.; Stradomska, A.; Knoester, J.; Spano, F. C. Circularly Polarized Luminescence as a Probe for Long-Range Interactions in Molecular Aggregates. *J. Phys. Chem. B* **2011**, *115* (36), 10592–10603.

(116) Tanaka, H.; Inoue, Y.; Mori, T. Circularly Polarized Luminescence and Circular Dichroisms in Small Organic Molecules: Correlation between Excitation and Emission Dissymmetry Factors. *ChemPhotoChem* **2018**, *2* (5), 386–402.

(117) Morisaki, Y.; Gon, M.; Sasamori, T.; Tokitoh, N.; Chujo, Y. Planar Chiral Tetrasubstituted [2.2]Paracyclophane: Optical Resolution and Functionalization. *J. Am. Chem. Soc.* **2014**, *136* (9), 3350–3353.

(118) Mason, W. R. *Magnetic Circular Dichroism Spectroscopy*; John Wiley & Sons, **2007**.

(119) Cheesman, M. R.; Greenwood, C.; Thomson, A. J. Magnetic Circular Dichroism of Hemoproteins. In *Advances in Inorganic Chemistry*; Sykes, A. G., Ed.; Academic Press, **1991**; Vol. 36, pp 201–255.

(120) Solomon, E. I.; Pavel, E. G.; Loeb, K. E.; Campochiaro, C. Magnetic Circular Dichroism Spectroscopy as a Probe of the Geometric and Electronic Structure of Non-Heme Ferrous Enzymes. *Coord. Chem. Rev* **1995**, *144*, 369–460.

(121) Gao, X.; Zhang, X.; Yang, X.; Zhao, L.; Han, B.; Alanagh, H. R.; Tang, Z. Detecting Electronic Structure Evolution of Semiconductor Nanocrystals by Magnetic Circular Dichroism Spectroscopy. *Nanoscale* **2019**, *11* (41), 19380–19386.

(122) Tinoco, I.; Turner, D. H. Fluorescence Detected Circular Dichroism. Theory. *J. Am. Chem. Soc.* **1976**, *98* (21), 6453–6456.

(123) Turner, D. H. Fluorescence-Detected Circular Dichroism. In *Methods in Enzymology*; Enzyme Structure Part G; Academic Press, **1978**; Vol. 49, pp 199–214.

(124) Tanaka, K.; Pescitelli, G.; Nakanishi, K.; Berova, N. Fluorescence Detected Exciton Coupled Circular Dichroism: Development of New Fluorescent Reporter Groups for Structural Studies. *Monatshefte für Chemie* **2005**, *136* (3), 367–395.

(125) Prabodh, A.; Wang, Y.; Sinn, S.; Albertini, P.; Spies, C.; Spuling, E.; Yang, L.-P.; Jiang, W.; Bräse, S.; Biedermann, F. Fluorescence Detected Circular Dichroism (FDCD) for Supramolecular Host–Guest Complexes. *Chem. Sci.* **2021**, *12* (27), 9420–9431.

(126) Nafie, L. A.; Keiderling, T. A.; Stephens, P. J. Vibrational Circular Dichroism. *J. Am. Chem. Soc.* **1976**, *98* (10), 2715–2723.

(127) Le Barbu-Debus, K.; Zehnacker, A. Competition between Inter and Intramolecular Hydrogen Bond Evidenced by Vibrational Circular Dichroism Spectroscopy: The Case of (1S,2R)-(−)-Cis-1-Amino-2-Indanol. *Chirality* **2021**, *33* (12), 858–874.

(128) Jähnigen, S.; Le Barbu-Debus, K.; Guillot, R.; Vuilleumier, R.; Zehnacker, A. How Crystal Symmetry Dictates Non-Local Vibrational Circular Dichroism in the Solid State. *Angew. Chem., Int. Ed* **2023**, *62* (5), e202215599.

(129) Dupont, J.; Guillot, R.; Lepère, V.; Zehnacker, A. Jet-Cooled Laser Spectroscopy and Solid-State Vibrational Circular Dichroism of the Cyclo-(Tyr-Phe) Diketopiperazine Dipeptide. *J. Mol. Struct.* **2022**, *1262*, 133059.

(130) Gautier, C.; Bürgi, T. Vibrational Circular Dichroism of Adsorbed Molecules: BINAS on Gold Nanoparticles. *J. Phys. Chem. C* **2010**, *114* (38), 15897–15902.

(131) Nafie, L. A.; Cheng, J. C.; Stephens, P. J. Vibrational Circular Dichroism of 2,2,2-Trifluoro-1-Phenylethanol. *J. Am. Chem. Soc.* **1975**, *97* (13), 3842–3843.

(132) Stephens, P. J.; Devlin, F. J.; Pan, J.-J. The Determination of the Absolute Configurations of Chiral Molecules Using Vibrational Circular Dichroism (VCD) Spectroscopy. *Chirality* **2008**, *20* (5), 643–663.

(133) Auvray, F.; Dennetiere, D.; Giuliani, A.; Jamme, F.; Wien, F.; Nay, B.; Zirah, S.; Polack, F.; Menneglier, C.; Lagarde, B.; Hirst, J. D.; Réfrégiers, M. Time Resolved Transient Circular Dichroism Spectroscopy Using Synchrotron Natural Polarization. *Structural Dynamics* **2019**, *6* (5), 054307.

(134) Lux, C.; Wollenhaupt, M.; Bolze, T.; Liang, Q.; Köhler, J.; Sarpe, C.; Baumert, T. Circular Dichroism in the Photoelectron Angular Distributions of Camphor and Fenchone from Multiphoton Ionization with Femtosecond Laser Pulses. *Angew. Chem., Int. Ed* **2012**, *51* (20), 5001–5005.

(135) Lees, J. G.; Wallace, B. A. Synchrotron Radiation Circular Dichroism and Conventional Circular Dichroism Spectroscopy: A Comparison. *Spectroscopy* **2002**, *16* (3–4), 121–125.

(136) Wallace, B. A. Conformational Changes by Synchrotron Radiation Circular Dichroism Spectroscopy. *Nat Struct Mol Biol* **2000**, *7* (9), 708–709.

(137) Wallace, B. A.; Wien, F.; Miles, A. J.; Lees, J. G.; Hoffmann, S. V.; Evans, P.; Wistow, G. J.; Slingsby, C. Biomedical Applications of Synchrotron Radiation Circular Dichroism Spectroscopy: Identification of Mutant Proteins Associated with Disease and Development of a Reference Database for Fold Motifs. *Faraday Discuss.* **2004**, *126* (0), 237–243.

(138) Clark Sutherland, J.; Desmond, E. J.; Takacs, P. Z. Versatile Spectrometer for Experiments Using Synchrotron Radiation at Wave-Lengths Greater than 100 Nm. *Nuclear Instruments and Methods* **1980**, *172* (1), 195–199.

(139) Dupont, J.; Lepère, V.; Zehnacker, A.; Hartweg, S.; Garcia, G. A.; Nahon, L. Photoelectron Circular Dichroism as a Signature of Subtle Conformational Changes:

The Case of Ring Inversion in 1-Indanol. *J. Phys. Chem. Lett.* **2022**, *13* (10), 2313–2320.

(140) Powis, I.; Harding, C. J.; Garcia, G. A.; Nahon, L. A Valence Photoelectron Imaging Investigation of Chiral Asymmetry in the Photoionization of Fenchone and Camphor. *ChemPhysChem* **2008**, *9* (3), 475–483.

(141) Turchini, S.; Catone, D.; Contini, G.; Zema, N.; Irrera, S.; Stener, M.; Di Tommaso, D.; Decleva, P.; Prosperi, T. Conformational Effects in Photoelectron Circular Dichroism of Alaninol. *ChemPhysChem* **2009**, *10* (11), 1839–1846.

(142) Sen, A.; Pratt, S. T.; Reid, K. L. Circular Dichroism in Photoelectron Images from Aligned Nitric Oxide Molecules. *The Journal of Chemical Physics* **2017**, *147* (1), 013927.

(143) Thomas, A.; Chervy, T.; Azzini, S.; Li, M.; George, J.; Genet, C.; Ebbesen, T. W. Mueller Polarimetry of Chiral Supramolecular Assembly. *J. Phys. Chem. C* **2018**, *122* (25), 14205–14212.

(144) Disch, R. L.; Sverdlik, D. I. Apparent Circular Dichroism of Oriented Systems. *Anal. Chem.* **1969**, *41* (1), 82–86.

(145) Salij, A.; Goldsmith, R. H.; Tempelaar, R. Theory of Apparent Circular Dichroism Reveals the Origin of Inverted and Noninverted Chiroptical Response under Sample Flipping. *J. Am. Chem. Soc.* **2021** , *143* (51), 21519–21531.

(146) Shindo, Y.; Ohmi, Y. Problems of CD Spectrometers. 3. Critical Comments on Liquid Crystal Induced Circular Dichroism. *J. Am. Chem. Soc.* **1985**, *107* (1), 91–97.

(147) Shindo, Y.; Nakagawa, M.; Ohmi, Y. On the Problems of CD Spectropolarimeters. II: Artifacts in CD Spectrometers. *Appl Spectrosc* **1985**, *39* (5), 860–868.

(148) Urry, D. W.; Hinners, T. A.; Krivacic, J. Distortions in the Circular Dichroism of Nonoriented Poly-L-Alanine Films. *Anal Biochem* **1970**, *37* (1), 85–91.

(149) Castiglioni, E.; Biscarini, P.; Abbate, S. Experimental Aspects of Solid State Circular Dichroism. *Chirality* **2009**, *21* (1E), E28–E36.

(150) Yao, H.; Isohashi, T.; Kimura, K. Detection of Spectral Inhomogeneities of Mesoscopic Thiacyanine J Aggregates in Solution by the Apparent CD Spectral Measurement. *Chemical Physics Letters* **2006**, *419* (1), 21–27.

(151) Shindo, Y.; Nishio, M. The Effect of Linear Anisotropies on the CD Spectrum: Is It True That the Oriented Polyvinyalcohol Film Has a Magic Chiral Domain Inducing Optical Activity in Achiral Molecules? *Biopolymers* **1990**, *30* (1–2), 25–31.

(152) Hipps, K. W.; Crosby, G. A. Applications of the Photoelastic Modulator to Polarization Spectroscopy. *J. Phys. Chem.* **1979**, *83* (5), 555–562.

(153) Dekkers, H. P. J. M.; Moraal, P. F.; Timper, J. M.; Riehl, J. P. Optical Artifacts in Circularly Polarized Luminescence Spectroscopy. *Appl Spectrosc* **1985**, *39* (5), 818–821.

(154) Blok, P. M. L.; Dekkers, H. P. J. M. Measurement of the Circular Polarization of the Luminescence of Photoselected Samples Under Artifact-Free Conditions. *Appl. Spectrosc., AS* **1990**, *44* (2), 305–309.

(155) Shindo, Y.; Ohmi, Y. New Polarization-modulation Spectrometer for Simultaneous Circular Dichroism and Optical Rotary Dispersion Measurements (I): Instrument Design, Analysis, and Evaluation. *Review of Scientific Instruments* **1985**, *56* (12), 2237–2242.

(156) Kuroda, R.; Harada, T.; Shindo, Y. A Solid-State Dedicated Circular Dichroism Spectrophotometer: Development and Application. *Rev. Sci. Instrum.* **2001**, *72* (10), 3802–3810.

(157) Kuroda, R.; Honma, T. CD Spectra of Solid-State Samples. *Chirality* **2000**, *12* (4), 269–277.

(158) Freudenthal, J. H.; Hollis, E.; Kahr, B. Imaging Chiroptical Artifacts. *Chirality* **2009**, *21 Suppl 1*, E20-27.

(159) Arteaga, O.; Canillas, A. Analytic Inversion of the Mueller-Jones Polarization Matrices for Homogeneous Media. *Opt. Lett., OL* **2010**, *35* (4), 559–561.

(160) Arteaga, O.; Baldrís, M.; Antó, J.; Canillas, A.; Pascual, E.; Bertran, E. Mueller Matrix Microscope with a Dual Continuous Rotating Compensator Setup and Digital Demodulation. *Applied Optics* **2014**, *53* (10), 2236–2245.

(161) Arteaga, O.; Canillas, A.; Crusats, J.; El-Hachemi, Z.; Llorens, J.; Sacristan, E.; Ribo, J. M. Emergence of Supramolecular Chirality by Flows. *ChemPhysChem* **2010**, *11* (16), 3511–3516.

(162) Wan, L.; Wade, J.; Salerno, F.; Arteaga, O.; Laidlaw, B.; Wang, X.; Penfold, T.; Fuchter, M. J.; Campbell, A. J. Inverting the Handedness of Circularly Polarized Luminescence from Light-Emitting Polymers Using Film Thickness. *ACS Nano* **2019**, *13* (7), 8099–8105.

(163) Arteaga, O.; Nichols, S.; Kahr, B. Mueller Matrices in Fluorescence Scattering. *Opt. Lett., OL* **2012**, *37* (14), 2835–2837.

(164) Li, M. Mueller Polarimetry for Probing Supramolecular and Optical Chiralities. These de doctorat, Strasbourg, **2020**.

(165) Gautier, J. Effets de Chiralité En Régime de Couplage Fort Lumière-Matière. These de doctorat, Strasbourg, **2022**.

(166) Jones, R. C. A New Calculus for the Treatment of Optical SystemsI. Description and Discussion of the Calculus. *J. Opt. Soc. Am., JOSA* **1941**, *31* (7), 488–493.

(167) Hecht, E. *Optics*; Pearson, **2012**.

(168) Hovenier, J. W. Structure of a General Pure Mueller Matrix. *Appl. Opt., AO* **1994**, *33* (36), 8318–8324.

(169) Simon, R. Mueller Matrices and Depolarization Criteria. *J. Mod. Opt.* **1987**, *34* (4), 569–575.

(170) Barriel, O. A. *Mueller Matrix Polarimetry of Anisotropic Chiral Media*; **2010**.

(171) Boulbry, B.; Bousquet, B.; Jeune, B. L.; Guern, Y.; Lotrian, J. Polarization Errors Associated with Zero-Order Achromatic Quarter-Wave Plates in the Whole Visible Spectral Range. *Opt. Express, OE* **2001**, *9* (5), 225–235.

(172) Ortega-Quijano, N.; Arce-Diego, J. L. Mueller Matrix Differential Decomposition. *Opt. Lett., OL* **2011**, *36* (10), 1942–1944.

(173) Ossikovski, R. Differential and Product Mueller Matrix Decompositions: A Formal Comparison. *Opt. Lett., OL* **2012**, *37* (2), 220–222.

(174) Arwin, H.; Schoeche, S.; Hilfiker, J.; Hartveit, M.; Järrendahl, K.; Juárez-Rivera, O. R.; Mendoza-Galván, A.; Magnusson, R. Optical Chirality Determined from Mueller Matrices. *Appl. Sci.* **2021**, *11* (15), 6742.

(175) Arteaga, O. Number of Independent Parameters in the Mueller Matrix Representation of Homogeneous Depolarizing Media. *Opt. Lett., OL* **2013**, *38* (7), 1131–1133.

(176) Pugzlys, A.; Hania, P. R.; Augulis, R.; Duppen, K.; van Loosdrecht, P. H. M. Cylindrical Aggregates of 5,5',6,6'-Tetrachlorobenzimida-Carbocyanine Amphiphilic Derivatives: Structure-Related Optical Properties and Exciton Dynamics. *Int. J. Photoenergy* **2006**, *2006*, e29623.

(177) Diaspro, A.; Chirico, G.; Usai, C.; Ramoino, P.; Dobrucki, J. Photobleaching. In *Handbook Of Biological Confocal Microscopy*; Pawley, J. B., Ed.; Springer US: Boston, MA, **2006**; pp 690–702.

(178) Talhavini, M.; Atvars, T. D. Z. Photostability of Xanthene Molecules Trapped in Poly(Vinyl Alcohol) (PVA) Matrices. *J. Photochem. Photobiol., A* **1999**, *120* (2), 141–149.

(179) Zondervan, R.; Kulzer, F.; Kol'chenk, M. A.; Orrit, M. Photobleaching of Rhodamine 6G in Poly(Vinyl Alcohol) at the Ensemble and Single-Molecule Levels. *J. Phys. Chem. A* **2004**, *108* (10), 1657–1665.

(180) Klein, M. D.; Shulenberger, K. E.; Barotov, U.; Šverko, T.; Bawendi, M. G. Supramolecular Lattice Deformation and Exciton Trapping in Nanotubular J-Aggregates. *J. Phys. Chem. C* **2022**, *126* (8), 4095–4105.

(181) Maji, K.; Saha, S.; Dey, R.; Ghosh, N.; Haldar, D. Mueller Matrix Fluorescence Spectroscopy for Probing Self-Assembled Peptide-Based Hybrid Supramolecular Structure and Orientation. *J. Phys. Chem. C* **2017**, *121* (35), 19519–19529. https://doi.org/10.1021/acs.jpcc.7b06725.

(182) Saha, S.; Soni, J.; Chandel, S.; Ghosh, N.; Kumar, U. Probing Intrinsic Anisotropies of Fluorescence: Mueller Matrix Approach. *JBO* **2015**, *20* (8), 085005.

(183) Dhbaibi, K.; Abella, L.; Meunier-Della-Gatta, S.; Roisnel, T.; Vanthuyne, N.; Jamoussi, B.; Pieters, G.; Racine, B.; Quesnel, E.; Autschbach, J.; Crassous, J.; Favereau, L. Achieving High Circularly Polarized Luminescence with Push–Pull Helicenic Systems: From Rationalized Design to Top-Emission CP-OLED Applications. *Chem. Sci.* **2021**, *12* (15), 5522–5533.

(184) Schulz, M.; Balzer, F.; Scheunemann, D.; Arteaga, O.; Lützen, A.; Meskers, S. C. J.; Schiek, M. Chiral Excitonic Organic Photodiodes for Direct Detection of Circular Polarized Light. *Advanced Functional Materials* **2019**, *29* (16), 1900684.

(185) Feringa, B. L.; van Delden, R. A.; Koumura, N.; Geertsema, E. M. Chiroptical Molecular Switches. *Chem Rev* **2000**, *100* (5), 1789–1816.

(186) Qu, D.; Archimi, M.; Camposeo, A.; Pisignano, D.; Zussman, E. Circularly Polarized Laser with Chiral Nematic Cellulose Nanocrystal Cavity. *ACS Nano* **2021**, *15* (5), 8753–8760.

(187) Zhang, C.; Wang, X.; Qiu, L. Circularly Polarized Photodetectors Based on Chiral Materials: A Review. *Front. Chem.* **2021**, *9*.

(188) He, J.; Bian, K.; Li, N.; Piao, G. Generation of Full-Color and Switchable Circularly Polarized Luminescence from Nonchiral Dyes Assembled in Cholesteric Cellulose Films. *J. Mater. Chem. C* **2019**, *7* (30), 9278–9283.

(189) Zhao, B.; Pan, K.; Deng, J. Intense Circularly Polarized Luminescence Contributed by Helical Chirality of Monosubstituted Polyacetylenes. *Macromolecules* **2018**, *51* (18), 7104–7111.

(190) Furumi, S. Recent Progress in Chiral Photonic Band-Gap Liquid Crystals for Laser Applications. *Chem Rec* **2010**, *10* (6), 394–408.

(191) Kitagawa, Y.; Tsurui, M.; Hasegawa, Y. Steric and Electronic Control of Chiral Eu(III) Complexes for Effective Circularly Polarized Luminescence. *ACS Omega* **2020**, *5* (8), 3786–3791.

(192) Wade, J.; Salerno, F.; Kilbride, R. C.; Kim, D. K.; Schmidt, J. A.; Smith, J. A.; LeBlanc, L. M.; Wolpert, E. H.; Adeleke, A. A.; Johnson, E. R.; Nelson, J.; Mori, T.; Jelfs, K. E.; Heutz, S.; Fuchter, M. J. Controlling Anisotropic Properties by Manipulating the Orientation of Chiral Small Molecules. *Nat. Chem.* **2022**, *14* (12), 1383–1389.

(193) Amako, T.; Kimoto, T.; Tajima, N.; Fujiki, M.; Imai, Y. A Comparison of Circularly Polarized Luminescence (CPL) and Circular Dichroism (CD) Characteristics of Four Axially Chiral Binaphthyl-2,2′-Diyl Hydrogen Phosphate Derivatives. *Tetrahedron* **2013**, *69* (13), 2753–2757.

(194) Saleh, N.; Srebro, M.; Reynaldo, T.; Vanthuyne, N.; Toupet, L.; Chang, V. Y.; Muller, G.; Williams, J. A. G.; Roussel, C.; Autschbach, J.; Crassous, J. Enantio-Enriched CPL-Active Helicene–Bipyridine–Rhenium Complexes. *Chem. Commun.* **2015**, *51* (18), 3754–3757.

(195) Dhbaibi, K.; Favereau, L.; Srebro-Hooper, M.; Jean, M.; Vanthuyne, N.; Zinna, F.; Jamoussi, B.; Bari, L. D.; Autschbach, J.; Crassous, J. Exciton Coupling in Diketopyrrolopyrrole–Helicene Derivatives Leads to Red and near-Infrared Circularly Polarized Luminescence. *Chem. Sci.* **2018**, *9* (3), 735–742.

(196) Li, Y.; Li, Q.; Miao, X.; Qin, C.; Chu, D.; Cao, L. Adaptive Chirality of an Achiral Cucurbit[8]Uril-Based Supramolecular Organic Framework for Chirality Induction in Water. *Angew. Chem., Int. Ed* **2021**, *60* (12), 6744–6751.

(197) Lunkley, J. L.; Shirotani, D.; Yamanari, K.; Kaizaki, S.; Muller, G. Extraordinary Circularly Polarized Luminescence Activity Exhibited by Cesium Tetrakis(3-Heptafluoro-Butylryl-(+)-Camphorato) Eu(III) Complexes in EtOH and CHCl3 Solutions. *J. Am. Chem. Soc.* **2008**, *130* (42), 13814–13815.

(198) Muller, G. Luminescent Chiral Lanthanide(III) Complexes as Potential Molecular Probes. *Dalton Trans.* **2009**, No. 44, 9692–9707.

(199) Liu, W.-D.; Li, G.-J.; Xu, H.; Deng, Y.-K.; Du, M.-H.; Long, L.-S.; Zheng, L.-S.; Kong, X.-J. Circularly Polarized Luminescence and Performance Modulation of Chiral Europium-Titanium (Eu2Ti4)-Oxo Clusters. *Chem. Commun.* **2023**, *59* (3), 346–349.

(200) Marydasan, B.; Suryaletha, K.; Lena, A. M.; Sachin, A.; Kawai, T.; Thomas, S.; Kumar, J. Chiral Nanostructures Derived from Europium(III) Complexes for Enhanced Circularly Polarised Luminescence and Antibacterial Activity. *J. Mater. Chem. C* **2022**, *10* (37), 13954–13963.

(201) Albano, G.; Aronica, L. A.; Minotto, A.; Cacialli, F.; Di Bari, L. Chiral Oligothiophenes with Remarkable Circularly Polarized Luminescence and Electroluminescence in Thin Films. *Chem. Eur. J.* **2020**, *26* (70), 16622–16627.

(202) Liu, J.; Su, H.; Meng, L.; Zhao, Y.; Deng, C.; Ng, J. C. Y.; Lu, P.; Faisal, M.; Lam, J. W. Y.; Huang, X.; Wu, H.; Wong, K. S.; Tang, B. Z. What Makes Efficient Circularly Polarised Luminescence in the Condensed Phase: Aggregation-Induced Circular Dichroism and Light Emission. *Chem. Sci.* **2012**, *3* (9), 2737–2747.

(203) Deng, Y.; Wang, M.; Zhuang, Y.; Liu, S.; Huang, W.; Zhao, Q. Circularly Polarized Luminescence from Organic Micro-/Nano-Structures. *Light Sci Appl* **2021**, *10* (1), 76.

(204) Albano, G., Pescitelli, G., Di Bari, L., Chiroptical Properties in Thin Films of π-Conjugated Systems. *Chem.Rev.* **2020***, 120* (18)*, 10145−10243.*

(205) Tempelaar, R.; Stradomska, A.; Knoester, J.; Spano, F. C. Circularly Polarized Luminescence as a Probe for Long-Range Interactions in Molecular Aggregates. *J. Phys. Chem. B* **2011**, *115* (36), 10592–10603.

(206) Albano, G., Pescitelli, G., Di Bari, L., Chiroptical Properties in Thin Films of π-Conjugated Systems. *Chem.Rev.* **2020***, 120* (18)*, 10145−10243.*

(207) Doria, S.; Sinclair, T. S.; Klein, N. D.; Bennett, D. I. G.; Chuang, C.; Freyria, F. S.; Steiner, C. P.; Foggi, P.; Nelson, K. A.; Cao, J.; Aspuru-Guzik, A.; Lloyd, S.; Caram, J. R.; Bawendi, M. G. Photochemical Control of Exciton Superradiance in Light-Harvesting Nanotubes. *ACS Nano* **2018**, *12* (5), 4556–4564.

(208) Würthner, F.; Kaiser, T. E.; Saha-Möller, C. R. J-Aggregates: From Serendipitous Discovery to Supramolecular Engineering of Functional Dye Materials. *Angew Chem Int Ed Engl* **2011**, *50* (15), 3376–3410.

(209) Eisele, D. M.; Cone, C. W.; Bloemsma, E. A.; Vlaming, S. M.; van der Kwaak, C. G. F.; Silbey, R. J.; Bawendi, M. G.; Knoester, J.; Rabe, J. P.; Vanden Bout, D. A. Utilizing Redox-Chemistry to Elucidate the Nature of Exciton Transitions in Supramolecular Dye Nanotubes. *Nat Chem* **2012**, *4* (8), 655–662.

(210) Bailey, A. D.; Deshmukh, A. P.; Bradbury, N. C.; Pengshung, M.; Atallah, T. L.; Williams, J. A.; Barotov, U.; Neuhauser, D.; Sletten, E. M.; Caram, J. R. Exploring the

Design of Superradiant J-Aggregates from Amphiphilic Monomer Units. *Nanoscale* **2023**, *15* (8), 3841-3849.

(211) Longhi, G.; Castiglioni, E.; Koshoubu, J.; Mazzeo, G.; Abbate, S. Circularly Polarized Luminescence: A Review of Experimental and Theoretical Aspects. *Chirality* **2016**, *28* (10), 696–707.

(212) Lampoura, S. S.; Spitz, C.; Dähne, S.; Knoester, J.; Duppen, K. The Optical Dynamics of Excitons in Cylindrical J-Aggregates. *J. Phys. Chem. B* **2002**, *106* (12), 3103–3111.

(213) Kirstein, S.; Daehne, S. J-Aggregates of Amphiphilic Cyanine Dyes: Self-Organization of Artificial Light Harvesting Complexes. *International Journal of Photoenergy* **2007**, *2006*, e20363.

(214) Pugzlys, A.; Hania, P. R.; Augulis, R.; Duppen, K.; van Loosdrecht, P. H. M. Cylindrical Aggregates of 5,5',6,6'-Tetrachlorobenzimida-Carbocyanine Amphiphilic Derivatives: Structure-Related Optical Properties and Exciton Dynamics. *International Journal of Photoenergy* **2006**, *2006*, e29623.

(215) Kirstein, S.; Daehne, S. J-Aggregates of Amphiphilic Cyanine Dyes: Self-Organization of Artificial Light Harvesting Complexes. *International Journal of Photoenergy* **2007**, *2006*, e20363.

(216) Mishra, A.; Behera, R. K.; Behera, P. K.; Mishra, B. K.; Behera, G. B. Cyanines during the 1990s: A Review. *Chem. Rev.* **2000**, *100* (6), 1973–2012.

(217) Würthner, F.; Wortmann, R.; Meerholz, K. Chromophore Design for Photorefractive Organic Materials. *ChemPhysChem* **2002**, *3* (1), 17–31.

(218) Tani, T. J –AGGREGATES IN SPECTRAL SENSITIZATION OF PHOTOGRAPHIC MATERIALS. In *J-Aggregates*; WORLD SCIENTIFIC, **1996**; pp 209–228.

(219) Gadonas, R. Nonlinear Optical Properties of Pseudoisocyanine J -Aggregates. In *J-Aggregates*; WORLD SCIENTIFIC, **1996**; pp 181–197.

(220) McDermott, G.; Prince, S. M.; Freer, A. A.; Hawthornthwaite-Lawless, A. M.; Papiz, M. Z.; Cogdell, R. J.; Isaacs, N. W. Crystal Structure of an Integral Membrane Light-Harvesting Complex from Photosynthetic Bacteria. *Nature* **1995**, *374* (6522), 517–521.

(221) Pawlik, A.; Ouart, A.; Kirstein, S.; Abraham, H.-W.; Daehne, S. Synthesis and UV/Vis Spectra of J-Aggregating 5,5′,6,6′-Tetrachlorobenzimidacarbocyanine Dyes for Artificial Light-Harvesting Systems and for Asymmetrical Generation of Supramolecular Helices. *Eur. J. Org. Chem.* **2003**, *2003* (16), 3065–3080.

(222) von Berlepsch, H.; Böttcher, C.; Ouart, A.; Burger, C.; Dähne, S.; Kirstein, S. Supramolecular Structures of J-Aggregates of Carbocyanine Dyes in Solution. *J. Phys. Chem. B* **2000**, *104* (22), 5255–5262.

(223) Pugzlys, A.; Hania, P. R.; Augulis, R.; Duppen, K.; van Loosdrecht, P. H. M. Cylindrical Aggregates of 5,5',6,6'-Tetrachlorobenzimida-Carbocyanine Amphiphilic Derivatives: Structure-Related Optical Properties and Exciton Dynamics. *International Journal of Photoenergy* **2006**, *2006*, e29623.

(224) Pugzlys, A.; Hania, P. R.; Augulis, R.; Duppen, K.; van Loosdrecht, P. H. M. Cylindrical Aggregates of 5,5',6,6'-Tetrachlorobenzimida-Carbocyanine Amphiphilic Derivatives: Structure-Related Optical Properties and Exciton Dynamics. *International Journal of Photoenergy* **2006**, *2006*, e29623.

(225) von Berlepsch, H.; Kirstein, S.; Hania, R.; Didraga, C.; Pugžlys, A.; Böttcher, C. Stabilization of Individual Tubular J-Aggregates by Poly(Vinyl Alcohol). *J. Phys. Chem. B* **2003**, *107* (51), 14176–14184.

(226) Lampoura, S. S.; Spitz, C.; Dähne, S.; Knoester, J.; Duppen, K. The Optical Dynamics of Excitons in Cylindrical J-Aggregates. *J. Phys. Chem. B* **2002**, *106* (12), 3103–3111.

(227) Kirstein, S.; von Berlepsch, H.; Böttcher, C.; Burger, C.; Ouart, A.; Reck, G.; Dähne, S. Chiral J-Aggregates Formed by Achiral Cyanine Dyes. *ChemPhysChem* **2000**, *1* (3), 146–150.

(228) Kondepudi, D. K.; Kaufman, R. J.; Singh, N. Chiral Symmetry Breaking in Sodium Chlorate Crystallization. *Science* **1990**, *250* (4983), 975–976.

(229) Thomas, A.; Chervy, T.; Azzini, S.; Li, M.; George, J.; Genet, C.; Ebbesen, T. W. Mueller Polarimetry of Chiral Supramolecular Assembly. *J. Phys. Chem. C* **2018**, *122* (25), 14205–14212.

(230) Ortega-Quijano, N.; Arce-Diego, J. L. Mueller Matrix Differential Decomposition. *Opt. Lett., OL* **2011**, *36* (10), 1942–1944.

(231) Li, M. Mueller Polarimetry for Probing Supramolecular and Optical Chiralities. These de doctorat, Strasbourg, **2020**.

(232) Nizar, N. S. S.; Sujith, M.; Swathi, K.; Sissa, C.; Painelli, A.; Thomas, K. G. Emergent Chiroptical Properties in Supramolecular and Plasmonic Assemblies. *Chem. Soc. Rev.* **2021**, *50* (20), 11208–11226.

(233) Duong, S. T.; Fujiki, M. The Origin of Bisignate Circularly Polarized Luminescence (CPL) Spectra from Chiral Polymer Aggregates and Molecular Camphor: Anti-

Kasha's Rule Revealed by CPL Excitation (CPLE) Spectra. *Polym. Chem.* **2017**, *8* (32), 4673–4679.

(234) Viswanath, G.; Kasha, M. Confirmation of the Anomalous Fluorescence of Azulene. *J. Chem. Phys.* **1956**, *24* (3), 574–577.

(235) Tanaka, H.; Inoue, Y.; Mori, T. Circularly Polarized Luminescence and Circular Dichroisms in Small Organic Molecules: Correlation between Excitation and Emission Dissymmetry Factors. *ChemPhotoChem* **2018**, *2* (5), 386–402.

(236) Morisaki, Y.; Gon, M.; Sasamori, T.; Tokitoh, N.; Chujo, Y. Planar Chiral Tetrasubstituted [2.2]Paracyclophane: Optical Resolution and Functionalization. *J. Am. Chem. Soc.* **2014**, *136* (9), 3350–3353.

(237) Swathi, K.; Sissa, C.; Painelli, A.; Thomas, K. G. Supramolecular Chirality: A Caveat in Assigning the Handedness of Chiral Aggregates. *Chem. Commun.* **2020**, *56* (59), 8281–8284.

(238) Ghosh, N.; Vitkin, I. A. Tissue Polarimetry: Concepts, Challenges, Applications, and Outlook. *J Biomed Opt* **2011**, *16* (11), 110801.

(239) Hadley, K. C.; Vitkin, I. A. Optical Rotation and Linear and Circular Depolarization Rates in Diffusively Scattered Light from Chiral, Racemic, and Achiral Turbid Media. *J Biomed Opt* **2002**, *7* (3), 291–299.

(240) He, C.; He, H.; Chang, J.; Chen, B.; Ma, H.; Booth, M. J. Polarisation Optics for Biomedical and Clinical Applications: A Review. *Light Sci Appl* **2021**, *10* (1), 194.

(241) Lorchat, E.; Azzini, S.; Chervy, T.; Taniguchi, T.; Watanabe, K.; Ebbesen, T. W.; Genet, C.; Berciaud, S. Room-Temperature Valley Polarization and Coherence in Transition Metal Dichalcogenide–Graphene van Der Waals Heterostructures. *ACS Photonics* **2018**, *5* (12), 5047–5054.

(242) Qi, J.; Elson, D. S. A High Definition Mueller Polarimetric Endoscope for Tissue Characterisation. *Sci Rep* **2016**, *6* (1), 25953.

(243) Maji, K.; Saha, S.; Dey, R.; Ghosh, N.; Haldar, D. Mueller Matrix Fluorescence Spectroscopy for Probing Self-Assembled Peptide-Based Hybrid Supramolecular Structure and Orientation. *J. Phys. Chem. C* **2017**, *121* (35), 19519–19529.

(244) Saha, S.; Soni, J.; Chandel, S.; Ghosh, N.; Kumar, U. Probing Intrinsic Anisotropies of Fluorescence: Mueller Matrix Approach. *JBO* **2015**, *20* (8), 085005.

(245) Shinitzky, M.; Barenholz, Y. Dynamics of the Hydrocarbon Layer in Liposomes of Lecithin and Sphingomyelin Containing Dicetylphosphate. *J. Biol. Chem.* **1974**, *249* (8), 2652–2657.

(246) Mullaney, J. M.; Thompson, R. B.; Gryczynski, Z.; Black, L. W. Green Fluorescent Protein as a Probe of Rotational Mobility within Bacteriophage T4. *J. Virol. Methods* **2000**, *88* (1), 35–40.

(247) Marczak, A. Fluorescence Anisotropy of Membrane Fluidity Probes in Human Erythrocytes Incubated with Anthracyclines and Glutaraldehyde. *Bioelectrochemistry* **2009**, *74* (2), 236–239.

(248) Lúcio, M.; Ferreira, H.; Lima, J. L. F. C.; Matos, C.; Castro, B. de; Reis, S. Influence of Some Anti-Inflammatory Drugs in Membrane Fluidity Studied by Fluorescence Anisotropy Measurements. *Phys. Chem. Chem. Phys.* **2004**, *6* (7), 1493–1498.

(249) Li, Y.; Yu, H.; Zhao, Q. Aptamer Fluorescence Anisotropy Assays for Detection of Aflatoxin B1 and Adenosine Triphosphate Using Antibody to Amplify Signal Change. *RSC Advances* **2022**, *12* (12), 7464–7468.

(250) Zhang, D.; Lu, M.; Wang, H. Fluorescence Anisotropy Analysis for Mapping Aptamer–Protein Interaction at the Single Nucleotide Level. *J. Am. Chem. Soc.* **2011**, *133* (24), 9188–9191.

(251) Fluorescence Anisotropy. In *Principles of Fluorescence Spectroscopy*; Lakowicz, J. R., Ed.; Springer US: Boston, MA, 2006; pp 353–382.

(252) Arteaga, O.; Kahr, B. Mueller Matrix Polarimetry of Bianisotropic Materials [Invited]. *J. Opt. Soc. Am. B, JOSAB* **2019**, *36* (8), F72–F83.

(253) Tuchin, V. V.; Wang, L. V.; Zimnyakov, D. A. Biomedical Diagnostics and Imaging. In *Optical Polarization in Biomedical Applications*; Tuchin, V. V., Wang, L. V., Zimnyakov, D. A., Eds.; Biological and Medical Physics, Biomedical Engineering; Springer: Berlin, Heidelberg, **2006**; pp 177–223.

(254) Samanta, S.; Ray, S. K.; Deolka, S.; Saha, S.; R, P. K.; Bhowal, R.; Ghosh, N.; Chaudhuri, D. Safeguarding Long-Lived Excitons from Excimer Traps in H-Aggregated Dye-Assemblies. *Chem. Sci.* **2020**, *11* (22), 5710–5715.

(255) Maji, K.; Saha, S.; Dey, R.; Ghosh, N.; Haldar, D. Mueller Matrix Fluorescence Spectroscopy for Probing Self-Assembled Peptide-Based Hybrid Supramolecular Structure and Orientation. *J. Phys. Chem. C* **2017**, *121* (35), 19519–19529.

(256) Li, M. Mueller Polarimetry for Probing Supramolecular and Optical Chiralities. These de doctorat, Strasbourg, 2020.

(257) Arteaga, O.; Nichols, S.; Kahr, B. Mueller Matrices in Fluorescence Scattering. *Opt. Lett., OL* **2012**, *37* (14), 2835–2837.

(258) Kuśba, J.; Lakowicz, J. R. Definition and Properties of the Emission Anisotropy in the Absence of Cylindrical Symmetry of the Emission Field: Application to the Light Quenching Experiments. *J Chem Phys* **1999**, *111* (1), 89–99.

(259) Weber, G. Polarization of the Fluorescence of Macromolecules. 1. Theory and Experimental Method. *Biochemical Journal* **1952**, *51* (2), 145–155.

(260) Barotov, U.; Klein, M. D.; Wang, L.; Bawendi, M. G. Designing Highly Luminescent Molecular Aggregates via Bottom-Up Nanoscale Engineering. *J. Phys. Chem. C* **2022**, *126* (1), 754–763.

(261) Katrunov, I. K.; Sorokin, A. V.; Yefimova, S. L.; Malyukin, Yu. V. Manifestation of Exciton-Lattice Interaction in J-Aggregates. *Molecular Crystals and Liquid Crystals* **2011**, *535* (1), 57–63.

(262) Sorokin, A. V.; Filimonova, I. I.; Grynyov, R. S.; Guralchuk, G. Ya.; Yefimova, S. L.; Malyukin, Y. V. Control of Exciton Migration Efficiency in Disordered J-Aggregates. *J. Phys. Chem. C* **2010**, *114* (2), 1299–1305.

(263) Klein, M. D.; Shulenberger, K. E.; Barotov, U.; Šverko, T.; Bawendi, M. G. Supramolecular Lattice Deformation and Exciton Trapping in Nanotubular J-Aggregates. *J. Phys. Chem. C* **2022**, *126* (8), 4095–4105.

(264) Thomas, A.; Chervy, T.; Azzini, S.; Li, M.; George, J.; Genet, C.; Ebbesen, T. W. Mueller Polarimetry of Chiral Supramolecular Assembly. *J. Phys. Chem. C* **2018**, *122* (25), 14205–14212.

(265) Adelizzi, B.; Van Zee, N. J.; de Windt, L. N. J.; Palmans, A. R. A.; Meijer, E. W. Future of Supramolecular Copolymers Unveiled by Reflecting on Covalent Copolymerization. *J. Am. Chem. Soc.* **2019**, *141* (15), 6110–6121.

(266) Brunsveld, L.; Folmer, B. J. B.; Meijer, E. W.; Sijbesma, R. P. Supramolecular Polymers. *Chem. Rev.* **2001**, *101* (12), 4071–4098.

(267) Zhao, D.; Moore, J. S. Nucleation–Elongation: A Mechanism for Cooperative Supramolecular Polymerization. *Org. Biomol. Chem.* **2003**, *1* (20), 3471–3491.

(268) Aida, T.; Meijer, E. W.; Stupp, S. I. Functional Supramolecular Polymers. *Science* **2012**, *335* (6070), 813–817.

(269) Lehn, J.-M. Toward Complex Matter: Supramolecular Chemistry and Self-Organization. *Proceedings of the National Academy of Sciences* **2002**, *99* (8), 4763–4768.

(270) Sijbesma, R. P.; Beijer, F. H.; Brunsveld, L.; Folmer, B. J.; Hirschberg, J. H.; Lange, R. F.; Lowe, J. K.; Meijer, E. W. Reversible Polymers Formed from Self-

Complementary Monomers Using Quadruple Hydrogen Bonding. *Science* **1997**, *278* (5343), 1601–1604.

(271) Palmans, A. R. A.; Meijer, E. W. Amplification of Chirality in Dynamic Supramolecular Aggregates. *Angew. Chem., Int. Ed.* **2007**, *46* (47), 8948–8968.

(272) van der Zwaag, D.; de Greef, T. F. A.; Meijer, E. W. Programmable Supramolecular Polymerizations. *Angew. Chem., Int. Ed.* **2015**, *54* (29), 8334–8336.

(273) Korevaar, P. A.; George, S. J.; Markvoort, A. J.; Smulders, M. M. J.; Hilbers, P. A. J.; Schenning, A. P. H. J.; De Greef, T. F. A.; Meijer, E. W. Pathway Complexity in Supramolecular Polymerization. *Nature* **2012**, *481* (7382), 492–496.

(274) Korevaar, P. A.; de Greef, T. F. A.; Meijer, E. W. Pathway Complexity in π-Conjugated Materials. *Chem. Mater.* **2014**, *26* (1), 576–586.

(275) Gsänger, M.; Bialas, D.; Huang, L.; Stolte, M.; Würthner, F. Organic Semiconductors Based on Dyes and Color Pigments. *Adv. Mater* **2016**, *28* (19), 3615–3645.

(276) Bouman, M. M.; Meijer, E. W. Stereomutation in Optically Active Regioregular Polythiophenes. *Adv. Mater* **1995**, *7* (4), 385–387.

(277) Aida, T.; Meijer, E. w. Supramolecular Polymers – We've Come Full Circle. *Isr. J. Chem.* **2020**, *60* (1–2), 33–47.

(278) Würthner, F. Living It Up. *Nature Chem* **2014**, *6* (3), 171–173.

(279) Chen, Z.; Lohr, A.; Saha-Möller, C. R.; Würthner, F. Self-Assembled π-Stacks of Functional Dyes in Solution: Structural and Thermodynamic Features. *Chem. Soc. Rev.* **2009**, *38* (2), 564–584.

(280) Markvoort, A. J.; ten Eikelder, H. M. M.; Hilbers, P. A. J.; de Greef, T. F. A.; Meijer, E. W. Theoretical Models of Nonlinear Effects in Two-Component Cooperative Supramolecular Copolymerizations. *Nat Commun* **2011**, *2* (1), 509.

(281) De Greef, T. F. A.; Smulders, M. M. J.; Wolffs, M.; Schenning, A. P. H. J.; Sijbesma, R. P.; Meijer, E. W. Supramolecular Polymerization. *Chem. Rev.* **2009**, *109* (11), 5687–5754.

(282) Martin, R. B. Comparisons of Indefinite Self-Association Models. *Chem. Rev.* **1996**, *96* (8), 3043–3064.

(283) Mattia, E.; Otto, S. Supramolecular Systems Chemistry. *Nature Nanotech* **2015**, *10* (2), 111–119.

(284) Mukhopadhyay, R. D.; Ajayaghosh, A. Living Supramolecular Polymerization. *Science* **2015**, *349* (6245), 241–242.

(285) Matern, J.; Dorca, Y.; Sánchez, L.; Fernández, G. Revising Complex Supramolecular Polymerization under Kinetic and Thermodynamic Control. *Angew. Chem., Int. Ed.* **2019**, *58* (47), 16730–16740.

(286) Sorrenti, A.; Leira-Iglesias, J.; Markvoort, A. J.; Greef, T. F. A. de; Hermans, T. M. Non-Equilibrium Supramolecular Polymerization. *Chem. Soc. Rev.* **2017**, *46* (18), 5476–5490.

(287) van der Zwaag, D.; Pieters, P. A.; Korevaar, P. A.; Markvoort, A. J.; Spiering, A. J. H.; de Greef, T. F. A.; Meijer, E. W. Kinetic Analysis as a Tool to Distinguish Pathway Complexity in Molecular Assembly: An Unexpected Outcome of Structures in Competition. *J. Am. Chem. Soc.* **2015**, *137* (39), 12677–12688.

(288) Lohr, A.; Würthner, F. Evolution of Homochiral Helical Dye Assemblies: Involvement of Autocatalysis in the "Majority-Rules" Effect. *Angew. Chem., Int. Ed.* **2008**, *47* (7), 1232–1236.

(289) Hifsudheen, M.; Mishra, R. K.; Vedhanarayanan, B.; Praveen, V. K.; Ajayaghosh, A. The Helix to Super-Helix Transition in the Self-Assembly of π-Systems: Superseding of Molecular Chirality at Hierarchical Level. *Angew. Chem., Int. Ed.* **2017**, *56* (41), 12634–12638.

(290) Würthner, F.; Yao, S.; Beginn, U. Highly Ordered Merocyanine Dye Assemblies by Supramolecular Polymerization and Hierarchical Self-Organization. *Angew. Chem., Int. Ed.* **2003**, *42* (28), 3247–3250.

(291) Lohr, A.; Lysetska, M.; Würthner, F. Supramolecular Stereomutation in Kinetic and Thermodynamic Self-Assembly of Helical Merocyanine Dye Nanorods. *Angew. Chem., Int. Ed.* **2005**, *44* (32), 5071–5074.

(292) Yagai, S.; Yamauchi, M.; Kobayashi, A.; Karatsu, T.; Kitamura, A.; Ohba, T.; Kikkawa, Y. Control over Hierarchy Levels in the Self-Assembly of Stackable Nanotoroids. *J. Am. Chem. Soc.* **2012**, *134* (44), 18205–18208.

(293) Smulders, M. M. J.; Nieuwenhuizen, M. M. L.; de Greef, T. F. A.; van der Schoot, P.; Schenning, A. P. H. J.; Meijer, E. W. How to Distinguish Isodesmic from Cooperative Supramolecular Polymerisation. *Chem. Eur. J.* **2010**, *16* (1), 362–367.

(294) Wehner, M.; Würthner, F. Supramolecular Polymerization through Kinetic Pathway Control and Living Chain Growth. *Nat Rev Chem* **2020**, *4* (1), 38–53.

(295) Korevaar, P. A.; Schaefer, C.; de Greef, T. F. A.; Meijer, E. W. Controlling Chemical Self-Assembly by Solvent-Dependent Dynamics. *J. Am. Chem. Soc.* **2012**, *134* (32), 13482–13491.

(296) Fernández, G.; Stolte, M.; Stepanenko, V.; Würthner, F. Cooperative Supramolecular Polymerization: Comparison of Different Models Applied on the Self-Assembly of Bis(Merocyanine) Dyes. *Chem. Eur. J.* **2013**, *19* (1), 206–217.

(297) Jonkheijm, P.; van der Schoot, P.; Schenning, A. P. H. J.; Meijer, E. W. Probing the Solvent-Assisted Nucleation Pathway in Chemical Self-Assembly. *Science* **2006**, *313* (5783), 80–83.

(298) Goldstein, R. F.; Stryer, L. Cooperative Polymerization Reactions. Analytical Approximations, Numerical Examples, and Experimental Strategy. *Biophysical Journal* **1986**, *50* (4), 583–599.

(299) Gershberg, J.; Fennel, F.; Rehm, T. H.; Lochbrunner, S.; Würthner, F. Anti-Cooperative Supramolecular Polymerization: A New K2–K Model Applied to the Self-Assembly of Perylene Bisimide Dye Proceeding via Well-Defined Hydrogen-Bonded Dimers. *Chem. Sci.* **2016**, *7* (3), 1729–1737.

(300) Thomas, A.; Chervy, T.; Azzini, S.; Li, M.; George, J.; Genet, C.; Ebbesen, T. W. Mueller Polarimetry of Chiral Supramolecular Assembly. *J. Phys. Chem. C* **2018**, *122* (25), 14205–14212.

(301) Hananel, U.; Schwartz, G.; Paiss, G.; Arrico, L.; Zinna, F.; Di Bari, L.; Cheshnovsky, O.; Markovich, G. Time-Resolved Circularly Polarized Luminescence of Eu3+-Based Systems. *Chirality* **2021**, *33* (3), 124–133.

(302) Kondo, Y.; Suzuki, S.; Watanabe, M.; Kaneta, A.; Albertini, P.; Nagamori, K. Temperature-Dependent Circularly Polarized Luminescence Measurement Using KBr Pellet Method. *Frontiers in Chemistry* **2020**, *8,* 527.

(303) Lorchat, E.; Azzini, S.; Chervy, T.; Taniguchi, T.; Watanabe, K.; Ebbesen, T. W.; Genet, C.; Berciaud, S. Room-Temperature Valley Polarization and Coherence in Transition Metal Dichalcogenide–Graphene van Der Waals Heterostructures. *ACS Photonics* **2018**, *5* (12), 5047–5054.

(304) Voloshin, A. I.; Shavaleev, N. M.; Kazakov, V. P. Water Enhances Quantum Yield and Lifetime of Luminescence of Europium(III) Tris-β-Diketonates in Concentrated Toluene and Acetonitrile Solutions. *J. Lumin.* **2001**, *93* (3), 191–197.

(305) Brittain, H. G.; Richardson, F. S. Circularly Polarized Emission Studies on the Chiral Nuclear Magnetic Resonance Lanthanide Shift Reagent Tris(3-Trifluoroacetyl-d-Camphorato)Europium(III). *J. Am. Chem. Soc.* **1976**, *98* (19), 5858–5863.

(306) MacKenzie, L. E.; Pal, R. Circularly Polarized Lanthanide Luminescence for Advanced Security Inks. *Nat Rev Chem* **2021**, *5* (2), 109–124.

(307) Genet, C.; Faist, J.; Ebbesen, T. W. Inducing New Material Properties with Hybrid Light–Matter States. *Physics Today* **2021**, *74* (5), 42–48.

(308) Sandeep, K.; Joseph, K.; Gautier, J.; Nagarajan, K.; Sujith, M.; Thomas, K. G.; Ebbesen, T. W. Manipulating the Self-Assembly of Phenyleneethynylenes under Vibrational Strong Coupling. *J. Phys. Chem. Lett.* **2022**, *13* (5), 1209–1214.

(309) Spano, F. C. Optical Microcavities Enhance the Exciton Coherence Length and Eliminate Vibronic Coupling in J-Aggregates. *J. Chem. Phys.* **2015**, *142* (18), 184707.

(310) Li, M.; Nizar, S.; Saha, S.; Thomas, A.; Azzini, S.; Ebbesen, T. W.; Genet, C. Strong Coupling of Chiral Frenkel Exciton for Intense, Bisignate Circularly Polarized Luminescence. *Angew. Chem., Int. Ed.* **2023**, *62* (6), e202212724.

Université de Strasbourg

École doctorale
Sciences chimiques | ED 222
Université de Strasbourg

UNIVERSITE DE STRASBOURG

ECOLE DOCTORALE DES SCIENCES CHIMIQUES

RESUME DE LA THESE DE DOCTORAT

1) Introduction

Le domaine des assemblages supramoléculaires est connu pour passer d'une simple science de la complexation hôte-invité à un domaine actuellement exploré dans toutes les régions du monde, exigeant un intérêt extrême pour la compréhension des systèmes vivants, qui est une forme complexe d'espèces supramoléculaires sophistiquées de protéines, ADN, structures cellulaires, etc.[1,2] Non seulement pour comprendre les mécanismes de fonctionnement des architectures supramoléculaires complexes sous une forme vivante en les imitant à l'aide de matériaux bio-inspirés, mais le domaine a émergé dans le développement de matériaux fonctionnels pour tenir compte des problèmes mondiaux de pollution, d'applications technologiques et de diagnostics médicaux.[2] L'intérêt de la recherche pour ces structures fascinantes consiste principalement à synthétiser des structures moléculaires et supramoléculaires qui sont manipulées pour une fonctionnalité spécifique. Ce développement d'une stratégie de synthèse nécessite des méthodes de caractérisation expérimentale appropriées et une compréhension théorique de l'interaction lumière-matière.

Une réponse optique intéressante observée à partir d'agrégats supramoléculaires est l'amplification de la signature chirale. L'augmentation de la réponse chirale est depuis longtemps un intérêt de recherche exigeant des chimistes synthétiques pour moduler la structure moléculaire pour les propriétés souhaitées. Cependant, la chiralité au niveau moléculaire est limitée à l'ordre de 10^{-5} à 10^{-2}, là où réside l'intérêt de la chiralité supramoléculaire.[3] Ces systèmes montrent une réponse chiroptique amplifiée grâce à un couplage fort des excitons.[3] Cependant, l'étude de ces propriétés dans des structures supramoléculaires est extrêmement difficile avec les méthodes conventionnelles impliquant le dichroïsme circulaire électronique. Cette difficulté survient principalement en raison de l'anisotropie élevée, de l'inhomogénéité et de la réabsorption de la lumière dues au faible décalage de Stokes dans l'émission, ce qui entraîne des artefacts indésirables dus à l'effet de filtrage interne. De plus, la caractérisation de l'anisotropie de fluorescence est extrêmement importante pour les chimistes pour étudier les interactions protéiques, la fluidité membranaire, etc. [4] Cependant, la diffusion des fluorophores, la dépolarisation et la réabsorption de la lumière émise affectent la mesure de l'anisotropie intrinsèque. Par conséquent, les

mesures d'anisotropie sont limitées à la plupart des petites molécules, mais l'élargissement du domaine aux systèmes supramoléculaires est très exigeant. De plus, l'étude de la complexité des voies des agrégats supramoléculaires est un domaine de recherche important en chimie pour identifier, manipuler et contrôler les différentes étapes de l'application fonctionnelle des agrégats. Cela exige également des méthodes de caractérisation spectroscopique appropriées qui fournissent des propriétés polarimétriques intrinsèques du matériau. À cet égard, la polarimétrie de Mueller est une technique récemment apparue qui a montré une excellente capacité à éliminer les artefacts dans les mesures polarimétriques.[5]

Dans cette thèse, nous nous concentrons principalement sur l'extraction des signaux polarimétriques sans artéfact du C8O3 (3,3′-bis(3-carboxy-n-propyl)-3,3′-di-n-octyl-5,5′, 6,6′-tétrachlorobenzimidacarbocyanine) en utilisant la méthode polarimétrique de Mueller. Les agrégats de C8O3 ont montré des propriétés polarimétriques intéressantes à l'état fondamental alors que leur état excité n'a pas été bien exploré. En utilisant la méthode polarimétrique de Mueller, nous montrons diverses propriétés intéressantes qui ne sont pas observables dans les méthodes conventionnelles. Cette méthode est actuellement une technique émergente qui a montré le potentiel de changer les limites de la spectroscopie chiroptique. Dans cette thèse, nous exploitons toutes les informations polarimétriques que le formalisme de Mueller pourrait fournir, et présentons l'efficacité du système à fournir des informations essentielles pour les chimistes.

2) Résultats et discussions

Cette thèse est divisée en 6 chapitres comme brièvement discuté ci-dessous.

Chapitre 1: Dans ce chapitre, nous introduisons les concepts de base et les intérêts de recherche actuels sur la chiralité moléculaire et supramoléculaire. Nous discutons brièvement de l'évolution du domaine de la chiralité qui a ouvert la voie à l'identification de différentes façon d’observer des signaux chiraux tels que la chiralité ponctuelle, la chiralité axiale et la chiralité supramoléculaire. Nous discutons également de la compréhension théorique de l'émergence de la chiralité dans les molécules et les assemblages supramoléculaires. En outre, nous présentons diverses techniques analytiques récemment avancées pour caractériser les structures chirales visant à améliorer la sensibilité des signaux et la détection de signaux sans artefact.

Chapitre 2: Dans ce chapitre, nous présentons la méthode polarimétrique de Mueller, ses techniques de calibration et le protocole expérimental pour réaliser les études sur les systèmes supramoléculaires. Nous présentons également diverses observables qui peuvent être extraites de la mesure pour comprendre les propriétés structurelles et optiques du matériau.

Chapitre 3: Dans ce chapitre, nous explorons les propriétés chiroptiques de l'état fondamental et excité des agrégats de C8O3 groupés à l'aide de la polarimétrie de Mueller pour montrer que le couplage fort des excitons chiraux de Frenkel de ces agrégats J en couche mince produit des facteurs de dissymétrie bissignés intenses en absorption et émission de l'ordre 0,08. Nous utilisons des mesures prudentes pour éliminer les artefacts dus à la réabsorption, à l'anisotropie élevée et à l'inhomogénéité de l'échantillon afin de mesurer les propriétés intrinsèques de l'agrégat regroupé. Avec cette mesure de Mueller sans artefact, nous étudions la corrélation entre la chiralité de l'état fondamental et de l'état excité qui explique une nature émissive anti-Kasha difficilement perceptible avec les études polarimétriques conventionnelles. Les résultats de ce chapitre ont été récemment publiés. (Figure 1)

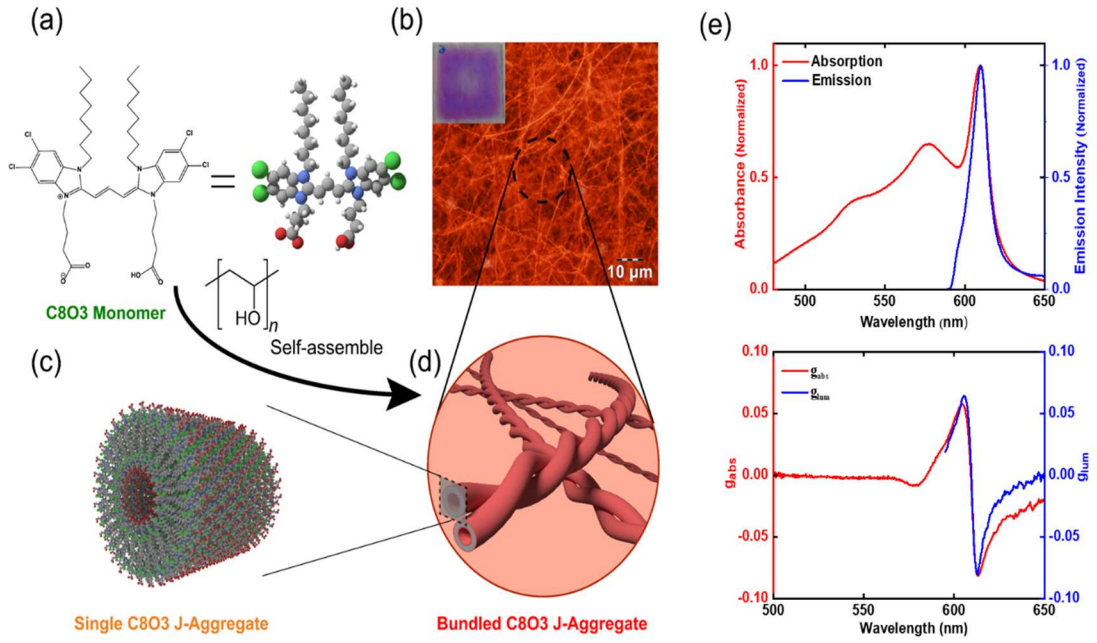

Figure 13 : *structure chimique du monomère C8O3 (a), qui s'auto-assemble en agrégats tubulaires (c), qui forment ensuite des faisceaux (d) comme on le voit sur l'image microscopique à fond noir (b). (e) Les spectres d'absorption et d'émission (panneau supérieur) et le facteur de dissymétrie CD et CPL (panneau inférieur) des agrégats regroupés.*

Chapitre 4: Dans ce chapitre, nous explorons les propriétés anisotropes de l'état excité dépendant de la longueur d'onde d'excitation des agrégats de C8O3 à l'état de film en utilisant la polarimétrie Mueller bidimensionnelle d'excitation-émission (2D-EE). La caractérisation de l'anisotropie de ces structures est très difficile en raison de la forte inhomogénéité de l'échantillon et du décalage de zéro-Stokes dans l'émission. En utilisant le formalisme de Mueller, nous séparons l'anisotropie intrinsèque et extrinsèque et analysons ainsi l'évolution dépendante de la longueur d'onde des propriétés polarimétriques de l'état fondamental et excité de l'agrégat groupé, telles que le dichroïsme linéaire détecté par fluorescence, le dichroïsme circulaire détecté par fluorescence, la luminescence polarisée linéairement, la luminescence polarisée

circulairement et l'anisotropie des dipôles d'excitation et d'émission. Nous montrons également que ces mesures d'anisotropie sans artefact aident à déterminer l'orientation des dipôles d'excitation et d'émission et leur ordre d'orientation. Un manuscrit est en cours de préparation avec les résultats de ce chapitre. (Figure 2)

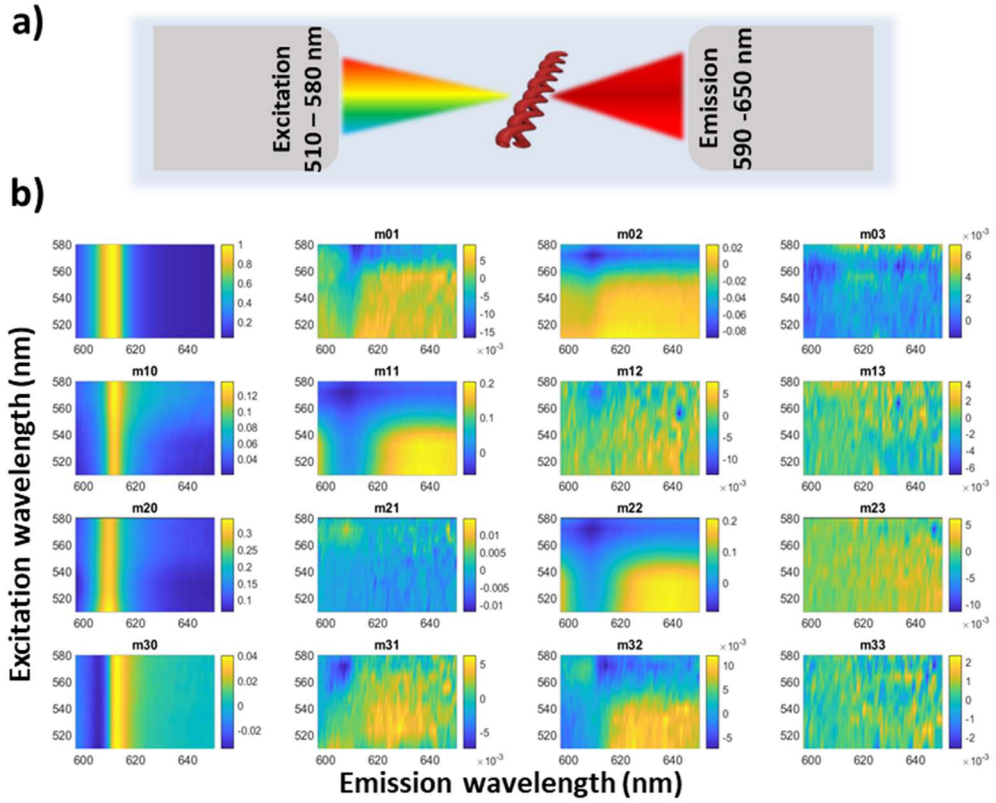

Figure 14 : *a) Les gammes de longueurs d'onde d'excitation et d'émission sont démontrées. b) La matrice de Mueller 2D-EE de l'agrégat.*

Chapitre 5: Dans ce chapitre, en utilisant la méthode polarimétrique de Mueller, nous suivons la voie de désassemblage du film d'agrégats groupés de C8O3 à travers des cycles de chauffage-refroidissement. L'utilisation du formalisme de Mueller est essentielle pour explorer la complexité des voies de ces agrégats en raison de la forte anisotropie et de l'inhomogénéité du système qui empêche une analyse spectrale fiable. Ici, nous montrons qu'en plus de la caractérisation conventionnelle UV-Vis et chiroptique, suivre la progression spectrale dans le dichroïsme linéaire et le degré de polarisation peut également fournir des informations essentielles concernant la voie de polymérisation. Nous explorons différents protocoles expérimentaux et divers défis liés à l'utilisation de la méthode et présentons diverses observables souhaitées, sensibles aux variations structurelles. Dans ce chapitre, nous élargissons les limites de la méthode polarimétrique de Mueller pour explorer la complexité de la voie d'agrégation. (Figure 3)

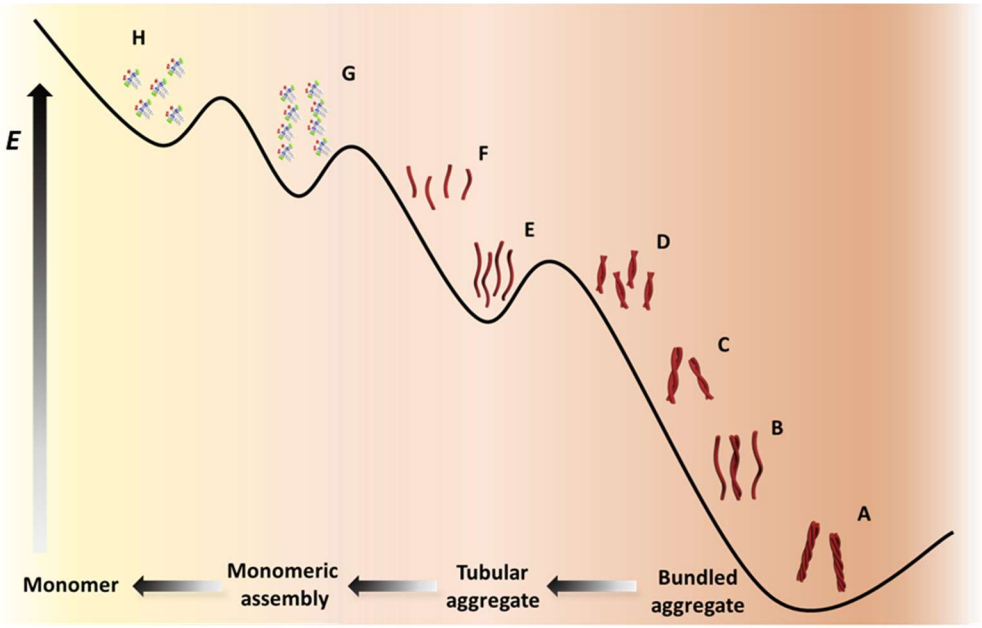

Figure 15: *Illustration graphique montrant le paysage énergétique de la voie d'agrégation du C8O3 tirée des enseignements de l'analyse polarimétrique de Mueller.*

Chapitre 6 : Dans ce chapitre, nous fournissons une brève conclusion sur la méthodologie et les résultats expérimentaux obtenus à l'aide du formalisme de Mueller. Nous fournissons également diverses perspectives futures sur les études. Cela inclut des méthodes pour biaiser la chiralité des agrégats de C8O3. Nous expliquons également la possibilité d'améliorer les signatures chirales grâce à un couplage fort lumière-matière. En outre, nous présentons également les recherches actuellement en cours sur les études théoriques collaboratives sur les agrégats chiraux C8O3.

3) Conclusion générale

Pour conclure, dans cette thèse, nous présentons l'efficacité du formalisme de Mueller pour fournir une analyse polarimétrique sans artefact sur des assemblages supramoléculaires. A travers ce travail, nous identifions diverses propriétés intéressantes des agrégats de C8O3 qui sont difficilement observables dans les méthodes conventionnelles. Bien que les agrégats de C8O3 aient été bien étudiés dans la littérature, les propriétés de l'état excité de ce système n'ont pas été bien explorées. En utilisant le formalisme de Mueller, nous étudions ces propriétés pour les identifier comme des émetteurs potentiels de CPL. Nous présentons également diverses propriétés uniques et intéressantes de ces matériaux telles que l'émission Anti-Kasha et la forte corrélation entre l'état fondamental et l'état excité. De plus, à travers la matrice de Mueller 2D-excitation-émission, nous présentons l'anisotropie de fluorescence dépendante de la longueur d'onde du matériau. Ces propriétés ne sont pas facilement observables en raison des problèmes de réabsorption. Enfin, nous suivons la complexité de la voie des agrégats à l'aide de la polarimétrie de Mueller,

au fur et à mesure que le système se désassemble de sa phase agrégée à la phase monomère. Ces études montrent l'importance d'utiliser la polarimétrie de Mueller comme outil analytique pour la caractérisation supramoléculaire sans artéfact.

4) Références

[1] Lehn, J.-M. Supramolecular Chemistry—Scope and Perspectives Molecules, Supermolecules, and Molecular Devices (Nobel Lecture). Angewandte Chemie International Edition in English 1988, 27 (1), 89–112.
[2] Uhlenheuer, D. A.; Petkau, K.; Brunsveld, L. Combining Supramolecular Chemistry with Biology. Chem. Soc. Rev. 2010, 39 (8), 2817–2826.
[3] Kolesnichenko, I. V.; Anslyn, E. V. Practical Applications of Supramolecular Chemistry. Chem. Soc. Rev. 2017, 46 (9), 2385–2390.
[4] Nizar, N. S. S.; Sujith, M.; Swathi, K.; Sissa, C.; Painelli, A.; Thomas, K. G. Emergent Chiroptical Properties in Supramolecular and Plasmonic Assemblies. Chem. Soc. Rev. 2021, 50 (20), 11208–11226.
[5] Marczak, A. Fluorescence Anisotropy of Membrane Fluidity Probes in Human Erythrocytes Incubated with Anthracyclines and Glutaraldehyde. Bioelectrochemistry 2009, 74 (2), 236–239.
[6] Thomas, A.; Chervy, T.; Azzini, S.; Li, M.; George, J.; Genet, C.; Ebbesen, T. W. Mueller Polarimetry of Chiral Supramolecular Assembly. J. Phys. Chem. C 2018, 122 (25), 14205–14212.

Université de Strasbourg

École doctorale Sciences chimiques | ED 222 Université de Strasbourg

Shahana Nizar NIZAR SHYLA

Characterization of chiral supramolecular assemblies using Mueller polarimetry

Résumé

Cette thèse discute des défis que pose la caractérisation des assemblages supramoléculaires chiraux dus à l'inhomogénéité de l'échantillon, à l'effet de filtrage interne et aux effets d'anisotropie, qui tous induisent des artefacts dans les mesures polarimétriques. Ces défis sont relevés par l'utilisation de la polarimétrie de Mueller qui permet d'extraire les propriétés polarimétriques intrinsèques des structures supramoléculaires chirales, à la fois dans les états fondamentaux et excités. Grâce à cette polarimétrie, cette thèse peut étudier sur des agrégats supramoléculaires chiraux les réponses chiroptiques intrinsèques, la polarisation de fluorescence et la diversité hiérarchique des voies d'agrégations sur de tels systèmes moléculaires complexes. Les résultats présentés dans ce travail seraient autrement difficiles à obtenir en utilisant des méthodes de caractérisation conventionnelles.

Mots clés : Anisotropie — assemblages supramoléculaires — Chiralité — complexité des voies — Polarimétrie de Mueller — polarisation de fluorescence

Résumé en anglais

This thesis discusses the challenges in characterizing chiral supramolecular assemblies arising due to sample inhomogeneity, inner-filtering effect, and high anisotropy, inducing artefacts in polarimetric measurements. These challenges are addressed using Mueller polarimetry to extract the intrinsic polarimetric properties of chiral supramolecular structures in both ground and excited states. Employing this method, this thesis is able to study on chiral supramolecular aggregates' intrinsic chiroptical responses, fluorescence polarizations, and the hierarchical pathway diversity for aggregation offered by such complex molecular systems. The results presented in this work would have been otherwise hardly accessible using conventional characterization methods.

Keywords: Anisotropy — Chirality — fluorescence polarization — Mueller polarimetry — pathway complexity — supramolecular assemblies